

Nucleon Isovector Axial Form Factors

Yong-Chull Jang,^{1,2,3,*} Rajan Gupta,^{4,†} Tanmoy Bhattacharya,^{4,‡} Boram Yoon,^{5,§} and Huey-Wen Lin^{6,¶}
(Precision Neutron Decay Matrix Elements (PNDME) Collaboration)

¹*Electron-Ion Collider, Brookhaven National Laboratory, Upton, New York 11973*

²*Physics Department, Brookhaven National Laboratory, Upton, New York 11973*

³*Department of Physics, Columbia University, 538 West 120th Street, New York, NY 10027, USA*

⁴*Los Alamos National Laboratory, Theoretical Division T-2, Los Alamos, NM 87545, USA*

⁵*NVIDIA Corporation, Santa Clara, CA 95051, USA*

⁶*Department of Physics and Astronomy, Michigan State University, MI, 48824, USA*

(Dated: June 12, 2023)

We present results for the isovector axial vector form factors obtained using thirteen 2+1+1-flavor highly improved staggered quark (HISQ) ensembles generated by the MILC collaboration. The calculation of nucleon two- and three-point correlation functions has been done using Wilson-clover fermions. In the analysis of these data, we quantify the sensitivity of the results to strategies used for removing excited state contamination and invoke the partially conserved axial current relation between the form factors to choose between them. Our data driven analysis includes removing contributions from multihadron $N\pi$ states that make significant contributions. Our final results are: $g_A = 1.292(53)_{\text{stat}}(24)_{\text{sys}}$ for the axial charge; $g_S = 1.085(50)_{\text{stat}}(103)_{\text{sys}}$ and $g_T = 0.991(21)_{\text{stat}}(10)_{\text{sys}}$ for the scalar and tensor charges; $\langle r_A^2 \rangle = 0.439(56)_{\text{stat}}(34)_{\text{sys}} \text{ fm}^2$ for the mean squared axial charge radius, $g_P^* = 9.03(47)_{\text{stat}}(42)_{\text{sys}}$ for the induced pseudoscalar charge; and $g_{\pi NN} = 14.14(81)_{\text{stat}}(85)_{\text{sys}}$ for the pion-nucleon coupling. We also provide a parameterization of the axial form factor $G_A(Q^2)$ over the range $0 \leq Q^2 \leq 1 \text{ GeV}^2$ for use in phenomenology and a comparison with other lattice determinations. We find that the various lattice data agree within 10% but are significantly different from the extraction of $G_A(Q^2)$ from the ν -deuterium scattering data.

I. INTRODUCTION

In current neutrino scattering experiments (T2K, NOvA, MINERvA, MicroBooNE, SBN), the lack of precise reconstruction of the final state of the struck nucleus gives rise to uncertainty in the cross-section. Theoretical calculations of the cross-section for targets such as ^{12}C , ^{16}O , and ^{40}Ar , being used in experiments take as input axial vector form factor of the nucleon and build in nuclear effects using nuclear many body theory [1–3]. The cleanest experimental measurements of the nucleon axial form factor from scattering neutrinos off liquid hydrogen targets are not being carried out due to safety concerns. Similarly, the two steps in the theoretical analysis, calculating nucleon axial form factors using lattice QCD and including nuclear effects using many-body theory, have uncertainties. Incorporating nuclear effects involves modeling of the complex physical phenomena (quasi-elastic, resonance, deep inelastic scattering) that contribute when considering incoming neutrino energies up to 5 GeV relevant for ongoing and future (DUNE) experiments. These complex phenomena make it hard to reconstruct the incident neutrino energy or the cross-section from the imprecise knowledge of the final state of the struck nucleus.

The MINERvA experiment [4] has recently shown that the axial form factor of the nucleon can be extracted from the charged current elastic scattering process $\bar{\nu}_\mu H \rightarrow \mu^+ n$ in which the free proton in hydrogen (H) gets converted into a neutron. This opens the door to direct measurements of the nucleon axial form factor (without the historic need for nuclear corrections when extracting then from nuclei), and direct comparisons with predictions using lattice QCD. Our final result for the axial charge radius, $\langle r_A^2 \rangle = 0.439(56)_{\text{stat}}(34)_{\text{sys}} \text{ fm}^2$, given in Eq. (36), is consistent, within one combined sigma, with their result, $\sqrt{\langle r_A^2 \rangle} = 0.73 \pm 0.17 \text{ fm}$.

Similarly, recent advances in simulations of lattice QCD have enabled robust results for the nucleon charges that have been reviewed by the Flavor Lattice Averaging Group (FLAG) in their 2019 and 2021 reports [5, 6]). Results for axial vector form factors [7] are now available with $\lesssim 10\%$ uncertainty as we show in this work. At the same time, there continues to be progress in nuclear many-body theory in the calculation of the neutrino-nucleus cross-section [1].

In this work, we present lattice QCD results for the isovector axial, $G_A(Q^2)$, induced pseudoscalar, $\tilde{G}_P(Q^2)$, and pseudoscalar $G_P(Q^2)$ form factors, the axial, scalar and tensor isovector charges g_A^{u-d} , g_S^{u-d} and g_T^{u-d} , the axial charge radius squared $\langle r_A^2 \rangle$, the induced pseudoscalar coupling g_P^* , and the pion-nucleon coupling $g_{\pi NN}$.

The calculation has been done using thirteen ensembles generated with 2+1+1-flavors of highly improved staggered quarks (HISQ) by the MILC collaboration [8]. The construction of nucleon two- and three-point correlation

* integration.field@gmail.com

† rajan@lanl.gov

‡ tanmoy@lanl.gov

§ byoon@nvidia.com

¶ hwlin@pa.msu.edu

functions has been done using Wilson-clover fermions. The analysis of the data generated using this clover-on-HISQ formulation includes a study of excited state contributions (ESC) in the extraction of ground state matrix elements (GSME) and a simultaneous chiral-continuum-finite-volume (CCFV) fit to obtain results at the physical point, which throughout the paper will be defined as taking the continuum ($a = 0$) and infinite volume ($M_\pi L \rightarrow \infty$) limits at physical light quark masses in the isospin symmetric limit, $m_u = m_d$, which is set using the neutral pion mass ($M_{\pi^0} = 135$ MeV). The masses of the strange and charm quarks in the lattice generation have been tuned to be close to their physical values in each of the thirteen ensembles [8].

The three form factors $G_A(Q^2)$, $\tilde{G}_P(Q^2)$ and $G_P(Q^2)$ must, up to discretization errors, satisfy the constraint in Eq. (16) imposed by the partially conserved axial current (PCAC) relation $\partial_\mu A_\mu = 2mP$ between the axial and pseudoscalar currents. The decomposition of the matrix elements, given in Eqs. 1 and (2), assumes that they are GSME. Post-facto, deviations from the PCAC relation larger than those expected due to lattice discretization artifacts are indicative of residual ESC in the extraction of matrix elements from the spectral decomposition of the three-point correlation functions. They point to the need for reevaluation of the key inputs in this analysis—the number and energies of the excited states that contribute significantly to the three-point functions. The strategies used to remove ESC are described in sections II B and V, and the use of the PCAC relation to evaluate how well ESC have been controlled is discussed in Sec. II C.

In Ref. [9], we showed that the standard method of taking the excited-state spectrum from fits to the nucleon two-point correlation function to analyze the three-point functions lead to form factors that fail the PCAC test by almost a factor of two on the physical pion mass ensemble $a09m130W$, and identified the cause as enhanced contributions due to multihadron, $N\pi$, excited states that have mass gaps smaller than of radial excitations [10, 11]. These contributions had been missed in all prior calculations. Including $N\pi$ excited states in the analysis reduces the disagreement to within 10%, an amount that can be attributed to discretization effects. In this paper, we extend the analysis with $N\pi$ states to the thirteen ensembles described in Table I. Data from various analyses discussed in Sections III A, III B, and IV B are then extrapolated to the physical limit using simultaneous CCFV fits and compared.

In order to extract g_A and $\langle r_A^2 \rangle$, we parameterize the Q^2 behavior of $G_A(Q^2)$ using the dipole, Padé, polynomial ansatz and the model independent z -expansion. We find that the dipole ansatz does not provide a good fit and our final results are obtained using the model independent z -expansion. We show that the pion-pole dominance (PPD) hypothesis Eq. (20) tracks the improvement observed in satisfying the PCAC relation when $N\pi$ states are included in the analysis. We, therefore, use it to parameterize $\tilde{G}_P(Q^2)$ and extract g_P^* and $g_{\pi NN}$ in Sec. IV.

Similarly, the analysis of the ESC in isovector charges extracted from the forward matrix elements is carried out using information from both the 2- and 3-point correlation functions and the non-interacting energy of the lowest $N\pi$ state.

Our final result for the axial form factor, parameterized using the z^2 truncation, is given in Eq. (34); the axial charge obtained from extrapolating it to $Q^2 = 0$ in Eq. (30), and the charge radius in Eq. (31). The results for the induced pseudoscalar charge g_P^* and $g_{\pi NN}$ are given in Eqs. (42) and (43). Lastly, the results for the three isovector charges $g_{A,S,T}^{u-d}$ from the forward matrix elements are given in Eq. (48).

This paper is organized as follows. In section II, we briefly review the notation and the methodology for the extraction of the three form factors: the axial, G_A , the induced pseudoscalar \tilde{G}_P , and the pseudoscalar, G_P , from matrix elements of the axial and pseudoscalar currents within ground state nucleons. In Sec. II B, we explain the three strategies used to remove the ESC to the three-point functions. The analysis of the form factors with respect to how well they satisfy the relations imposed between them by PCAC and the PPD hypothesis is presented in Sec. II C. Based on this analysis, we present our understanding of the excited states that contribute in Sec. II D. The parameterization of the axial form factors as a function of Q^2 and the extraction of the axial charge g_A and the charge radius squared $\langle r_A^2 \rangle$ is carried out in Sec. III. Parameterization of the induced pseudoscalar form factor, \tilde{G}_P , and the extraction of the induced pseudoscalar coupling g_P^* and the pion-nucleon coupling $g_{\pi NN}$ is carried out in Sec. IV. The calculation of the isovector charges $g_{A,S,T}^{u-d}$ from forward matrix elements is described in Sec. V. A summary of our results and a comparison with previous lattice calculations is presented in the concluding section VI. Six appendices give further details of the analysis and the data.

II. METHODOLOGY FOR EXTRACTING THE FORM FACTORS

The ground state matrix elements of the axial $A_\mu = \bar{u}\gamma_\mu\gamma_5 d$ and pseudoscalar $P = \bar{u}\gamma_5 d$ currents between the ground state of the nucleon can be decomposed, in the isospin symmetric limit, into the axial G_A , induced pseudoscalar \tilde{G}_P , and pseudoscalar G_P form factors as

$$\langle N(\vec{p}_f) | A_\mu(\vec{Q}) | N(\vec{p}_i) \rangle = \bar{u}(\vec{p}_f) \left[G_A(Q^2) \gamma_\mu \gamma_5 + q_\mu \gamma_5 \frac{\tilde{G}_P(Q^2)}{2M} \right] u(\vec{p}_i), \quad (1)$$

$$\langle N(\vec{p}_f) | P(\vec{q}) | N(\vec{p}_i) \rangle = \bar{u}(\vec{p}_f) [G_P(Q^2) \gamma_5] u(\vec{p}_i), \quad (2)$$

where $u(\vec{p}_i)$ is the nucleon spinor with momentum \vec{p}_i , $q = p_f - p_i$ is the momentum transferred by the current, $Q^2 = -q^2 = \vec{p}_f^2 - (E(\vec{p}_f) - E(\vec{p}_i))^2$ is the space-like four

Ensemble ID	a (fm)	M_π^{sea} (MeV)	M_π^{val} (MeV)	$L^3 \times T$	$M_\pi^{\text{val}} L$	τ/a	N_{conf}	$N_{\text{meas}}^{\text{HP}}$	$N_{\text{meas}}^{\text{LP}}$
$a15m310$	0.1510(20)	306.9(5)	320.6(4.3)	$16^3 \times 48$	3.93	{5, 6, 7, 8, 9}	1917	7668	122,688
$a12m310$	0.1207(11)	305.3(4)	310.2(2.8)	$24^3 \times 64$	4.55	{8, 10, 12}	1013	8104	64,832
$a12m220S$	0.1202(12)	218.1(4)	225.0(2.3)	$24^3 \times 64$	3.29	{8, 10, 12}	946	3784	60,544
$a12m220$	0.1184(10)	216.9(2)	227.9(1.9)	$32^3 \times 64$	4.38	{8, 10, 12}	744	2976	47,616
$a12m220L$	0.1189(09)	217.0(2)	227.6(1.7)	$40^3 \times 64$	5.49	{8, 10, 12, 14}	1000	4000	128,000
$a09m310$	0.0888(08)	312.7(6)	313.0(2.8)	$32^3 \times 96$	4.51	{10, 12, 14, 16}	2263	9052	114,832
$a09m220$	0.0872(07)	220.3(2)	225.9(1.8)	$48^3 \times 96$	4.79	{10, 12, 14, 16}	964	7712	123,392
$a09m130W$	0.0871(06)	128.2(1)	138.1(1.0)	$64^3 \times 96$	3.90	{8, 10, 12, 14, 16}	1290	5160	165,120
$a06m310$	0.0582(04)	319.3(5)	319.6(2.2)	$48^3 \times 144$	4.52	{16, 20, 22, 24}	1000	8000	64,000
$a06m310W$						{18, 20, 22, 24}	500	2000	64,000
$a06m220$	0.0578(04)	229.2(4)	235.2(1.7)	$64^3 \times 144$	4.41	{16, 20, 22, 24}	650	2600	41,600
$a06m220W$						{18, 20, 22, 24}	649	2596	41,546
$a06m135$	0.0570(01)	135.5(2)	135.6(1.4)	$96^3 \times 192$	3.7	{16, 18, 20, 22}	675	2700	43,200

TABLE I. The parameters of the 2+1+1-flavor HISQ ensembles generated by the MILC collaboration and analyzed in this study are quoted from Ref. [8]. In this clover-on-HISQ study, all fits are made versus M_π^{val} , which is tuned to be close to the Goldstone pion mass M_π^{sea} . The finite-size effects are analyzed in terms of $M_\pi^{\text{val}} L$. The last four columns give the values of the source-sink separation τ used in the calculation of the three-point functions, the number of configurations analyzed, and the number of measurements made using the high precision (HP) and the low precision (LP) truncation of the inversion of the clover operator [12]. On two ensembles, $a06m310$ and $a06m220$, a second set of calculations labeled $a06m310W$ and $a06m220W$, have been done with a larger smearing size σ as described in Ref. [13].

momentum squared transferred. The spinor normalization used is

$$\sum_s u(\mathbf{p}, s) \bar{u}(\mathbf{p}, s) = \frac{E(\mathbf{p}) \gamma_4 - i \boldsymbol{\gamma} \cdot \mathbf{p} + M}{2E(\mathbf{p})}. \quad (3)$$

The process of obtaining the GSME needed in Eqs. (1) and (2) from fits to 2- and 3-point correlation functions is described next.

A. Two- and three-point correlation functions

The lattice calculation starts with the measurement and analysis of the two- and three-point correlation functions $C^{2\text{pt}}(\mathbf{p}; \tau)$ and $C_J(\mathbf{q}, t; \tau)$ constructed using the nucleon interpolating operator χ ,

$$\chi(x) = \epsilon^{abc} \left[q_1^{aT}(x) C \gamma_5 \frac{1 \pm \gamma_4}{2} q_2^b(x) \right] q_1^c(x), \quad (4)$$

where the \pm sign give positive parity states propagating forward/backward in time. The spectral decompositions of the two time-ordered correlation functions are

$$C^{2\text{pt}}(\mathbf{p}; \tau) \equiv \langle \Omega | \mathcal{T}(\chi(\tau) \bar{\chi}(0)) | \Omega \rangle = \sum_{i=0} |A'_i|^2 e^{-E_i \tau}, \quad (5)$$

and

$$\begin{aligned} C_J(\mathbf{q}; t, \tau) &\equiv \langle \Omega | \mathcal{T}(\chi(\tau) J_\Gamma(t) \bar{\chi}(0)) | \Omega \rangle, \\ &= \sum_{i,j=0} A'_i{}^* A_j \langle i' | J_\Gamma | j \rangle e^{-E_i t - M_j(\tau-t)}, \end{aligned} \quad (6)$$

where $J_\Gamma = A_\mu$ or P is the quark bilinear current inserted at time t with momentum \mathbf{q} , and $|\Omega\rangle$ is the vacuum state. In our set up, the nucleon state $|j\rangle$ is, by construction, projected to zero momentum, i.e., $p_j = (E, \mathbf{0})$, whereas $\langle i'|$ is projected onto definite momentum $p_i = (E, \mathbf{p})$ with $\mathbf{p} = -\mathbf{q}$ by momentum conservation. Consequently, the states on the two sides of the inserted operator J are different. The prime in $\langle i'|$ indicates that this state can have non-zero momentum.

For large time separations, τ and $\tau-t$, only the ground state contributes and the ground state matrix element, $\langle 0' | J | 0 \rangle$, whose Lorentz covariant decomposition is given in Eqs. (1) and (2), can be extracted reliably. Assuming this is the case, and choosing the nucleon spin projection to be in the “3” direction, the decompositions become

$$C_{A_i}(\mathbf{q}) \rightarrow K^{-1} \left[-q_i q_3 \frac{\tilde{G}_P}{2M} + \delta_{i3} (M + E) G_A \right], \quad (7)$$

$$C_{A_4}(\mathbf{q}) \rightarrow K^{-1} q_3 \left[(M - E) \frac{\tilde{G}_P}{2M} + G_A \right], \quad (8)$$

$$C_P(\mathbf{q}) \rightarrow K^{-1} q_3 G_P, \quad (9)$$

where $i \in 1, 2, 3$ and the kinematic factor $K^{-1} \equiv \sqrt{2E(E+M)}$. These correlation functions are complex valued, and the signal, for the CP symmetric theory, is in $\text{Im } C_{A_i}$, $\text{Re } C_{A_4}$, and $\text{Re } C_P$.

For a given $\mathbf{q}^2 \neq 0$, the correlators with momentum combinations $\mathbf{q} = (2\pi/L) \mathbf{n} = (2\pi/L)(n_1, n_2, n_3)$ related by cubic symmetry can be averaged to increase the statistics before making fits. We construct the following aver-

ages \bar{A}_μ and \bar{P} :

$$\begin{aligned}\bar{A}_i(\mathbf{q}) &\equiv \frac{1}{\alpha_1 \mathbf{q}^2} \sum_{\mathbf{q}} \text{sgn}(q_i q_3) C_{A_i}(\mathbf{q}) \\ &\rightarrow K^{-1} \frac{\tilde{G}_P}{2M}, \quad (i = 1, 2),\end{aligned}\quad (10)$$

$$\begin{aligned}\bar{A}_{3,L} &\equiv \frac{1}{\alpha_3 \mathbf{q}^2} \sum_{q_3 \neq 0} C_{A_3}(\mathbf{q}) \\ &\rightarrow K^{-1} \left[-\frac{\tilde{G}_P}{2M} + \frac{(N - \beta)}{\alpha_3 \mathbf{q}^2} (M + E) G_A \right],\end{aligned}\quad (11)$$

$$\bar{A}_{3,T} \equiv \frac{1}{\beta} \sum_{q_3=0} C_{A_3}(\mathbf{q}) \rightarrow K^{-1} (M + E) G_A, \quad (12)$$

$$\begin{aligned}\bar{A}_4(\mathbf{q}) &\equiv \frac{1}{\alpha_3 \mathbf{q}^2} \sum_{\mathbf{q}} q_3 C_{A_4}(\mathbf{q}) \\ &\rightarrow K^{-1} \left[(M - E) \frac{\tilde{G}_P}{2M} + G_A \right],\end{aligned}\quad (13)$$

$$\bar{P}(\mathbf{q}) \equiv \frac{1}{\alpha_3 \mathbf{q}^2} \sum_{\mathbf{q}} q_3 C_P(\mathbf{q}) \rightarrow K^{-1} G_P, \quad (14)$$

where $\text{sgn}(x) = x/|x|$ is a sign function with $\text{sgn}(0) = 0$, $\alpha_1 \equiv \sum |n_1 n_3|/n^2$, $\alpha_3 \equiv \sum_{q_3} n_3^2/n^2 = N/3$, $\mathbf{q} = (2\pi/L)\mathbf{n}$, $\beta \equiv \sum_{q_3=0} 1$, and $N \equiv \sum_{\mathbf{q}} 1$ is the number of equivalent momenta averaged.

The pseudoscalar form factor, G_P , is given uniquely by Eq. (14). For a subset of momenta, G_A and \tilde{G}_P are determined uniquely from Eqs. (10) and (12). In general, we solve the over-determined system of equations, Eqs. (10)–(13). Of these, correlators $\bar{A}_{3,L}$ and \bar{A}_4 are nonvanishing for all \mathbf{q} , and are thus sufficient to solve for G_A and \tilde{G}_P . In practice, the A_4 correlator has a poor signal and is dominated by excited states contributions, which we exploit to determine the relevant low-lying excited states. These turn out to be towers of multihadron $N\pi$ and $N\pi\pi$ states. We find that including these states in fits to the spectral decomposition given in Eqs. (6) and (5) is essential for extracting the GSME. With the GSME in hand, the form factors G_A and \tilde{G}_P are determined using Eqs. (10)–(12).

B. Strategies to extract ground state matrix elements

Calculations of nucleon correlation functions face two key challenges. First, the statistical signal-to-noise ratio decays exponentially with the source-sink separation τ as $e^{-(M_N - 1.5M_\pi)\tau}$. This limits current measurements of two-point (three-point) functions to $\lesssim 2$ ($\lesssim 1.5$) fm. Second, at these τ , the ESC are large and the many states that, theoretically, can provide significant contribution are not resolved by the fits to the data. These states arise because the standard nucleon interpolating operator χ , defined in Eq. 4, used to construct the correlation

functions in Eqs. (5) and (6), couples to nucleons and all its excitations including multi-hadron states with positive parity such as $N(\mathbf{p})\pi(-\mathbf{p})$ and $N(\mathbf{0})\pi(\mathbf{0})\pi(\mathbf{0})$. Consequently, the contributions from all these excited states have to be removed to obtain the GSME, $\langle 0'|J|0\rangle$, which we do by fitting the averaged correlators \bar{A}_μ and \bar{P} to Eq. (6). In this work, we construct and compare three fit strategies that differ in the determination of the excited state parameters, i.e., the energies $E_i(\mathbf{q})$ and masses M_i to use in Eq. (6), as explained below.

It is important to emphasize from the very outset that in all fits with each of the three strategies, the excited state amplitudes, $A_i^{(j)}$ and A_j , are not needed since these arise only in the combinations $|A'_i\rangle\langle A_j| \langle i'|J|j\rangle$, which are fit parameters but are not used thereafter in the analysis. Second, the ground state parameters, M_0 , E_0 , A'_0 and A_0 are common for all three strategies and taken from four-state fits to the two-point correlators.

In the standard approach, labeled $\mathcal{S}_{2\text{pt}}$, we take E_i , M_j , A'_0 and A_0 from 4-state fits to $C^{2\text{pt}}$, and input them into an m -state truncation ($m \leq n$) of Eq. (6) to extract the matrix element $\langle 0'|J|0\rangle$. In this paper, we truncate the spectral decompositions given in Eqs. (6) and (5) at $m = 3$ and $n = 4$, respectively.

The second strategy, labeled \mathcal{S}_{A4} , was proposed in Ref. [9]. Again E_0 , M_0 , A'_0 and A_0 are taken from 4-state fits to $C^{2\text{pt}}$, however, E_1 and M_1 are determined from two-state fits to the three-point correlator \bar{A}_4 . The output E_1 and M_1 are then fed into the fits to the other four correlation functions defined in Eqs. (10)–(12), (14). This strategy assumes that the same [first] excited state parameters apply to all five correlation functions, and these are given by fits to \bar{A}_4 .

The third strategy \mathcal{S}_{sim} is similar to \mathcal{S}_{A4} except that E_1 and M_1 are outputs of the simultaneous two-state fits to all five three-point correlators defined in Eqs. (10)–(14). It is, from a statistical point of view, better motivated than \mathcal{S}_{A4} because of the underlying assumption in both cases that the same excited states contribute to all five correlators. It avoids the two-step procedure used in \mathcal{S}_{A4} —first obtain E_1 and M_1 from fits to \bar{A}_4 and then use them in fits to the other four correlators. In \mathcal{S}_{sim} , we used the averaged correlator $\bar{A}_{xy} = (\bar{A}_1 + \bar{A}_2)/2$, since these two correlators are equivalent under cubic rotational symmetry, thus reducing the number of correlators fit simultaneously to four.

The unrenormalized values of the three form factors for each of the three strategies and for the 13 ensembles along with the corresponding Q^2 , are given in Tables X–XXII in Appendix C. Our final results will be presented using the \mathcal{S}_{sim} strategy as explained later.

Comparisons of $G_A(Q^2)$ and the combination $\tilde{G}_P(Q^2) \times (Q^2 + M_\pi^2)/(4M_N^2)$, which should be proportional to G_A according to the PPD hypothesis, obtained using the three strategies $\mathcal{S}_{2\text{pt}}$, \mathcal{S}_{A4} , and \mathcal{S}_{sim} are shown in Figs. 1 and 2. Results for both form factors are consistent between \mathcal{S}_{A4} and \mathcal{S}_{sim} for each of thirteen ensembles while the errors from \mathcal{S}_{sim} are slightly larger.

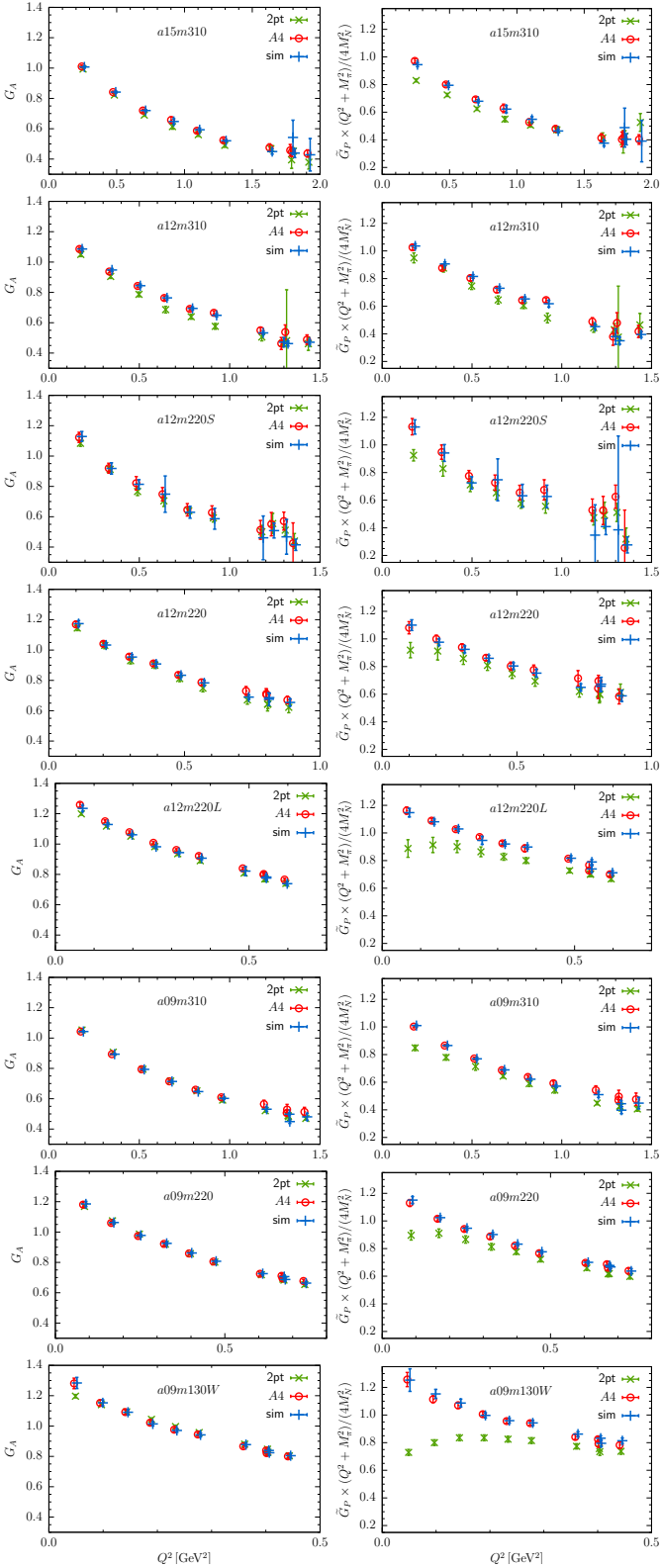


FIG. 1. Data from $a \approx 0.15$, 0.12 and 0.09 fm lattices for the axial form factor G_A (left) and $(Q^2 + M_\pi^2)\tilde{G}_P/(4M_N^2)$ (right). In each panel, data obtained using the three strategies \mathcal{S}_{2pt} , \mathcal{S}_{A4} , and \mathcal{S}_{sim} for controlling ESC are compared.

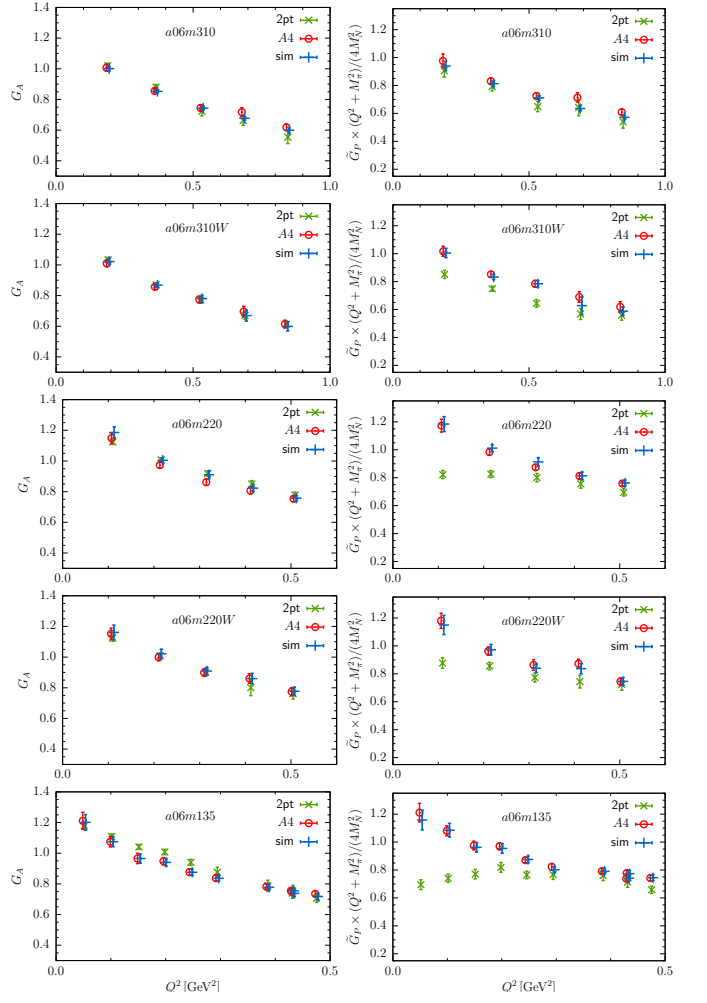


FIG. 2. Data from $a \approx 0.06$ fm lattices for the axial form factor G_A (left) and $(Q^2 + M_\pi^2)\tilde{G}_P/(4M_N^2)$ (right). In each panel, data obtained using the three strategies \mathcal{S}_{2pt} , \mathcal{S}_{A4} , and \mathcal{S}_{sim} for controlling ESC are compared.

On the other hand \tilde{G}_P (and G_P) from strategy \mathcal{S}_{2pt} show noticeable differences that increase as $Q^2 \rightarrow 0$ and $M_\pi^2 \rightarrow 135$ MeV, and these are correlated with the increase in the difference in E_1 and M_1 between \mathcal{S}_{2pt} and \mathcal{S}_{sim} in the same two limits.

Note that the increase in the difference between the three ensembles at the same value of a and M_π , $a12m220S$, $a12m220$, and $a12m220L$, is a simple kinematic effect, i.e., the Q^2 for a given \mathbf{n} decreases as the lattice volume is increased.

A small difference is also observed in G_A extracted using the three strategies. A detailed analysis of the extrapolation of these G_A to $Q^2 \rightarrow 0$ is presented in Sec. III, and the marked improvement in the G_A , \tilde{G}_P , and G_P satisfying the PCAC relation and the PPD hypothesis for the \mathcal{S}_{A4} and \mathcal{S}_{sim} strategies is discussed next in Sec. II C.

C. The PCAC relation and pion-pole dominance

In this section, we evaluate how well the form factors from the three strategies satisfy the PCAC relation, which written in terms of the bare axial, $A_\mu(x)$, and pseudoscalar, $P(x)$, currents is:

$$\partial_\mu A_\mu = 2\hat{m}P, \quad (15)$$

where the quark mass parameter $\hat{m} \equiv Z_m m_{ud} Z_P Z_A^{-1}$ includes all the renormalization factors, and $m_{ud} = (m_u + m_d)/2 = m_l$ is the light quark mass in the isospin symmetric limit. Using the decomposition in Eqs. (1) and (2) of GSME, the PCAC relation requires that the three form factors G_A , \tilde{G}_P , and G_P satisfy, up to discretization errors, the relation

$$2M_N G_A(Q^2) - \frac{Q^2}{2M_N} \tilde{G}_P(Q^2) = 2\hat{m} G_P(Q^2), \quad (16)$$

which we rewrite as

$$R_1 + R_2 = 1, \quad (17)$$

with

$$R_1 = \frac{Q^2}{4M_N^2} \frac{\tilde{G}_P(Q^2)}{G_A(Q^2)}, \quad (18)$$

$$R_2 = \frac{\hat{m}}{M_N} \frac{G_P(Q^2)}{G_A(Q^2)}. \quad (19)$$

The PPD hypothesis relates \tilde{G}_P to G_A as

$$R_3 \equiv \frac{Q^2 + M_\pi^2}{4M_N^2} \frac{\tilde{G}_P(Q^2)}{G_A(Q^2)} = 1. \quad (20)$$

Tests of whether the form factors satisfy the PCAC ($R_1 + R_2 = 1$) and PPD ($R_3 = 1$) relations are presented in Fig. 3 and Fig. 4, respectively. Data with the \mathcal{S}_{2pt} strategy show about 10% deviation for both the PPD and PCAC relations for $Q^2 > 0.3 \text{ GeV}^2$. Below it, the deviation grows to about 40% at the lowest Q^2 point on the two physical pion mass ensembles.

There is a very significant reduction in the deviations for both the \mathcal{S}_{A4} and \mathcal{S}_{sim} strategies for $Q^2 < 0.3 \text{ GeV}^2$. In fact, except for three $M_\pi \approx 220 \text{ MeV}$ ensembles, data below $Q^2 = 1 \text{ GeV}^2$ is essentially independent of Q^2 and the deviations from unity and the variations between ensembles is in most cases within about 5%, which can be accounted for by possible discretization errors. The differences between data with \mathcal{S}_{sim} and \mathcal{S}_{A4} are much smaller. Also, the improvement in the PPD relation, Eq. (20) tracks that in PCAC, Eq. (17).

We point out a caveat in our clover-on-HISQ calculation of the quark mass \hat{m} used in Eq. (16). For four ensembles, $a12m310$, $a09m130W$, $a06m220$, and $a06m135$ we have calculated \hat{m}^{2pt} using the following ratio of pion two-point correlators,

$$2\hat{m}^{2pt} = \frac{\langle \Omega | \partial_\mu A_\mu(t) P(0) | \Omega \rangle}{\langle \Omega | P(t) P(0) | \Omega \rangle}. \quad (21)$$

ID	am_{ud}^{sea}	$a\hat{m}^{2pt}$
<i>a15m310</i>	0.013	-
<i>a12m310</i>	0.0102	0.0121
<i>a12m220L</i>	0.00507	-
<i>a12m220</i>	0.00507	-
<i>a12m220S</i>	0.00507	-
<i>a09m310</i>	0.0074	-
<i>a09m220</i>	0.00363	-
<i>a09m130W</i>	0.0012	0.0015
<i>a06m220</i>	0.0024	0.0028
<i>a06m135</i>	0.00084	0.00088

TABLE II. Ensemble sea quark mass is given in the second column. The quark mass \hat{m} is calculated from Eq. (21)

For the other ensembles, the data for these two-point functions were not collected, so we use the HISQ sea quark mass am_{ud}^{sea} for \hat{m} since for staggered fermions, in fact all lattice fermions with chiral symmetry, $Z_m Z_P Z_A^{-1} = 1$. These quark masses are given in Table II and we find that \hat{m}^{2pt} is 5 – 20% larger than am_{ud}^{sea} , which is not unexpected for our clover-on-HISQ calculation. Noting that $R_2 \approx 0.5R_1$ (see Fig. [15] of Ref. [14]), such a 20% systematic error would increase $R_1 + R_2$ by about 7%. This would bring the data from the physical mass ensembles, *a09m130W* and *a06m135*, in better agreement but would not alter our conclusion that form factors obtained with \mathcal{S}_{A4} and \mathcal{S}_{sim} strategies show better agreement with the PCAC relation compared to \mathcal{S}_{2pt} . Also, \hat{m} does not enter in the PPD relation, Eq. (20), and the deviation from unity of the PPD relation with \mathcal{S}_{A4} and \mathcal{S}_{sim} data is observed to be smaller than seen in the PCAC relation as shown in Fig. 4. Equally important, this caveat does not impact the extraction of individual form factors or their subsequent analysis since \hat{m} only enters in the test of how well the three form factors satisfy the PCAC relation, Eq 16.

We further examine whether the deviation from unity in Fig. 3 at small Q^2 is a discretization error. The $\mathcal{O}(a)$ improvement affects only the axial current, $A_\mu \rightarrow A_\mu + c_A a \partial_\mu P$, and adds to the left hand side in Eq. (16) the term $-Q^2 a c_A G_P$, i.e., under improvement, Eq. (16) can be written as

$$M_N \frac{G_A}{G_P} - \frac{Q^2}{4M_N} \frac{\tilde{G}_P}{G_P} = \hat{m} + \frac{1}{2} a c_A Q^2, \quad (22)$$

where the improvement coefficient, c_A , is typically $\mathcal{O}(10^{-2})$ and negative. Thus, this effect is expected to be small for $Q^2 < 1 \text{ GeV}^2$, and will not change our conclusions.

The PPD relation (Eq. (20)) can be derived from PCAC (Eq. (16)) provided

$$R_4 \equiv \frac{4\hat{m}M_N}{M_\pi^2} \frac{G_P}{\tilde{G}_P} = 1. \quad (23)$$

In this case, $R_1 + R_2 = 1$ would also imply $R_3 = 1$. In

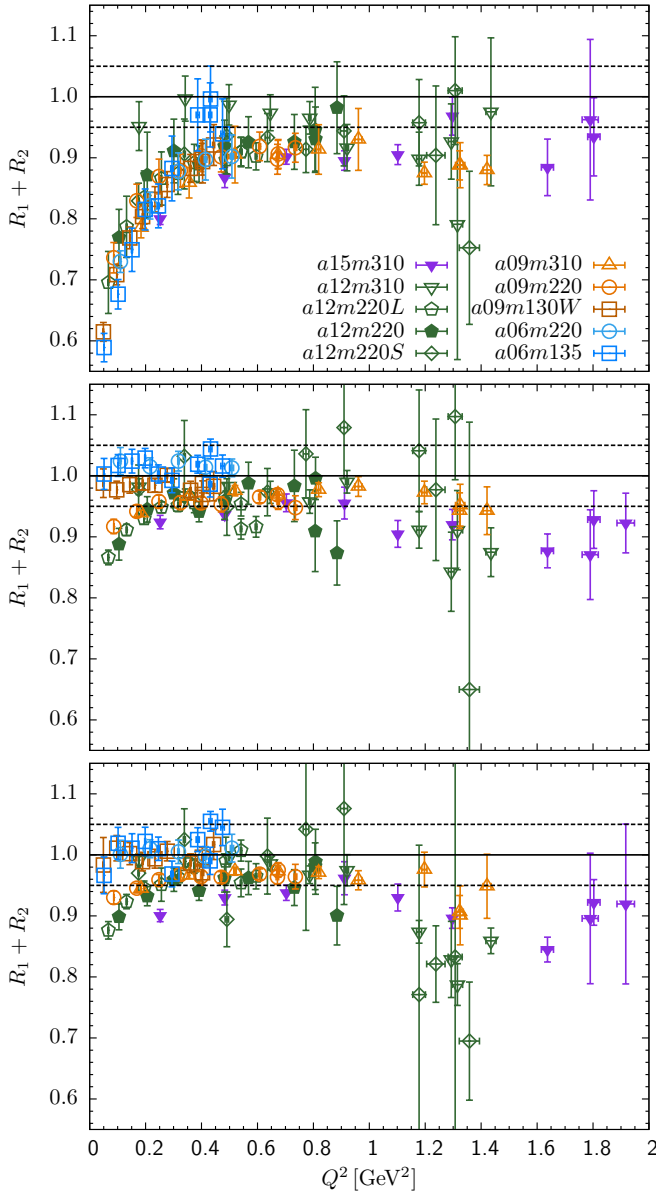


FIG. 3. The data for $R_1 + R_2$, which should equal unity to satisfy PCAC relation, is plotted versus Q^2 for analysis strategies $\mathcal{S}_{2\text{pt}}$ (top), \mathcal{S}_{A4} (middle), and \mathcal{S}_{sim} (bottom). The PCAC relation, Eqs.(15) and (16), requires $R_1 + R_2 = 1$ up to discretization errors. The dashed lines give the $\pm 5\%$ deviation band.

Fig. 5, we compare R_4 from the three strategies for all ensembles except $a06m220W$, $a06m310$, and $a06m310W$ where G_P is not available. We note a roughly linear increase in R_4 with Q^2 , which is consistent with the behavior observed in Ref. [7] and with the analysis of the Goldberger-Trieman discrepancy using χPT in Ref. [15]. Lastly, we note that the data for R_4 from all three strategies, $\mathcal{S}_{2\text{pt}}$, \mathcal{S}_{A4} and \mathcal{S}_{sim} , overlap implying that the changes in \hat{G}_P and G_P , both of which have a pion pole, between different treatments of ESC ($\mathcal{S}_{2\text{pt}}$ versus \mathcal{S}_{A4} or \mathcal{S}_{sim}) cancel in the ratio R_4 within our statistics. This ob-

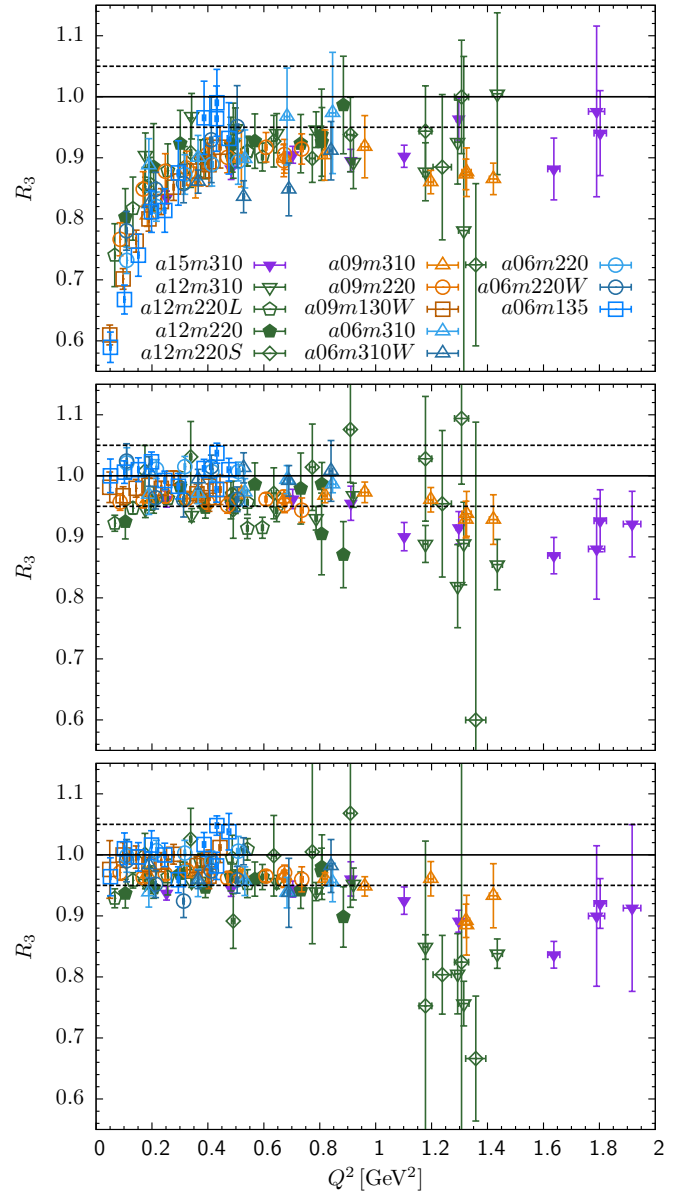


FIG. 4. The ratio R_3 , which should be unity for the pion-pole dominance hypothesis to be satisfied, is plotted versus Q^2 for analysis strategies $\mathcal{S}_{2\text{pt}}$ (top), \mathcal{S}_{A4} (middle), and \mathcal{S}_{sim} (bottom). The dashed lines mark the $\pm 5\%$ deviation band.

servation supports our hypothesis that the same excited states contribute to all five correlation functions.

D. Excited States Spectrum

In Fig. 6 we show data for the energy gaps, ΔE_1 and ΔM_1 on the two sides of the operator insertion for the various ensembles, including the two physical pion mass ones, $a09m130W$ and $a06m135$. The results for ΔE_1^A and ΔM_1^A , outputs of the simultaneous fits to all five correlators (insertions of A_μ and P) at a given momen-

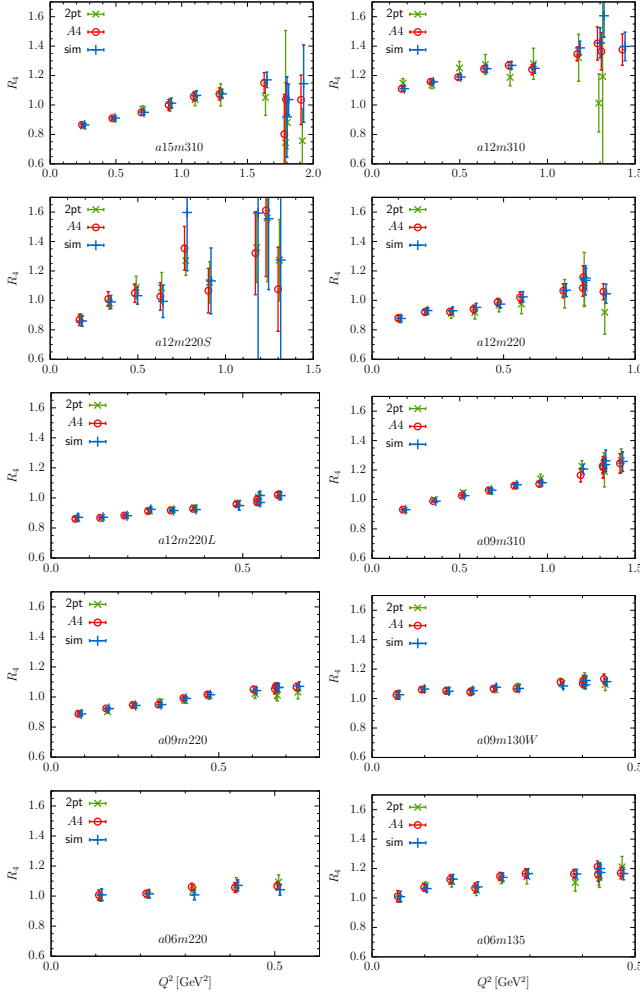


FIG. 5. Results for the ratio $R_4 = (G_P/\tilde{G}_P) \times (4\hat{m}M_N/M_\pi^2)$. For the pion-pole dominance hypothesis to be exact (derivable from the PCAC relation), R_4 should be unity independent of Q^2 . The data show an approximate linear increase with Q^2 , which is consistent with the Goldberger-Trieman discrepancy as discussed in Ref. [7, 15].

tum transfer $\mathbf{p} = 2\pi\mathbf{n}/L$ overlap with the results ΔE_1^{A4} and ΔM_1^{A4} obtained from fits to just C_{A4} . This indicates that the energy gaps in the simultaneous fits are essentially controlled by C_{A4} . The momentum dependence of the data is consistent with the expectation that the relevant excited states on the two sides are $N(\mathbf{n}) + \pi(-\mathbf{n})$ and $N(\mathbf{0}) + \pi(-\mathbf{n})$. This is based on the rough agreement between the data and the corresponding non-interacting energies of these states, ΔM_1 and ΔE_1 , shown by the red and dashed blue lines, respectively, and consistent with the PPD hypothesis that the current injects a pion with momentum \vec{q} .

The data with open circles in Figure 6 are the energy gaps $\Delta E_1^{2\text{pt}}$ obtained from the nucleon two-point correlators. These are roughly independent of momentum and larger than those from \mathcal{S}_{A4} or \mathcal{S}_{sim} fits, especially for the smaller Q^2 points. The difference increases as

$Q^2 \rightarrow 0$ and $M_\pi \rightarrow 0$. This behavior is consistent with $\Delta E_1^{2\text{pt}}$ corresponding to a mixture of radial and higher multiparticle excitation whereas the intermediate excited states identified by the \mathcal{S}_{A4} and \mathcal{S}_{sim} fits, $N(\mathbf{n}) + \pi(-\mathbf{n})$ and $N(\mathbf{0}) + \pi(-\mathbf{n})$, have energy decreasing faster with \mathbf{n} and M_π in those limits. At the same time, when making these identifications, it is very important to qualify that the ΔE_1 and ΔM_1 from the two-state fits in \mathcal{S}_{A4} and \mathcal{S}_{sim} strategies are effectively trying to account for all the intermediate states that make significant contributions and not just the most intuitive ones. Given the size of the effect, improving control over all the excited states that make significant contribution to these correlation functions is key to obtaining precision results for the form factors.

E. Renormalization Constant Z_A

The renormalization constant Z_A for the axial current needed for the form factors G_A and \tilde{G}_P and the charges g_A , g_P^* and $g_{\pi NN}$ was determined non-perturbatively using the RI-SMOM intermediate scheme in Ref. [13]. We use the results given in Table V there.

III. PARAMETERIZATION OF $G_A(Q^2)$, AND THE EXTRACTION OF g_A AND $\langle r_A^2 \rangle$

The axial form factor $G_A(Q^2)$ can be parameterized, near $Q^2 = 0$, by the axial charge g_A and the axial charge radius squared $\langle r_A^2 \rangle$:

$$G_A(Q^2) = g_A(1 - \frac{\langle r_A^2 \rangle}{6} Q^2 + \dots), \quad (24)$$

where $g_A \equiv G_A(0)$ and

$$\langle r_A^2 \rangle \equiv -\frac{6}{g_A} \left. \frac{dG_A(Q^2)}{dQ^2} \right|_{Q^2=0}. \quad (25)$$

To extract these from lattice data obtained at $Q^2 \gtrsim 0.1 \text{ GeV}^2$, one parameterizes the Q^2 dependence of $G_A(Q^2)$. Among the various parameterizations, we study the dipole ansatz and the model-independent z -expansion. The dipole ansatz

$$G_A(Q^2) = \frac{g_A}{(1 + Q^2/\mathcal{M}_A^2)^2}. \quad (26)$$

has two free parameters, the axial charge, $g_A = 1.2766(20)$ known accurately from experiments, and the axial mass \mathcal{M}_A . The z -expansion is a series expansion

$$G_A(Q^2) = \sum_{k=0}^{\infty} a_k z^k, \quad (27)$$

in terms of the variable

$$z = \frac{\sqrt{t_c + Q^2} - \sqrt{t_c + t_0}}{\sqrt{t_c + Q^2} + \sqrt{t_c + t_0}} \quad \text{with } t_c \equiv 9M_\pi^2 \quad (28)$$

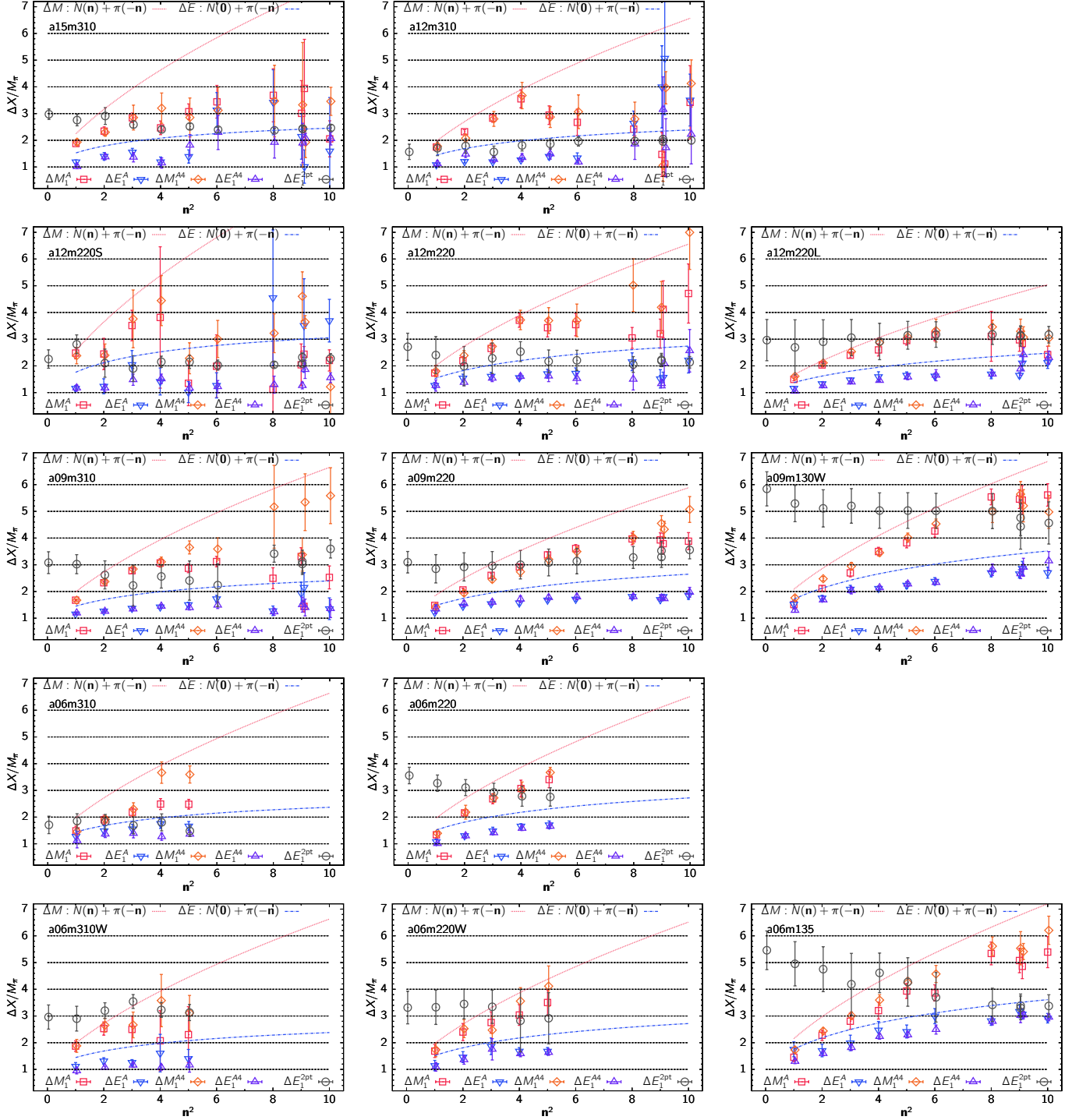


FIG. 6. Results for the energy (mass) gaps ΔE_1 (ΔM_1) for the first excited state extracted from (i) simultaneous fits to axial three-point correlators $C[A_\mu]$ and the pseudoscalar correlator C_P (\mathcal{S}_{sim} strategy and labeled ΔE_1^A and ΔM_1^A), and (ii) from fits to the $C[A_4]$ correlator (\mathcal{S}_{A4} strategy and labeled ΔE_1^{A4} and ΔM_1^{A4}). These mass gaps are compared with the first excited state energy $\Delta E_1^{2\text{pt}}$ from four-state fits to the nucleon two-point correlator. Note that the difference between them, and consequently the difference between the form factors extracted, increases as $M_\pi \rightarrow 135$ MeV.

that maps the kinematically allowed analytical region $Q^2 \geq 0$ to that within a unit circle, $|z| < 1$ [16]. The parameter t_0 is discussed later. For sufficiently small z , fits with the first few terms should suffice. In practice,

to stabilize the fits we impose the condition $|a_k| \leq 5$ [16] for all $z^{k \geq 1}$ truncations.

In our data, the statistical signal is good for momentum transfer with $n^2 \leq 6$ and often poor in the four

points with $8 \leq n^2 \leq 10$. To test the stability of the dipole and z^k fits, we therefore compare the output of the fits to the lowest six versus that to all ten Q^2 points on nine ensembles where data on all ten Q^2 values exist. Observing consistency, the final results are taken from fits to six (five in 4 cases) points.

Estimates using the dipole ansatz from the three ESC strategies are consistent, however, on six ensembles the dipole fits to \mathcal{S}_{sim} and \mathcal{S}_{A4} data have poor p -values. These dipole estimates for g_A and $\langle r_A^2 \rangle$ are smaller than those from z^2 fits to the \mathcal{S}_{sim} and \mathcal{S}_{A4} data. Based on \mathcal{S}_{sim} data showing the best agreement with PCAC, we conclude that the dipole ansatz does not provide a good fit to our data. Henceforth, the dipole results are given only for comparison and do not enter in the final estimates.

Our final results are obtained using the z -expansion. The free parameter t_0 in Eq. (28) is used to adjust the maximum value of z within $|z| \leq 1$. We take $t_0 = 0.4, 0.2, 0.12$ for $M_\pi \approx 310, 220, 130$ MeV ensembles, which gives $|z| \lesssim 0.2$. We have checked that using $t_0 = 0$ does not change the values significantly.

To ensure that the form factors satisfy the expected $1/Q^4$ perturbative behavior in the limit $Q^2 \rightarrow \infty$, sum rules can be imposed as done in Ref. [14]. However, to obtain the behavior near $Q^2 = 0$ from six or ten data points with $Q_{\text{max}}^2 \approx 1 \text{ GeV}^2$, we choose to make fits without the sum rules [17], i.e., to not increase the weight of the larger error high Q^2 points by imposing the sum rules. The z^1 and z^2 fits to $G_A(Q^2)$ from the \mathcal{S}_{sim} strategy are shown in Fig. 13. The resulting bare axial charge $g_A \equiv G_A(0)$ and the charge radius squared $\langle r_A^2 \rangle$ from the z^2 fits are shown in Fig. 7, and the data summarized in Table XXIII in Appendix D. From these data and the z -expansion fits, we conclude the following:

- There is agreement in results between z^2 and z^3 in all cases. To account for the small curvature observed in the data shown in Fig. 13 and yet avoid overparameterization, we will present final results with the z^2 truncation.
- The errors in the data from the two physical mass ensembles $a09m130W$ and $a06m135$ are large and underscore the need for higher statistics.
- Results for both g_A and $\langle r_A^2 \rangle$ from both \mathcal{S}_{A4} and \mathcal{S}_{sim} analyses overlap and increase in value as $M_\pi \rightarrow 135$ MeV. This increase is correlated with the decrease in the mass gap of the $N\pi$ state. A smaller mass gap gives larger ESC.

We take the final results from the \mathcal{S}_{sim} strategy in which a simultaneous fit is made to all five correlators and the form factors come closest to satisfying the PCAC relation as shown in Fig. 3.

The analysis of g_A from the forward matrix element is postponed until Sec. V.

A. Extrapolation of g_A and $\langle r_A^2 \rangle$ to the Physical Point

Extrapolation of the renormalized axial charge g_A and the axial charge radius squared $\langle r_A^2 \rangle$ to the physical point ($a \rightarrow 0$, $M_\pi \rightarrow 135 \text{ MeV}$, $L \rightarrow \infty$) is performed using a simultaneous CCFV fit with the ansatz

$$Y = b_0^Y + b_1^Y a + b_2^Y M_\pi^2 + b_3^Y M_\pi^2 \exp(-M_\pi L), \quad (29)$$

where $Y = \langle r_A^2 \rangle$ or g_A and $\{b_i^Y\}$ denote the corresponding set of fit parameters.

We have performed four CCFV fits: (i) the full set of thirteen ensembles (13-pt), and three “12-pt” fits that exclude (ii) the coarsest lattice point $a15m310$, (iii) the smallest volume point $a12m220S$ that also has large errors, and (iv) the point $a06m135$ that has large statistical errors and shows the largest difference from the other 12 points. The three 12-pt fits are used to estimate systematics due to discretization and finite volume effects, and the impact of the $a06m135$ point. Results of the 13-point CCFV extrapolation for g_A and $\langle r_A^2 \rangle$ are summarized in Table III for six cases: the three strategies used for removing ESC, \mathcal{S}_{sim} , \mathcal{S}_{A4} , and $\mathcal{S}_{2\text{pt}}$, and the two Q^2 parameterizations, z^2 and dipole. The parameters of the 13-point CCFV fit to the \mathcal{S}_{sim} data fit using the z^2 ansatz and used to get the final central values are given in Table XXVI in Appendix E for both g_A and $\langle r_A^2 \rangle$. Results for all the other cases can be constructed using the data for the form factors given in Tables X–XXII in Appendix C.

1. g_A

The central value for g_A , taken from the 13-point CCFV fit shown in Fig. 8 to the \mathcal{S}_{sim} data with z^2 fit, is

$$\begin{aligned} g_A &= 1.296(50)_{\text{stat}}(13)(11) \\ &= 1.296(50)_{\text{stat}}(17)_{\text{sys}}, \quad [z^2]. \end{aligned} \quad (30)$$

The first error is the total analysis uncertainty, and the next two are additional systematic uncertainties: (i) the difference between using z^2 and z^3 fits and (ii) the difference of this central value from the average of the three 12-point CCFV fits. The two systematics are added in quadrature to get the total systematic error given in the second line in Eq. (30). In Section V, this result is compared with an independent analysis of g_A obtained from the forward matrix element, i.e., from the zero momentum correlator, $C_{A_3}(\mathbf{p} = \mathbf{0})$, as defined in Eq. (7).

2. $\langle r_A^2 \rangle$

The CCFV fit to $\langle r_A^2 \rangle$, obtained from the \mathcal{S}_{sim} data with z^2 fit, is shown in Fig. 9 (top panels). It gives

$$\langle r_A^2 \rangle = 0.418(33)_{\text{stat}}(29)(18) \text{ fm}^2$$

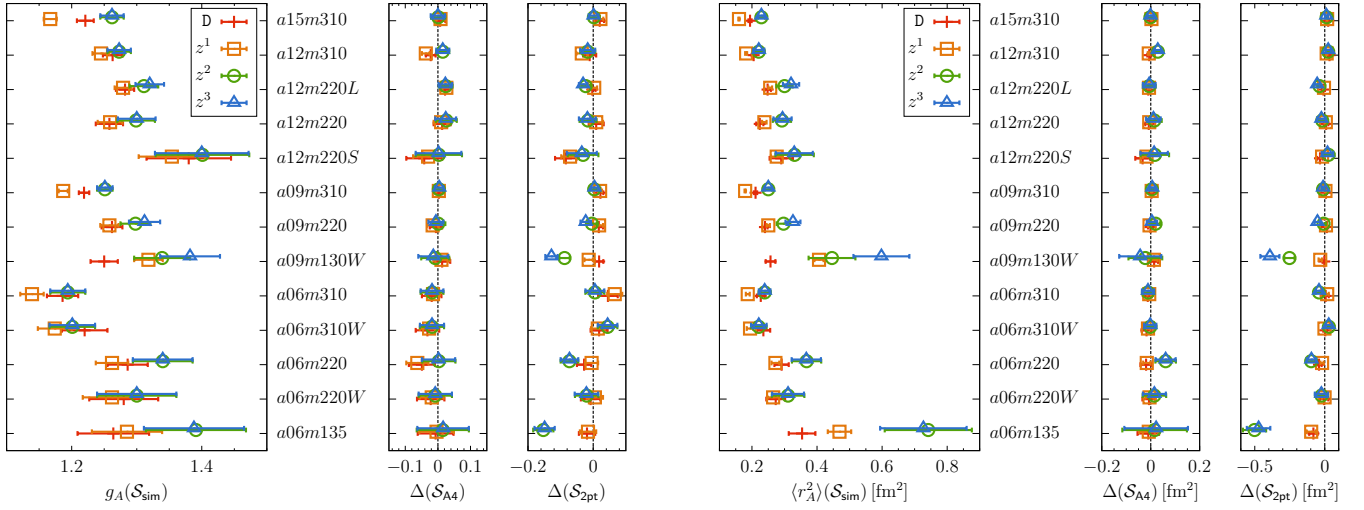


FIG. 7. (Left) Results for bare g_A from the strategy \mathcal{S}_{sim} and the differences $\Delta(\mathcal{S}_{A4}) = g_A|_{\mathcal{S}_{A4}} - g_A|_{\mathcal{S}_{\text{sim}}}$ and $\Delta(\mathcal{S}_{2\text{pt}}) = g_A|_{\mathcal{S}_{2\text{pt}}} - g_A|_{\mathcal{S}_{\text{sim}}}$. To facilitate visualization of the spread, the errors plotted for $\Delta(X)$ are those in $g_A(X)$. Results are shown for the dipole fit labeled “D” and $z^{1,2,3}$ -truncations. (Right) Analogous results for $\langle r_A^2 \rangle$.

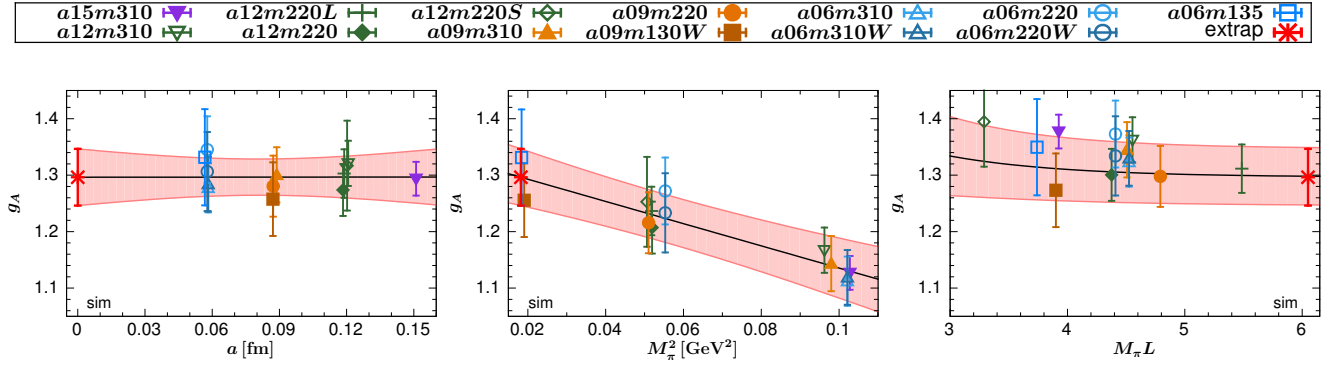


FIG. 8. The axial charge g_A given by the 13-pt CCFV fit to \mathcal{S}_{sim} data using the z^2 fit to $G_A(Q^2 \neq 0)$. The pink band in each panel gives the result of the CCFV fit (Eq. 29) versus the x-axis variable with the other two variables set to their physical values. The data points in each panel have been shifted in the other two variables using the same CCFV fit, however, the size of errors are not changed. The final result at the physical point is shown by the red cross.

$$=0.418(33)_{\text{stat}}(34)_{\text{sys}} \text{ fm}^2, \quad [z^2] \quad (31)$$

B. $G_A(Q^2)$ at the Physical Point

with the errors derived in the same way as for g_A .

For both g_A and $\langle r_A^2 \rangle$, the largest dependence in the CCFV fit is on M_π^2 for the \mathcal{S}_{sim} and \mathcal{S}_{A4} strategies. This is a consequence of the increasing influence of the $N\pi$ state as $M_\pi \rightarrow 0$ due to the decrease in its mass gap. In contrast, the $\mathcal{S}_{2\text{pt}}$ data, which do not include the $N\pi$ state in the analysis, show mild dependence on all three variables $\{a, M_\pi, M_\pi L\}$.

Estimates from the 12-pt CCFV fit excluding the $a06m135$ point, shown in the bottom panels of Fig. 9, are consistent with the 13-point results, not unexpected since the errors in the $a06m135$ point are large. Clearly, to further improve the estimates of both g_A and $\langle r_A^2 \rangle$ requires much higher statistics data at small Q^2 on the physical pion-mass ensembles.

The Q^2 dependence of the axial form factor up to 1 GeV^2 , obtained at the physical point, is shown in Fig. 10 for the three strategies $\mathcal{S}_{2\text{pt}}$, \mathcal{S}_{A4} , and \mathcal{S}_{sim} . The pink band in these figures was obtained using the following three step process. First, starting with the lattice data for $G_A(Q^2)/g_A$ on each of the thirteen ensembles, which does not need renormalization and are at different discrete values of Q^2 , we fit them using the z^2 -ansatz (see Eq. (27)). The result of these fits was taken to specify $G_A(Q^2)/g_A$ for $0 < Q^2 \leq 1 \text{ GeV}^2$. Second, we chose a set of eleven Q^2 values evenly distributed over this range, and for each of these Q^2 values carried out a CCFV extrapolation of the thirteen points using Eq. (29). The result was taken to be the value of G_A/g_A at that Q^2 at the physical point. In each of these CCFV fits, the data are assumed to be uncorrelated as the thirteen ensembles

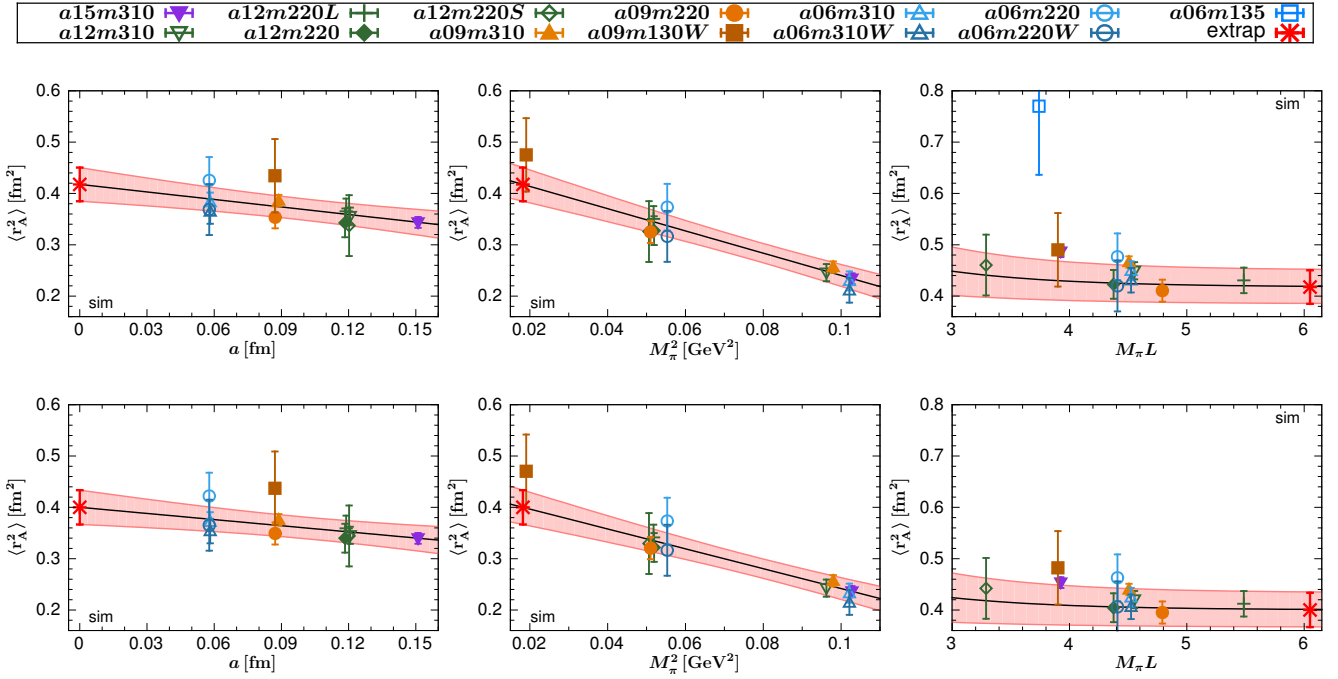


FIG. 9. (Top panels) The axial charge radius squared $\langle r_A^2 \rangle$ given by the 13-pt CCFV fit to data obtained using the z^2 fit to $G_A(Q^2 \neq 0)$ with the \mathcal{S}_{sim} strategy. (Bottom panels) The 12-pt fit without the $a06m135$ point (open blue square present only in the top of the right panel) that has large errors. The pink band in each panel gives the result of the CCFV fit (Eq. 29) versus the x-axis variable with the other two variables set to their physical values. The data points in each panel have been shifted using the same CCFV fit, however, the size of errors are not changed. The final result at the physical point is shown by the red cross.

g_A	z^2	dipole
\mathcal{S}_{sim}	1.296(50)(13)(11)	1.239(43)(-)(39)
\mathcal{S}_{A4}	1.281(51)(11)(21)	1.204(44)(-)(21)
$\mathcal{S}_{2\text{pt}}$	1.213(39)(02)(-)	1.228(37)(-)(-)
$\langle r_A^2 \rangle$	z^2	dipole
\mathcal{S}_{sim}	0.418(33)(29)(18)	0.305(13)(-)(06)
\mathcal{S}_{A4}	0.428(31)(21)(19)	0.305(15)(-)(06)
$\mathcal{S}_{2\text{pt}}$	0.282(27)(16)(-)	0.275(14)(-)(-)

TABLE III. g_A and $\langle r_A^2 \rangle$ from the 13-point CCFV fit. Results are given for the z^2 and dipole fits to $G_A(Q^2 \neq 0)$, and for the three strategies used to control ESC. In each case, in addition to the central value and the total analysis error, the two systematic errors are the difference between the z^2 and z^3 estimates, and the difference from the 12-pt CCFV fits explained in the Sec. III A.

are independent calculations. Third, these eleven extrapolated points are fit by the z^2 ansatz to obtain the final parameterization valid in the interval $0 \leq Q^2 \leq 1.0 \text{ GeV}^2$ that is shown by the pink band in Fig. 10. The errors in the original lattice data are fully propagated through this three step process carried out within a single bootstrap setup. They do not include possible uncertainty due to incomplete removal of ESC or due to using only the leading order CCFV fit ansatz.

Figure 10 also shows the experimental bubble chamber data and the dipole ansatz with $M_A = 1.026(21) \text{ GeV}$ extracted from it (green band) [15]. A recent analysis of the ν -deuterium data [18] finds a $\approx 10\times$ larger uncertainty. As already shown, only the lattice data with the $\mathcal{S}_{2\text{pt}}$ strategy is roughly consistent with a dipole ansatz with $M_A \approx 1.30 \text{ GeV}$, but the three form factors extracted using it fail to satisfy the PCAC relation. So the reader should regard our showing of the dipole curves with $M_A = 1.026, 1.2$ and 1.35 GeV as only for comparison.

Estimates using \mathcal{S}_{A4} and \mathcal{S}_{sim} strategies are consistent, and show a more rapid fall for $Q^2 \lesssim 0.3 \text{ GeV}^2$, roughly consistent with the dipole ansatz with $M_A = 1.026(21) \text{ GeV}$ (and therefore a larger $\langle r_A^2 \rangle$), and then level off falling more slowly. Note, however, that the data for $Q^2 > 0.5 \text{ GeV}^2$ come mainly from the heavier $M_\pi \approx 310 \text{ MeV}$ ensembles. At these heavy pion masses, the mass gap of the $N\pi$ state is large and close to the $\mathcal{S}_{2\text{pt}}$ values as shown in Fig. 6. To obtain data for $Q^2 > 0.5 \text{ GeV}^2$ on physical pion mass ensembles with $M_\pi L > 4$ requires going to large values of \mathbf{q} , where statistical and discretization errors are large with the methodology used in this work. A more promising method for generating data at large Q^2 is momentum smearing [19]. Also, when including points with larger Q^2 , the z -expansion fits with and without sum-rules should

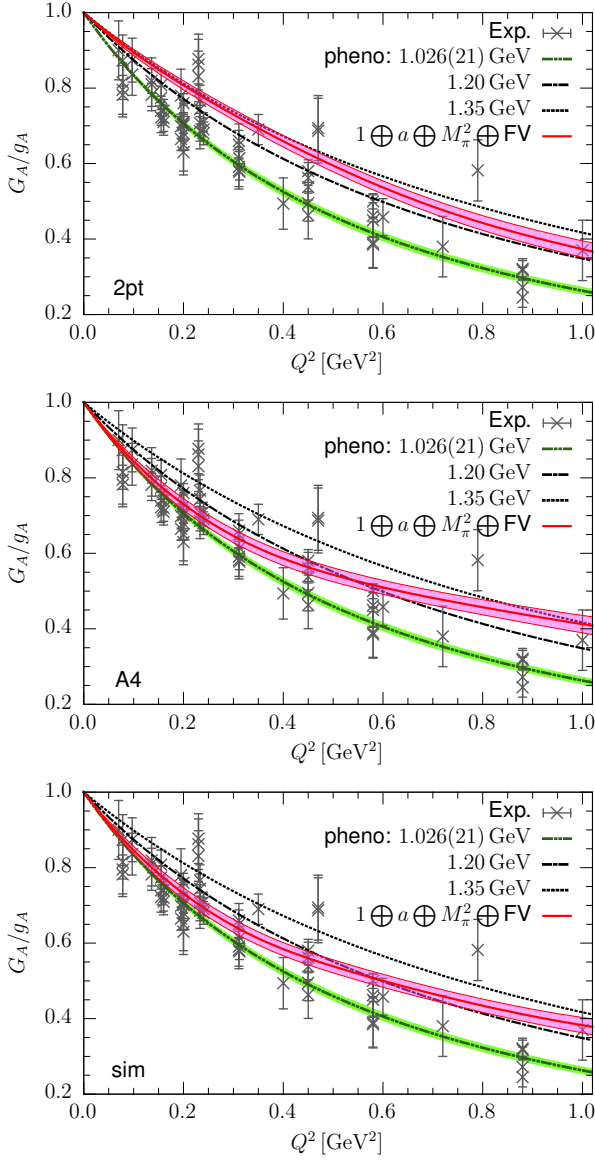


FIG. 10. Results for G_A/g_A at the physical point for the three strategies \mathcal{S}_{2pt} , \mathcal{S}_{A4} and \mathcal{S}_{sim} (labelled “2pt”, “A4”, and “sim”, respectively) used to control the excited-state contamination. The three step process used to get these results shown by the pink band is described in the text. In each case, the error band represents the full analysis error for that strategy but with the value at $Q^2 = 0$ fixed to unity. The label $1 \oplus a \oplus M_\pi^2 \oplus FV$ specifies that all 4 terms in the CCFV ansatz, Eq. 29, were kept. The experimental ν -deuterium data (gray crosses labeled Exp.) were provided by Ulf Meissner and the dipole result $M_A = 1.026(21)$ GeV is taken from Ref. [15]. This and the two other dipole fit with $M_A = 1.20$ and 1.35 GeV are shown only for comparison.

be compared since it is not known, a priori, when the $1/Q^4$ asymptotic behavior becomes significant.

The coefficients b_i in the CCFV ansatz given in Eq. (29) are shown in Fig. 11 for the three strategies \mathcal{S}_{2pt} , \mathcal{S}_{A4} , and \mathcal{S}_{sim} . The coefficients $b_1(Q^2)$ and $b_2(Q^2)$

are similar within errors for \mathcal{S}_{sim} and \mathcal{S}_{A4} , significantly different from zero, and qualitatively different from the case \mathcal{S}_{2pt} .

To provide our best parameterization of G_A for phenomenology, we repeated the above procedure for $G_A(Q^2)$ obtained with the \mathcal{S}_{sim} strategy. Again, the data after extrapolation to the continuum limit at $Q^2 = 0, 0.1, 0.2, \dots, 1.0$ GeV² were fit with a z^2 ansatz, $t_c = 9M_\pi^2$, and $t_0 = 0.25$ GeV². The result, shown in Fig. 12, has the parameterization

$$G_A(Q^2) = a_0 + a_1 z + a_2 z^2 \\ = 0.876(28) - 1.669(99)z + 0.483(498)z^2, \quad (32)$$

with the correlation matrix:

$$\begin{matrix} & a_0 & a_1 & a_2 \\ \begin{matrix} a_0 \\ a_1 \\ a_2 \end{matrix} & \begin{pmatrix} 1.0 & -0.45170 & -0.02966 \\ -0.45170 & 1.0 & -0.24394 \\ -0.02966 & -0.24394 & 1.0 \end{pmatrix} \end{matrix} \quad (33)$$

This fit gives

$$g_A = 1.281(53), \\ \langle r_A^2 \rangle = 0.498(56) \text{ fm}^2, \quad (34)$$

which are consistent with the estimates in Eqs. (30) and (31), *albeit* with an $\approx 1\sigma$ larger $\langle r_A^2 \rangle$.

We also carried out this final z^2 fit setting $t_0 = 0$ in the definition of z . The results are

$$g_A = 1.282(54) \\ \langle r_A^2 \rangle = 0.505(66) \text{ fm}^2. \quad (35)$$

While consistent, the coefficient c_2 in this fit is essentially undetermined. We, therefore, choose the results given in Eq. (34).

For our final results from the analysis of G_A , we take the average weighted by the “stat” errors of values given in Eqs. (30), (31) and (34) to get

$$g_A = 1.289(53)_{\text{stat}}(17)_{\text{sys}} \\ \langle r_A^2 \rangle = 0.439(56)_{\text{stat}}(34)_{\text{sys}} \text{ fm}^2. \quad (36)$$

For errors, we take the larger of the “stat” error and keep the “sys” errors given in Eqs. (30) and (31).

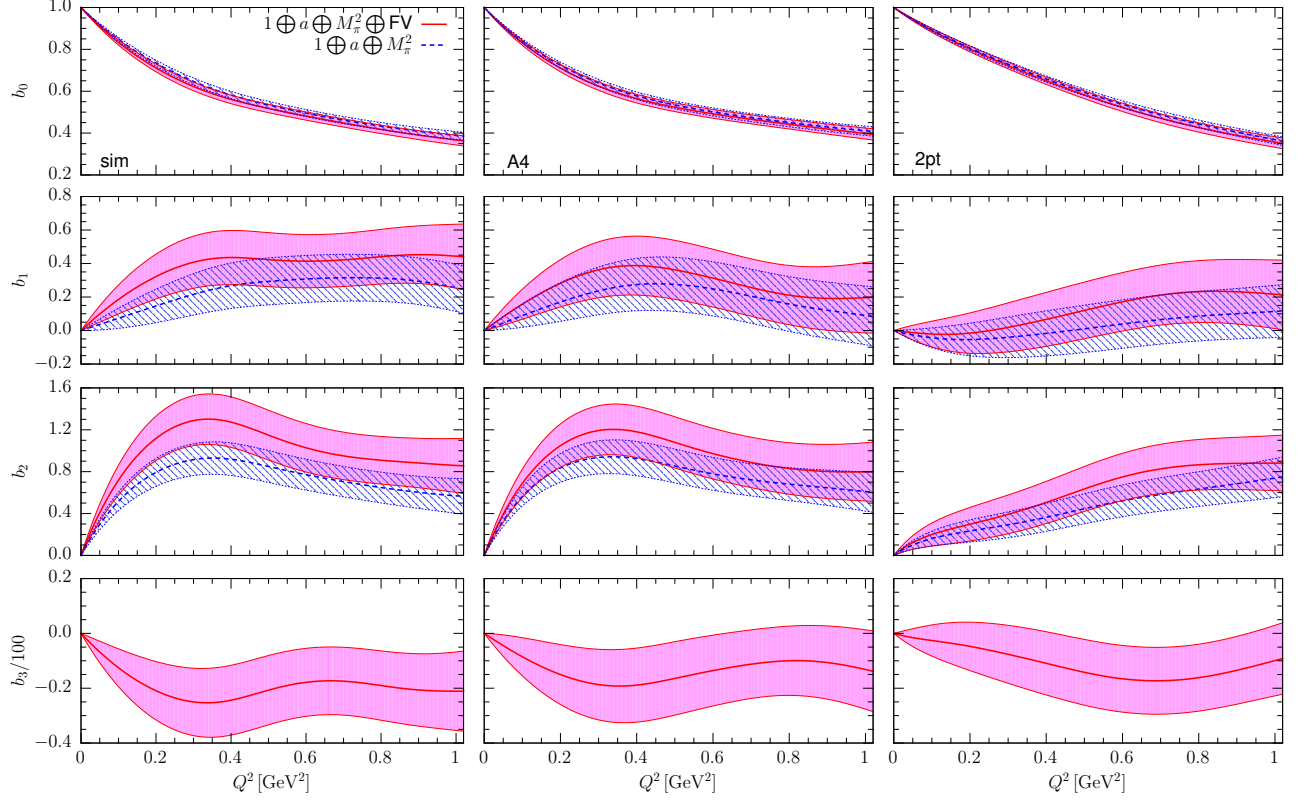


FIG. 11. The fit coefficients b_i , $i = 0, 1, 2, 3$, defined in Eq. (29), for the CCFV extrapolation of the axial form factor $G_A(Q^2)/g_A$ obtained with strategy \mathcal{S}_{sim} (left), \mathcal{S}_{A4} (middle) and $\mathcal{S}_{2\text{pt}}$ (right) and fit with the z^2 truncation. The extrapolated $G_A(Q^2)/g_A$ with \mathcal{S}_{sim} is shown in Fig. 10.

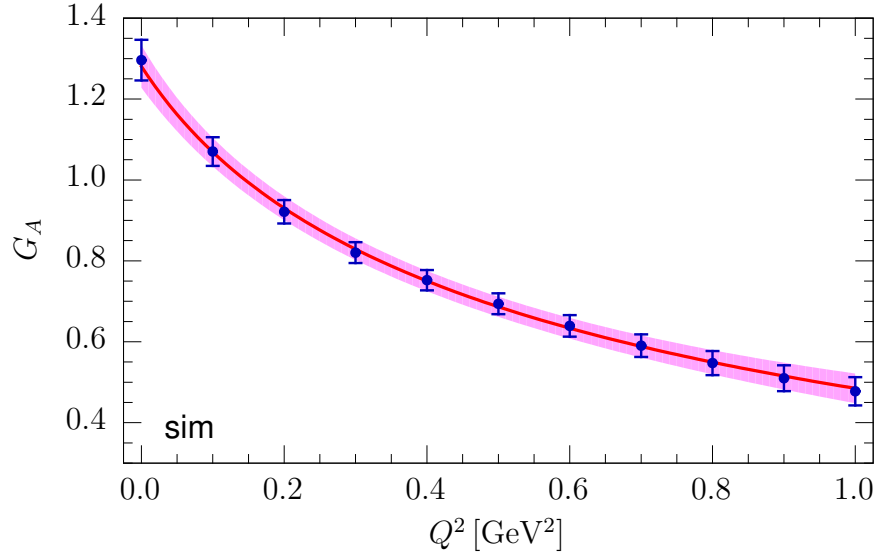


FIG. 12. The final estimate of $G_A(Q^2)$ at the physical point. The eleven fiducial points used to make the fit are shown in blue and their errors are given by the one overall bootstrap analysis covering the three step process described in the text. The parameterization is given in Eq. (32).

IV. COUPLINGS g_P^* AND $g_{\pi NN}$ FROM THE INDUCED PSEUDOSCALAR FORM FACTOR

The induced pseudoscalar coupling g_P^* is defined as

$$g_P^* \equiv \frac{m_\mu}{2M_N} \tilde{G}_P(Q^{*2}), \quad (37)$$

where m_μ is the muon mass and $Q^{*2} = 0.88m_\mu^2$ is the energy scale of muon capture. Similarly, the pion-nucleon coupling $g_{\pi NN}$ is obtained from the residue of $\tilde{G}_P(Q^2)$ at the pion pole through the relation

$$\begin{aligned} g_{\pi NN} &\equiv \lim_{Q^2 \rightarrow -M_\pi^2} \frac{M_\pi^2 + Q^2}{4M_N F_\pi} \tilde{G}_P(Q^2) \\ &= \frac{\tilde{F}_P(-M_\pi^2) M_N}{F_\pi}, \end{aligned} \quad (38)$$

where $F_\pi = 92.9$ MeV is the pion decay constant. The function \tilde{F}_P is \tilde{G}_P without the pion pole, and is defined as

$$\tilde{F}_P(Q^2) \equiv \frac{Q^2 + M_\pi^2}{4M_N^2} \tilde{G}_P(Q^2). \quad (39)$$

It would equal G_A if PPD were exact. This, as defined in Eq. (20), requires $R_3 = \tilde{F}_P/G_A = 1$. The data for R_3 , plotted in Fig. 4, deviates from unity for $\mathcal{S}_{2\text{pt}}$ while that for \mathcal{S}_{sim} and \mathcal{S}_{A4} strategies is one within expected discretization errors and violations of PPD.

To extract g_P^* and $g_{\pi NN}$ from the lattice data, a parameterization of the Q^2 behavior of \tilde{G}_P and \tilde{F}_P is carried out. A comparison of the z^1 and z^2 fits to G_A and \tilde{F}_P from the \mathcal{S}_{sim} strategy is shown in Fig. 13 for the thirteen ensembles. Results from z^2 and z^3 fits are consistent, indicating convergence, while z^1 fits miss the small curvature seen. To avoid overparameterization, we again take the z^2 results for the central values.

A. Parameterization of $\tilde{G}_P(Q^2)$ and \tilde{F}_P

Based on the PCAC analysis (see Figs. 3), we focus on the $\tilde{G}_P(Q^2)$ data from only the \mathcal{S}_{sim} and \mathcal{S}_{A4} strategies and again give the $\mathcal{S}_{2\text{pt}}$ results only for comparison.

We consider two ways to parameterize $\tilde{G}_P(Q^2)$, both of which build in the pion-pole dominance hypothesis. The first is a small Q^2 expansion

$$\tilde{G}_P(Q^2) = \frac{c_0}{Q^2 + M_\pi^2} + c_1 + c_2 Q^2, \quad (40)$$

where the c_i ($i = 0, 1, 2$) are fit parameters. Results for g_P^* , $g_{\pi NN} F_\pi$ and $g_{\pi NN} F_\pi / M_N$ using this fit (labeled PD) to the \mathcal{S}_{sim} data are given in Table XXIV along with the χ^2/DOF and p -value for the fits. Figure 14 (left) shows the bare g_P^* from the \mathcal{S}_{sim} strategy for five Q^2 parameterizations of \tilde{G}_P and its difference from \mathcal{S}_{A4} and

$\mathcal{S}_{2\text{pt}}$ results. The analogous results for unrenormalized $g_{\pi NN} F_\pi$ are also summarized in Table XXIV for \mathcal{S}_{sim} data fit using z^2 , and shown in Fig. 14 (right).

In the second way, we treat $\tilde{F}_P(Q^2)$ as an analytic function that can be fit using either the dipole ansatz (with free parameters $\tilde{F}_P(0)$ and \tilde{M}_P) or the z -expansion, Eq. (27), with z again defined by Eq. (28). Results for g_P^* , $g_{\pi NN} F_\pi$ and $g_{\pi NN} F_\pi / M_N$, from z^2 fits to $\tilde{F}_P(Q^2)$ obtained with the \mathcal{S}_{sim} strategy are given in Table XXV and agree with those in Table XXIV.

B. Extrapolation of g_P^* and $g_{\pi NN}$ to the Physical Point

1. g_P^*

Renormalized g_P^* is extrapolated to the physical point in two ways. In the first method $2m_\mu M_N \tilde{F}_P(Q^{*2})$ is extrapolated using the CCFV fit function given in Eq. (29) and multiplied by the pion-pole factor at the physical point:

$$g_P^* = 2m_\mu M_N \tilde{F}_P(Q^{*2}) \Big|_{\text{extrap}} \times \frac{1}{Q^{*2} + M_\pi^2} \Big|_{\text{phys}}. \quad (41)$$

In the second method, extrapolation of g_P^* is carried out by adding the pion-pole term, $b_4^{g_P^*}/(Q^{*2} + M_\pi^2)$, to the CCFV fit function in Eq. (29). The two methods give consistent estimates and their unweighted average is used to get the final results summarized in Table IV for each of the three strategies, \mathcal{S}_{sim} , \mathcal{S}_{A4} , and $\mathcal{S}_{2\text{pt}}$.

The error obtained from the overall analysis is quoted as the first “stat” uncertainty. The systematical errors associated with z -expansion truncation and the largest difference of the central value from the three 12-pt CCFV fits are quoted as the second and third errors. The difference between the two extrapolation methods described above is quoted as the fourth error. For the final result, we take the \mathcal{S}_{sim} data with z^2 fits:

$$\begin{aligned} g_P^* &= 9.03(47)_{\text{stat}}(01)(32)(27), \quad [z^2], \\ &= 9.03(47)_{\text{stat}}(42)_{\text{sys}}. \end{aligned} \quad (42)$$

In the second line, the three systematic errors are combined in quadrature. The 13-pt CCFV fit to the 13 points, obtained using \mathcal{S}_{sim} data fit with z^2 , is shown in Fig. 15.

2. $g_{\pi NN}$

The CCFV extrapolation to obtain $g_{\pi NN}$ is carried out using Eq. (29) for (i) the product $g_{\pi NN} F_\pi (= M_N \tilde{F}_P(-M_\pi^2))$, and the result, in the continuum, divided by $F_\pi = 92.9$ MeV; and (ii) $\tilde{F}_P(-M_\pi^2)$ and the result multiplied by $M_N (= 939 \text{ MeV})/F_\pi (= 92.9 \text{ MeV})$.

g_P^*	z^2	dipole	PD
\mathcal{S}_{sim}	9.03(47)(01)(32)(27)	8.61(39)(-)(19)(23)	8.92(45)(-)(38)(33)
\mathcal{S}_{A4}	8.92(44)(04)(20)(23)	8.70(37)(-)(17)(15)	8.94(43)(-)(28)(33)
$\mathcal{S}_{2\text{pt}}$	4.50(26)(02)(-)(22)	5.36(25)(-)(-)(12)	4.73(27)(-)(-)(10)

TABLE IV. g_P^* from the z^2 -expansion, dipole, and pion-pole dominance (PD) fits. The first column gives the strategy used for extracting the matrix elements. In each, the first error is the total analysis error and the rest are systematic errors explained in the text.

	z^2	dipole	PD
\mathcal{S}_{sim}	14.14(81)(01)(77)(35)	13.03(67)(-)(41)(28)	13.80(81)(-)(99)(33)
\mathcal{S}_{A4}	13.77(79)(07)(33)(29)	13.06(64)(-)(38)(26)	13.90(79)(-)(57)(31)
$\mathcal{S}_{2\text{pt}}$	5.76(57)(00)(-)(10)	7.57(46)(-)(-)(09)	6.24(57)(-)(-)(05)

TABLE V. Results for $g_{\pi NN}$ from the z^2 , dipole, and pion-pole dominance (PD) fits. The first column gives the ESC strategy used to extract the matrix elements. The first error is statistical and the rest are systematic as explained in the text.

These two extrapolations could have different systematics, and as shown in Fig. 15, the slopes with respect to M_π^2 of $g_{\pi NN}F_\pi$ and $\tilde{F}_P(-M_\pi^2)$ are different. These two estimates are averaged to get the $g_{\pi NN}$ for the nine cases summarized in Table V: the three strategies and the three Q^2 fit types.

The central value

$$\begin{aligned} g_{\pi NN} &= 14.14(81)_{\text{stat}}(1)(77)(35) \\ &= 14.14(81)_{\text{stat}}(85)_{\text{sys}}. \quad [z^2] \quad (43) \end{aligned}$$

is taken from the \mathcal{S}_{sim} data with z^2 fits and the errors estimated as for g_P^* .

C. $\tilde{F}_P(Q^2)$ at the Physical Point

The physical point $\tilde{F}_P(Q^2)$ was obtained following the same three step procedure used for extrapolating $G_A(Q^2)$ that is described in Sec. III B. This $\tilde{F}_P(Q^2)$ and the fit parameters, $b_i(Q^2)$, in the CCFV extrapolation are shown up to 1 GeV^2 in Figs. 16 and 17, respectively, for data obtained with the \mathcal{S}_{sim} strategy.

Figure 16 also provides a comparison with the $G_A(Q^2)$ already shown in Fig. 12. If PPD is exact, then \tilde{F}_P should equal G_A . The overlap of the two bands turns out to be surprisingly good over the whole Q^2 interval.

Similar to $G_A(Q^2)$, the two physical mass ensembles impact the coefficients $b_i(Q^2)$ shown in Fig. 17 only for $Q^2 \lesssim 0.4 \text{ GeV}^2$. The plots show some pion mass dependence for $Q^2 < 0.2 \text{ GeV}^2$, i.e., $b_2(Q^2) \neq 0$. The coefficients for the lattice spacing dependence, $b_1(Q^2)$, and for finite volume, $b_3(Q^2)$, have large uncertainty. Also, neglecting the finite volume term does not change $b_1(Q^2)$ and $b_2(Q^2)$ significantly. Overall, the shape of these coefficients versus Q^2 is somewhat different from those for G_A shown in Fig. 11.

The z^2 fit to the physical point \tilde{F}_P , shown in Fig. 16, with $t_c = 9M_\pi^2$ and $t_0 = 0.25 \text{ GeV}^2$ has the parameterization

$$\begin{aligned} \tilde{F}_P(Q^2) &= a_0 + a_1 z + a_2 z^2 \\ &= 0.868(30) - 1.702(136)z + 0.587(601)z^2, \quad (44) \end{aligned}$$

with the correlation matrix:

$$\begin{matrix} & a_0 & a_1 & a_2 \\ \begin{matrix} a_0 \\ a_1 \\ a_2 \end{matrix} & \begin{pmatrix} 1.0 & -0.45085 & -0.05106 \\ -0.45085 & 1.0 & -0.23890 \\ -0.05106 & -0.23890 & 1.0 \end{pmatrix} \end{matrix} \quad (45)$$

The agreement, within errors, with the parameterization of $G_A(Q^2)$ given in Eqs. (32) and (33) is surprisingly good.

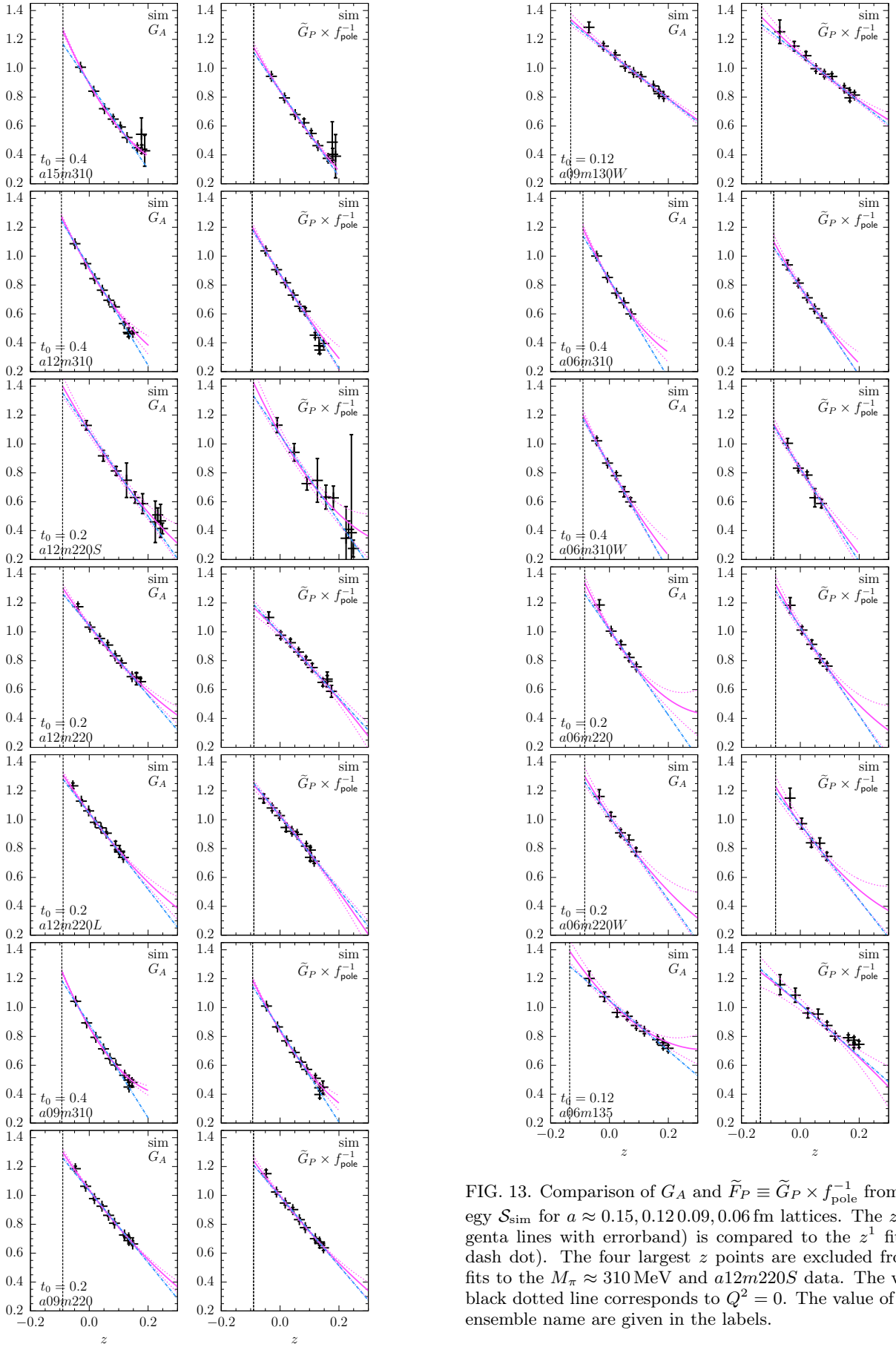


FIG. 13. Comparison of G_A and $\tilde{F}_P \equiv \tilde{G}_P \times f_{\text{pole}}^{-1}$ from strategy \mathcal{S}_{sim} for $a \approx 0.15, 0.12, 0.09, 0.06$ fm lattices. The z^2 (magenta lines with errorband) is compared to the z^1 fit (blue dash dot). The four largest z points are excluded from the fits to the $M_\pi \approx 310$ MeV and $a12m220S$ data. The vertical black dotted line corresponds to $Q^2 = 0$. The value of t_0 and ensemble name are given in the labels.

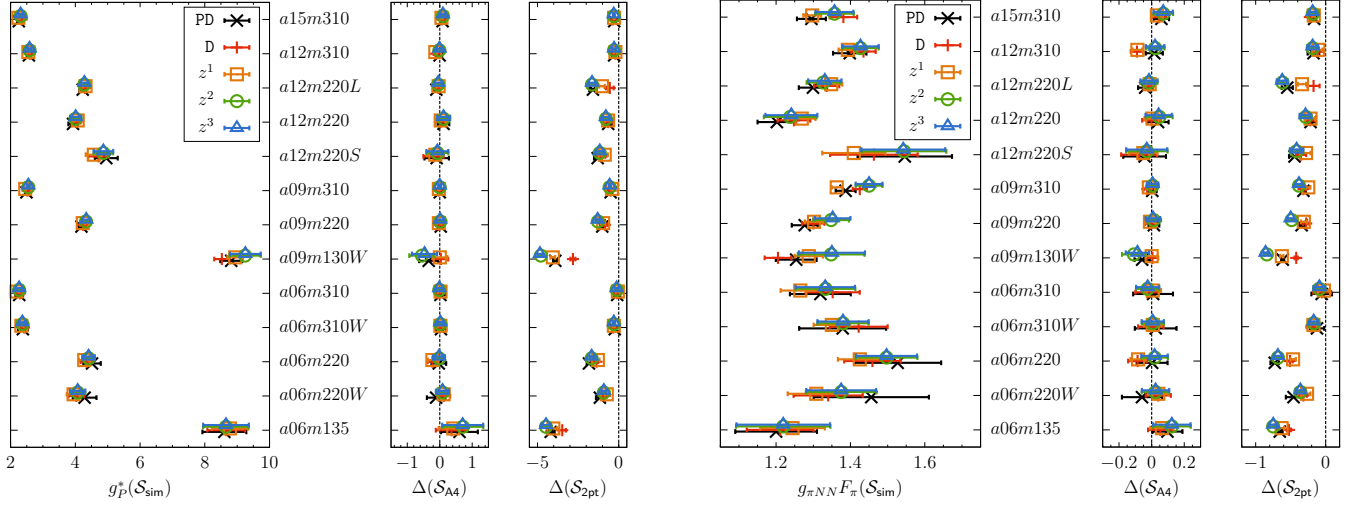


FIG. 14. (Left) Results for the bare g_P^* from the strategy \mathcal{S}_{sim} and the differences $\Delta(X) = g_P^*(X) - g_P^*(\mathcal{S}_{\text{sim}})$. To facilitate visualization of the spread, the errors plotted for $\Delta(X)$ are those in $g_P^*(X)$. The fits used to parameterize the Q^2 behavior are labelled “PD” defined in Eq. (40); “D” for the dipole fit, and z^k for various truncations of the z -expansion. (Right) Results for bare values of $g_{\pi NN} F_\pi$ obtained with the strategy \mathcal{S}_{sim} and the differences $\Delta(X) = g_{\pi NN} F_\pi(X) - g_{\pi NN} F_\pi(\mathcal{S}_{\text{sim}})$.

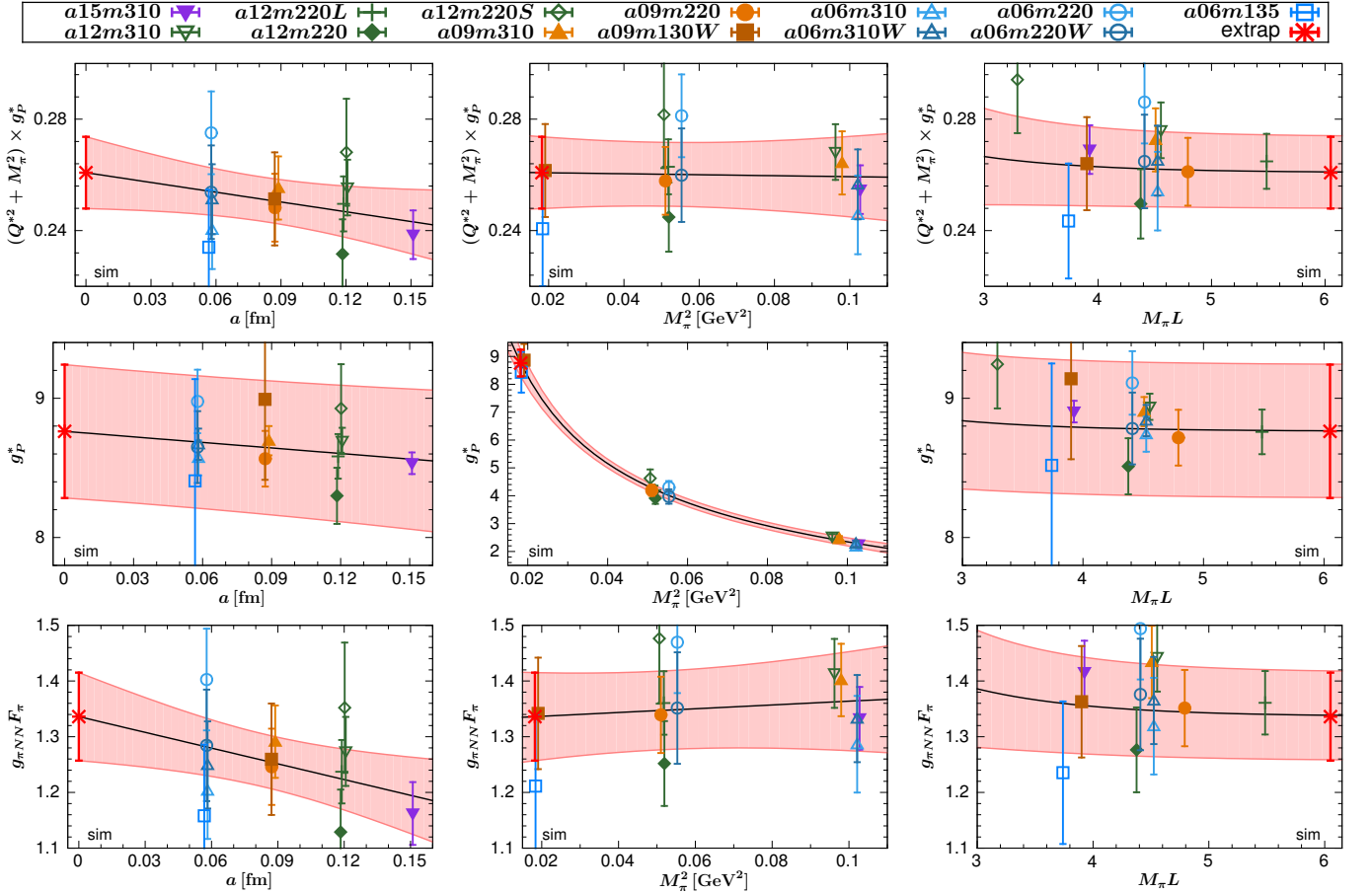


FIG. 15. The chiral-continuum-finite-volume extrapolation of the $(Q^2 + M_\pi^2) \times g_P^*$ (top row), g_P^* (middle row), and $g_{\pi NN} F_\pi$ (bottom row) data using the 13-point fit. In each case the data were obtained using the z^2 parameterization of $\bar{F}_P(Q^2 \neq 0)$ with strategy \mathcal{S}_{sim} . The black solid line with the pink error band represents a hyperplane obtained by taking the physical limit of all CCFV fit variables except the one shown on the x -axis. The plotted data points have been shifted by using the fit coefficients, while the errors are unchanged.

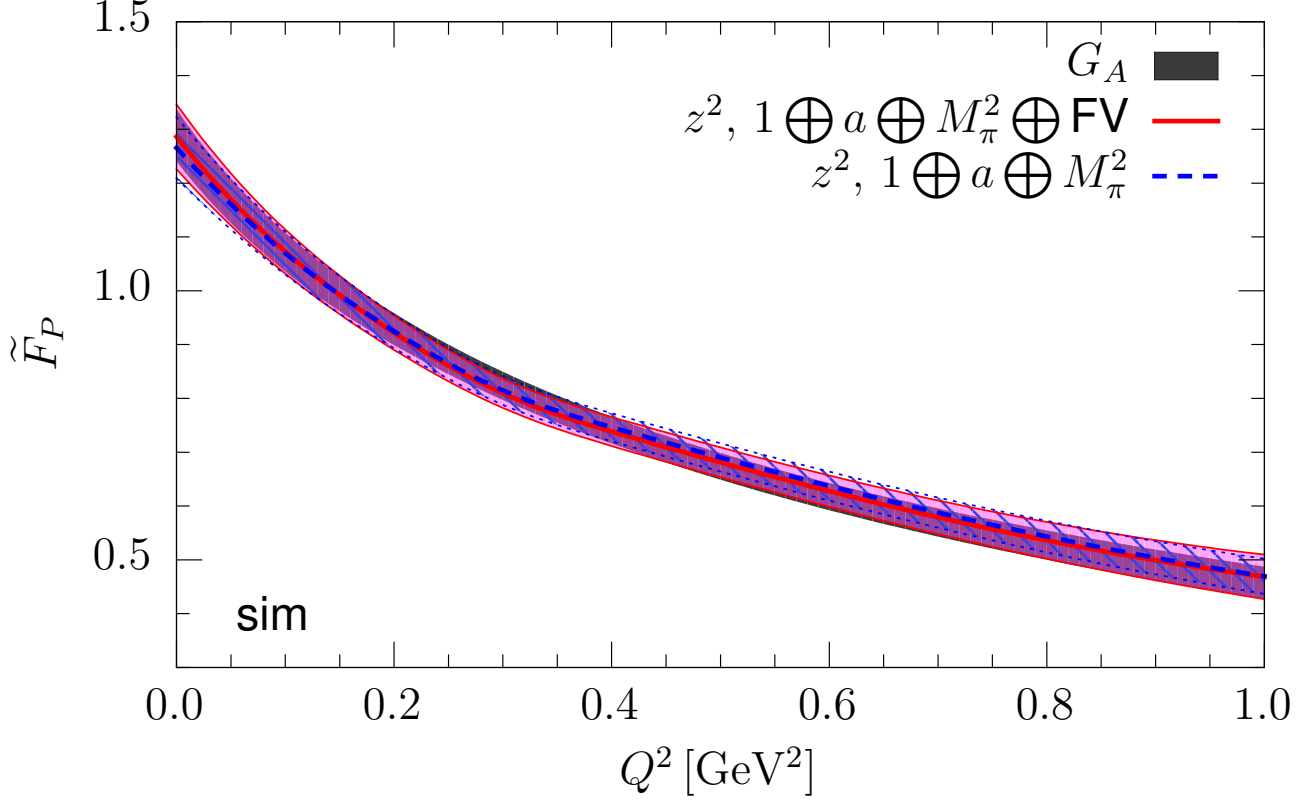


FIG. 16. The close overlap in the physical point results for $\tilde{F}_P(Q^2)$, defined in Eq. (39), with $G_A(Q^2)$ (black lines) reproduced from Fig. 12. Both were obtained using the three step process described in the text and the \mathcal{S}_{sim} strategy data. The full CCFV fits to the \tilde{F}_P data are shown with the solid red line and pink error band and the fit without the FV term with dashed blue line and hatched error band. These error bands show only the central analysis uncertainty.

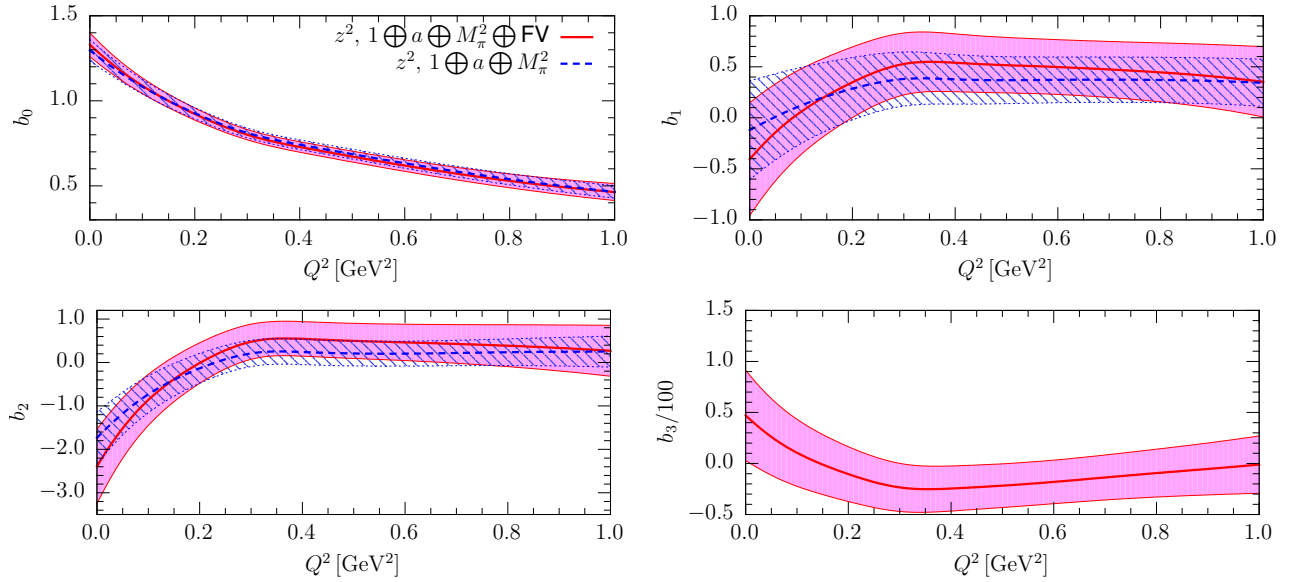


FIG. 17. The four CCFV fit coefficients b_i , $i = 0, 1, 2, 3$, defined in Eq. (29) for extrapolating $\tilde{F}_P(Q^2)$. The rest is the same as in Fig. 16.

V. NUCLEON CHARGES FROM FORWARD MATRIX ELEMENTS

The spectral decomposition of the forward, $\mathbf{q} = 0$, three-point function truncated at three states, $|i\rangle$ with $i = 0, 1, 2$, can be written as

$$\begin{aligned}
 C_{\Gamma}^{3\text{pt}}(t; \tau) &= \sum_{i,j=0} |A_j| |A_i| \langle j | \mathcal{O}_{\Gamma} | i \rangle e^{-M_i t - M_j(\tau-t)} \\
 &= |A_0|^2 g_{\Gamma} e^{-M_0 \tau} \times \left[1 + r_1^2 b_{11} e^{-\Delta M_1 \tau} \right. \\
 &\quad + r_2^2 b_{22} e^{-(\Delta M_1 + \Delta M_2) \tau} \\
 &\quad + 2r_1 b_{01} e^{-\Delta M_1 \tau/2} \cosh(\Delta M_1 t_s) \\
 &\quad + 2r_2 b_{02} e^{-(\Delta M_1 + \Delta M_2) \tau/2} \cosh\{(\Delta M_1 + \Delta M_2) t_s\} \\
 &\quad \left. + 2r_1 r_2 b_{12} e^{-(2\Delta M_1 + \Delta M_2) \tau/2} \cosh(\Delta M_2 t_s) \right] \\
 &\quad + \dots, \tag{46}
 \end{aligned}$$

where $t_s \equiv t - \tau/2$, $\langle 0 | \mathcal{O}_{\Gamma} | 0 \rangle$ is the bare charge g_{Γ} , the transition matrix elements are $b_{ij} \equiv \langle i | \mathcal{O}_{\Gamma} | j \rangle / \langle 0 | \mathcal{O}_{\Gamma} | 0 \rangle$, the ratios of amplitudes are $r_i = |A_i|/|A_0|$, and the successive mass gaps are $\Delta M_i \equiv M_i - M_{i-1}$. The prefactors in terms involving the excited states are combinations such as $r_2^2 b_{22}$. These are to be regarded as simply parameters in the fits and are not used subsequently. Thus the excited-state amplitudes R_i , by themselves, are not needed.

To remove the contributions from excited states, we made three kinds of fits based on Eq. (46):

- **3***: This is a 3-state fit with b_{22} set to zero. The four parameters A_0 , M_0 , M_1 , M_2 are taken from four-state fits to the two-point function, leaving only $\langle 0 | \mathcal{O}_{\Gamma} | 0 \rangle$, and products such as $r_1^2 b_{11}$ as free parameters. This strategy (along with its two-state version) was used to get the results presented in Ref. [13], which are reproduced in Eq. 47.
- **3-RD**: This is a 3-state fit with b_{01} , b_{11} and b_{22} set to zero, otherwise the fits become unstable. The three parameters A_0 , M_0 , M_1 are again taken from four-state fits to the two-point function. The value of the second mass gap, ΔM_2 , is left as a free parameter in the fit. The sign of ΔM_2 for a given charge determines whether $|1\rangle$ lies above or below $|2\rangle$ as shown pictorially in Fig. 18.
- **3-RD- $N\pi$** : In this fit, M_1 is fixed to the noninteracting energy of $(N(\mathbf{n})\pi(-\mathbf{n}))$ state with $\mathbf{n} = (1, 0, 0)$. For the value of M_2 , we use a Bayesian prior with a narrow width centered about the first excited state mass determined from the two-point correlator as given in Table XXX in Appendix F.

We also tried two-state fits with ΔM_1 left as a free parameter. For the axial charge, we found large fluctuations in ΔM_1 between the jackknife samples leading to unreliable values. So we do not present these estimates.

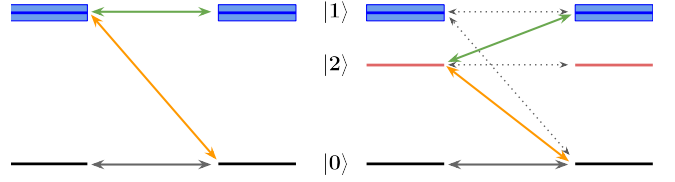


FIG. 18. A pictorial representation of the standard 2-state fit (left) and the 3-RD fit (right). In the 3-RD fit, the M_0 and M_1 are taken from the nucleon two-point correlator fit but ΔM_2 is determined from the fit to the three-point correlator. Negative values for ΔM_2 in Table XXXII indicate that $|2\rangle$ lies below $|1\rangle$. Both fits include only two transitions, $|0\rangle \rightarrow |1\rangle$ (yellow) and $|1\rangle \rightarrow |1\rangle$ (green) in the 2-state fit and $|0\rangle \rightarrow |2\rangle$ (yellow) and $|1\rangle \rightarrow |2\rangle$ (green) in the 3-RD fit. The transitions turned off with respect to the full 3-state ansatz given in Eq. (46) are represented by dashed lines.

Results for unrenormalized isovector nucleon charges, g_A , g_T , and g_S , using the 3*, 3-RD, and the 3-RD- $N\pi$ fits are given in Table XXXI, and the other parameters of the 3-RD fits are given in Table XXXII in Appendix F.

The final renormalized charges are presented in the $\overline{\text{MS}}$ scheme at 2 GeV. We carry out the renormalization using the RI-sMOM intermediate scheme as described in Ref. [13]. To understand systematics, we use three methods: (i) $g_X = Z_X g_X^{(\text{bare})}$, where $X = A, T, S$; and (ii) $g_X = Z_X/Z_V \times g_X^{(\text{bare})}/g_V^{(\text{bare})}$ and use the relation $Z_A g_V = 1$. For the final values, we use the average of these two within the jackknife process, and call it method three. The renormalization factors Z_X and Z_X/Z_V used in this study are given in Table V in Ref. [13].

We use the same leading order CCFV ansatz, given in Eq. (29), for extrapolating results from all three strategies: 3*, 3-RD, and 3-RD- $N\pi$.

Results from the 3* (or 2-state for g_S) analysis, have already been published in Ref. [13], and reproduced here to facilitate comparison.¹ These are:

$$\begin{aligned}
 g_A &= 1.218(25)_{\text{stat}}(30)_{\text{sys}} & (3^*\text{-state, [13]}) \\
 g_T &= 0.989(32)_{\text{stat}}(10)_{\text{sys}} & (3^*\text{-state, [13]}) \\
 g_S &= 1.022(80)_{\text{stat}}(60)_{\text{sys}} & (2\text{-state, [13]}).
 \end{aligned} \tag{47}$$

We now focus on the 3-RD analysis and make the following cuts on the points chosen for the CCFV extrapolation:

- “13-point” CCFV fit uses all thirteen points.
- “11-point-narrow” CCFV fit: This fit excludes the $a06m310W$ and $a06m220W$ points obtained with larger smearing radius for sources used to calculate quark propagators [13]. Larger smearing radius reduces the ESC at smaller values of τ but

¹ The statistics in the $a06m135$ and $a12m310$ ensembles have been increased, however, the changes in the estimates are insignificant, so we continue to quote the results from Ref. [13].

gives larger statistical errors at the values of τ used in our excited-state fits to get the $\tau \rightarrow \infty$ values as discussed in Ref. [12]. Also, we expect significant correlations between the two pairs, ($a06m310$, $a06m310W$) and ($a06m220$, $a06m220W$), since they use the same gauge configurations. Comparing the two sets, the results for the three charges agree except for g_S between $a06m220$ and $a06m220W$. This difference can be explained as due to statistical errors, which are large for g_S , especially in the $a06m220W$ data. Consequently, the “11-point-narrow” CCFV fit is used to get the central value for g_S , which is shown in Fig. 19.

- “10-point-narrow” CCFV fit excludes $a15m310$, $a06m310W$ and $a06m220W$ points. Since the variation with the lattice spacing is the dominant systematic, removing the $a15m310$ point (coarsest lattice with $a \sim 0.15$ fm) provides a handle on higher order, $\mathcal{O}(a^2)$, corrections neglected in Eq. (29).

Results from these three CCFV fits, different truncations of the CCFV ansatz, and the three renormalization methods are given in Tables XXXIII, XXXIV, and XXXV in Appendix F and used to assess the various systematics.

The central values are taken from the “13-point fit” for g_A and g_T and the “11-pt-narrow fit” for g_S with the 3-RD data renormalized using the third (average of the first two) method. Note that we find a systematic shift of ≈ 0.03 , 0.02 and 0.03 between the first two renormalization methods for the three charges, g_A , g_T and g_S , respectively.

These CCFV fits are shown in Fig. 19. Each panel in a given row shows the fit result versus one of the three variables with the other two set to their physical point values. In the left two panels, we show two fits: (i) using the full ansatz given in Eq. (29) (pink band), and (ii) assuming there is dependence only on the x-axis variable (grey band). For example, in the left panels the grey band corresponds to a fit with $b_2^{g_x} = b_3^{g_x} = 0$. The data show that the discretization errors are the dominant systematic, i.e., there is an almost complete overlap of the two fits (pink and grey bands) for g_A and a significant overlap for g_S and g_T . The variation with a over the range $0 < a \leq 0.15$ fm is about 10%, 5% and 30% for g_A , g_T , and g_S , respectively. The large variation with a in g_S is similar to that found in the clover-on-clover calculation [7].

The final results of the 3-RD analysis are:

$$\begin{aligned} g_A &= 1.294(42)_{\text{stat}}(18)_{\text{CCFV}}(16)_Z & (3\text{-RD}) \\ g_T &= 0.991(21)_{\text{stat}}(04)_{\text{CCFV}}(09)_Z & (3\text{-RD}) \\ g_S &= 1.085(50)_{\text{stat}}(102)_{\text{CCFV}}(13)_Z & (3\text{-RD}). \end{aligned} \quad (48)$$

The first error quoted (labeled stat) is the total uncertainty from the central analysis. The second error is an estimate of the uncertainty in the CCFV extrapolation. For g_A and g_T , this is taken to be the average of the differences |11-pt-narrow - 13-pt| and |10-pt-narrow - 13-pt|.

For g_S , it is the difference |10-pt-narrow - 11-pt-narrow|. The third error is half the difference in estimates between the first two renormalization methods.

The g_A from the 3-RD fit is in good agreement with the result obtained from the extrapolation of the axial form factor $G_A(Q^2)$ to $Q^2 = 0$ that is given in Eq. (30). It is also consistent with experimental value $g_A = 1.2766(20)$ but has much larger errors. The difference from the 3^* (PNDME18) value reproduced in Eq. (47) is due to different excited state energies used in the fits to the spectral decomposition. The data in Table XXXII show that the fit parameter M_2 when left free satisfies $M_\pi \lesssim M_2 - M_0 \lesssim 3M_\pi$ for all but the $a \approx 0.12$ fm lattices. In [9], we showed evidence that the $N(\mathbf{p}_1) + \pi(-\mathbf{p}_1)$ with $\mathbf{p}_1 = (1, 0, 0)2\pi/La$ state makes a significant contribution on the zero momentum side of the operator insertion in the calculation of the form factors, and the non-interacting energy of this state is $M_{N\pi} - M_0 \approx 2M_\pi$. In short, the M_2 output by the 3-RD fit has a mass lower than M_1 obtained from the two-point correlator and broadly consistent with the hypothesis that the $N\pi$ states contribute. We again caution the reader that these excited state masses should only be regarded as effective fit parameters that encapsulate the effect of the full tower of $N(\mathbf{p}) + \pi(-\mathbf{p})$ states with momenta $\mathbf{p} = (2\pi/L)\mathbf{n}$ as well as other multihadron and radial excitations that can contribute.

For g_S and g_T , the 3-RD fit reduces to a 2-state fit if $\Delta M_2 (= M_2 - M_1) = 0$, i.e., $M_2 \simeq M_1$. This is the case for many of the ensembles as shown in Table XXXII. Results given in Eq. (48) are consistent with those in Eq. (47) indicating that sensitivity to excited state energies is small.

Based on the 3-RD fits, which indicate that the data for g_A prefer a low-mass excited state with $\Delta M \approx 2M_\pi$, the 3-RD- $N\pi$ fit defined above, with the mass gaps summarized in Table XXX, were performed. Charges from this fit are compared with 3-RD and 3^* -state fits (or 2-state fit for the g_S) in Table XXXI for the thirteen ensembles. The p -value for many of the 3-RD- $N\pi$ fits are low. To stabilize the 3-RD- $N\pi$ fits, we increased the width of the priors for M_2 , however, this still did not lead to stable fits for several ensembles.

A comparison of $g_{A,S,T}$ obtained in Eq. (48) with recent results obtained by other collaborations is made in Table VI. The FLAG has reviewed results prior to 2021 [5, 6]. Overall, results for g_A and g_T are consistent within five percent and for g_S at ten percent, and the precision will continue to improve steadily.

Our conclusion is that, with current statistics, fits for the axial charge are more stable with input of M_0 and M_1 from the 4-state fit to the 2-point function and letting the 3-point function determine M_2 (corresponding roughly to the $N\pi$ state), i.e., the 3-RD fit. In future works with higher statistics, we intend to continue to investigate whether results from 3-RD and 3-RD- $N\pi$ fits come together as one would expect.

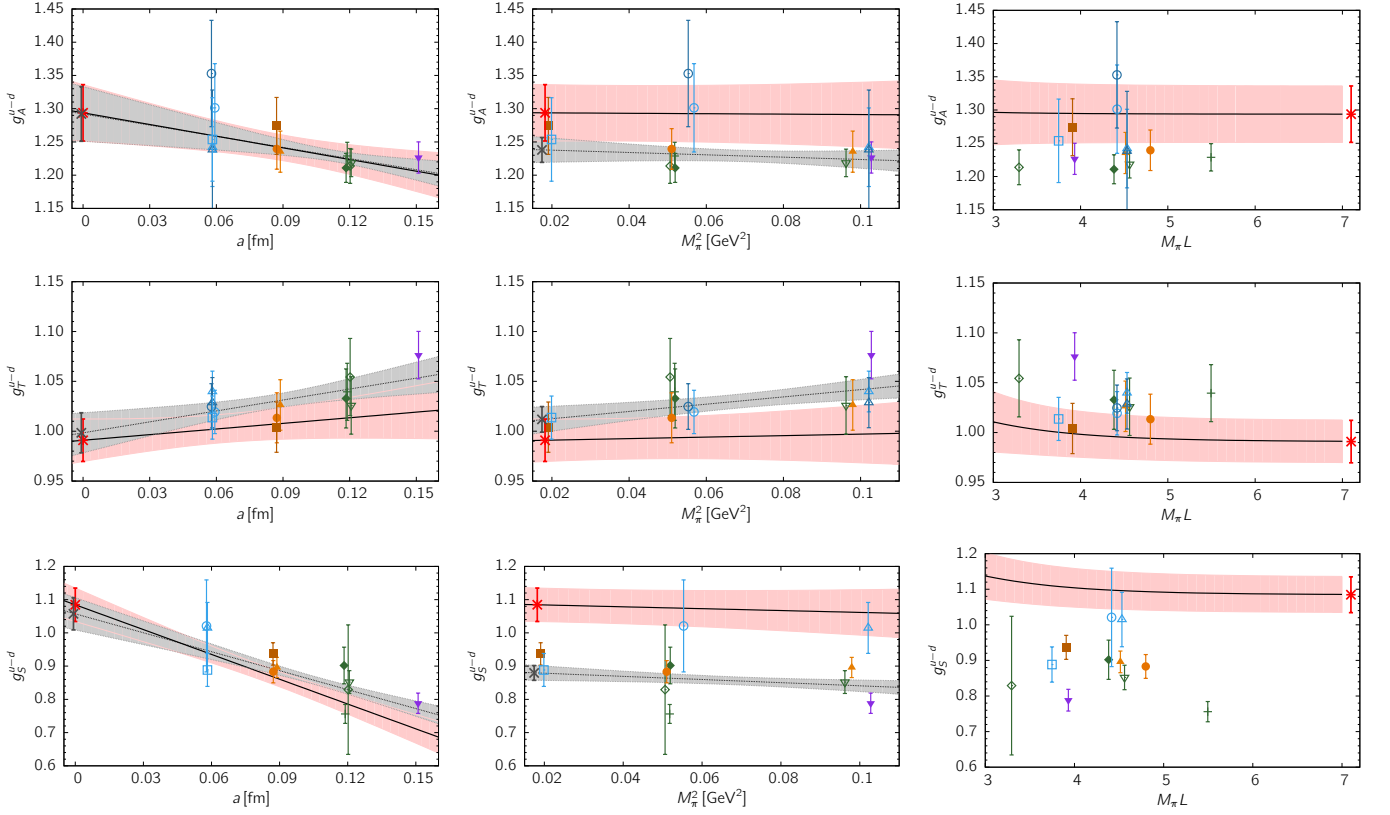


FIG. 19. The simultaneous chiral-continuum-finite-volume (CCFV) fit to the axial g_A (top, 13-point), tensor g_T (middle, 13-point), and scalar g_S (bottom, 11-point-narrow) charges. The data are extracted using the 3-RD fit described in the text and are the average over the two renormalization methods $Z_X \times g_X^{(\text{bare})}$ and $Z_X/Z_V \times g_X^{(\text{bare})}/g_V^{(\text{bare})}$ where the g_V is the vector charge. In each panel, the pink bend with black solid line represents the full CCFV fit. In the left (middle) panels, the grey band shows the fit to the date keeping only the a (M_π^2) dependent term in Eq. (29). The value at the physical point is marked by the red star. In each panel, the data have not been shifted with respect to the other two fit variables.

Collaboration	g_A	g_S	g_T	$\langle r_A^2 \rangle \text{ fm}^2$	g_P^*	$g_{\pi NN}$
PNDME 23	1.292(53)(24)	1.085(50)(103)	0.991(21)(10)	0.439(56)(34)	9.03(47)(42)	14.14(81)(85)
RQCD 19/23	1.284 $^{28}_{27}$	1.11 $^{14}_{16}$	0.984 $^{19}_{29}$	0.449(88)	8.68(45)	12.93(80)
ETMC 20	1.283(22)	1.35(17)	0.936(25)	0.343(42)(16)		
NME 21	1.32(6)(5)	1.06(9)(7)	0.97(3)(2)	0.428(53)(30)	7.9(7)(9)	12.4.(1.2)
Mainz 22	1.225(39)(25)	1.13(11)($\bar{7}$)	0.965(38)($^{13}_{41}$)	0.370(63)(16)		
PACS 22	1.288(14)(9)	0.927(83)(22)	1.036(6)(20)			

TABLE VI. Comparison of $g_{A,S,T}$, $\langle r_A^2 \rangle$, g_P^* and $g_{\pi NN}$ from recent calculations labeled as: PNDME 23 is this work, RQCD [20] (here we list values obtained with the $!z^{4+3}$ fit, and take $g_{A,S,T}$ from their recent work [21]), ETMC [22], NME [7], Mainz [23], and PACS [24]. All results for $g_{A,S,T}$ are in the $\overline{\text{MS}}$ scheme at scale 2 GeV. For completeness, we also give results for $g_{S,T}$ from the Mainz collaboration [25] and from the ETMC collaboration [26]. These and earlier results are reviewed by the FLAG [5, 6].

VI. CONCLUSIONS AND COMPARISON WITH PREVIOUS CALCULATIONS

We have presented results for the axial, $G_A(Q^2)$, the induced pseudoscalar, $\tilde{G}_P(Q^2)$, and the pseudoscalar, $G_P(Q^2)$, form factors of nucleons using thirteen ensembles of 2+1+1-flavors of HISQ ensembles generated by the MILC collaboration [8]. A large part of the focus of this work is on understanding the nature of the excited states that contribute significantly to the relevant nuclear correlation functions and removing their contributions. The analysis presented here strengthens the case for including multihadron excited states, such as $N\pi$, made in Ref. [9]. Our data driven analysis strategy, labeled \mathcal{S}_{sim} , identifies contributions from $N\pi$ state in the extraction of the GSME. The three form factors obtained including $N\pi$ state satisfy the PCAC relation to within 10% as opposed to a $\sim 50\%$ deviation without them. For the final results, we therefore choose the data obtained with the \mathcal{S}_{sim} strategy for removing ESC, parameterize the Q^2 behavior using the model-independent z^2 fit; and extrapolate the data to the physical point using the leading order terms in a simultaneous chiral-continuum-finite-volume fit ansatz given in Eq. (29). For errors, we quote two estimates: the first labeled “stat” is the total error obtained from the analysis used to produce the central value, and the second, labeled “sys”, is a combined systematic error discussed in the appropriate sections.

Our final results are:

- The axial charge is $g_A = 1.292(53)_{\text{stat}}(24)_{\text{sys}}$. This is the unweighted average of the value from the extrapolation of $G_A(Q^2)$ to $Q^2 = 0$ (Eqs. (36)) and from the forward matrix element (Eq. (48)). The “stat” and “sys” errors quoted are the larger of those from the two determinations. This result is consistent with the experimental value but has much larger errors.
- The scalar charge $g_S = 1.085(50)_{\text{stat}}(103)_{\text{sys}}$ and the tensor $g_T = 0.991(21)_{\text{stat}}(10)_{\text{sys}}$ are taken from Eq. (48).
- The extraction of the axial charge radius squared is discussed in Sec. IIIB, and the result taken from Eq. (36) is $\langle r_A^2 \rangle = 0.439(56)_{\text{stat}}(34)_{\text{sys}} \text{ fm}^2$.
- The extraction of the induced pseudoscalar charge is discussed in Sec. IV B 1 and the result from Eq. (42) is $g_P^* = 9.03(47)_{\text{stat}}(42)_{\text{sys}}$.
- The pion-nucleon coupling is discussed in Sec. IV B 2 and the result taken from Eq. (43) is $g_{\pi NN} = 14.14(81)_{\text{stat}}(85)_{\text{sys}}$.
- Our procedure for obtaining the axial form factor, $G_A(Q^2)$, in the continuum limit is discussed in Sec. IIIB. The final parameterization is given in Eq. (32), the covariance matrix of the fit in Eq. (33), and the corresponding values of $g_A =$

$1.281(53)$ and $\langle r_A^2 \rangle = 0.498(56) \text{ fm}^2$ in Eq. (34). The final values from the analysis of G_A are given in Eq. (36).

A comparison of lattice results from various collaborations for all the above quantities was presented recently in Ref. [7]. The charges $g_{A,S,T}$ have also been reviewed by FLAG [5–7]. Since then, new results have been presented in Refs. [23, 24, 27]. The full list of relevant publications that have included $N\pi$ states in the analysis of ESC and checked whether form-factors satisfy the PCAC relation are [7, 9, 20, 22–24]. We first summarize the results and important points made in each of these calculations, and then show a comparison of $G_A(Q^2)$ obtained by the various collaborations in Fig. 20. Results for the charges are compared in Table VI.

The observation that the form factors extracted using the spectrum from the nucleon 2-point function fail to satisfy the PCAC relation Eq. (17) was made in Ref. [14]. The possible cause, enhanced contributions of multihadron ($N\pi$) excited states in the axial channel was proposed by Bär [11] using a χPT analysis. This was confirmed using the data for the three-point function with the insertion of the A_4 current in Ref. [9]. This data-driven analysis, including only the lowest $N\pi$ excited state, found that the ESC to the $\tilde{G}_P(Q^2)$ and $G_P(Q^2)$ form factors were about 35%, while that in $G_A(Q^2)$ could be $O(5\%)$ as the latter is affected only at one-loop in χPT . This level of contamination in $G_A(Q^2)$ is consistent with what is observed in the axial charge g_A extracted from the forward matrix element. Below, we present a brief comparison of our results with other lattice calculations published in [7, 20, 22–24].

The RQCD collaboration [20] has extracted $G_A(Q^2)$ from a two-state fit to thirty-six 2+1-flavor Wilson-clover ensembles generated by the coordinated lattice simulations (CLS) collaboration. The $\tilde{G}_P(Q^2)$ and $G_P(Q^2)$ are, on the other hand, extracted using a 3-state fit in which the first excited state energies are fixed to be the non-interacting energies of the lowest $N\pi$ state and the second excited state energies are taken to be the first excited state (values higher than $N(1440)$) given by fits to the 2-point nucleon correlators. While their form factors satisfy the PCAC relation, they are equally well fit by the dipole ansatz and z^{4+3} (i.e., z^3 with sum rule constraints). The axial charge $g_A = 1.302(86)$ from z -expansion (fit labeled $!z^{4+3}$) is larger than $g_A = 1.229(30)$ from dipole (labeled $!2P$) with the latter agreeing with that from the forward matrix element. The corresponding difference in $\langle r_A^2 \rangle$ is $0.449(88)$ versus $0.272(33) \text{ fm}^2$. Results for g_P^* ($8.68(45)$ versus $8.30(24)$) and for $g_{\pi NN}$ ($12.93(80)$ versus $14.78(1.81)$) are consistent. They have recently [21] updated their results for $g_{A,S,T}$ based on the analysis of 47 ensembles. We quote these values in Table VI.

The preferred estimates from the ETM collaboration [22] are from a single 2+1+1-flavor physical mass $64^3 \times 128$ ensemble at $a \approx 0.8 \text{ fm}$. For the analysis of $G_A(Q^2)$, they take excited-state energies from the 2-point

function and find $\langle r_A^2 \rangle = 0.343(42)(16) \text{ fm}^2$. Their result for $g_A = 1.283(22)$ is obtained from the forward matrix element extracted without including possible contamination from $N\pi$ states. When results from the direct calculations of $\tilde{G}_P(Q^2)$ and $G_P(Q^2)$ are used, the three form factors show large deviations from the PCAC relation which they attribute partially to large discretization errors in their twisted mass formulation [28]. Consequently, they quote final estimates of $\tilde{G}_P(Q^2)$ derived from $G_A(Q^2)$ using the pion-pole dominance hypothesis, i.e., the quoted \tilde{G}_P is not independently determined.

The NME collaboration [7] analyzed seven ensembles generated with 2+1-flavors of Wilson-clover fermions. They make a simultaneous fit to all five correlation functions with insertion of the axial, A_μ , and pseudoscalar, P , currents, i.e., same as the \mathcal{S}_{sim} strategy used in this work. The A_4 correlator provides the dominant contribution to fixing the excited-state energies which turn out to be close to the lowest $N\pi$ states as also discussed in this paper and in Ref. [9]. The resulting form factors satisfy the PCAC relation to within ten percent. Observing only a small dependence of $G_A(Q^2)$ on a and M_π , they provide a continuum parameterization of $G_A(Q^2)$ neglecting these effects, and thus underestimate the uncertainty. This $G_A(Q^2)$ is reproduced in Fig. 20. The value of the axial charge without including $N\pi$ state is $g_A = 1.242(46)(42)$ and including them gives $1.32(6)(5)$. Their other results are $\langle r_A^2 \rangle = 0.428(53)(30) \text{ fm}^2$, $g_P^* = 7.9(7)(9)$ and $g_{\pi NN} = 12.4(1.2)$.

The Mainz Collaboration [23] analyze fourteen 2+1-flavor Wilson-clover ensembles also generated by the coordinated lattice simulations (CLS) collaboration. They obtain a parameterization of $G_A(Q^2)$ in the continuum from a single combined fit—summation method for dealing with ESC and the z^2 fit for the Q^2 behavior. This result is shown in Fig. 20 and from it they get $g_A = 1.225(39)(25)$ and $\langle r_A^2 \rangle = 0.370(63)(16) \text{ fm}^2$.

The PACS collaboration [24] has analyzed one ensemble with a large volume (128^4) at $a = 0.085 \text{ fm}$ and get $g_A = 1.288(14)(9)$. Remarkably, they find that an exponential smearing of sources for the generation of quark propagators, in contrast to Gaussian smearing used by all other calculations, leads to essentially no excited-state effects. The limitation of this calculation is only 20 configurations, each separated by 10 molecular dynamics trajectories, were analyzed. Most likely, this total of 200 trajectories represents less than one unit of autocorrelation time. Consequently, the errors are likely underestimated even on this single large-volume ensemble. No parameterization of $G_A(Q^2)$ has been presented.

Phenomenologically, the most important quantity is $G_A(Q^2)$, and we show a comparison of results from various lattice collaborations in Fig. 20 along with the extraction from the ν -deuterium bubble chamber scattering experiments [18]. In all cases, except ETM, the data are extrapolated to the physical point and then fit using a truncated z -expansion. The bands in Fig. 20 overlap indicating that the lattice results are consistent within one

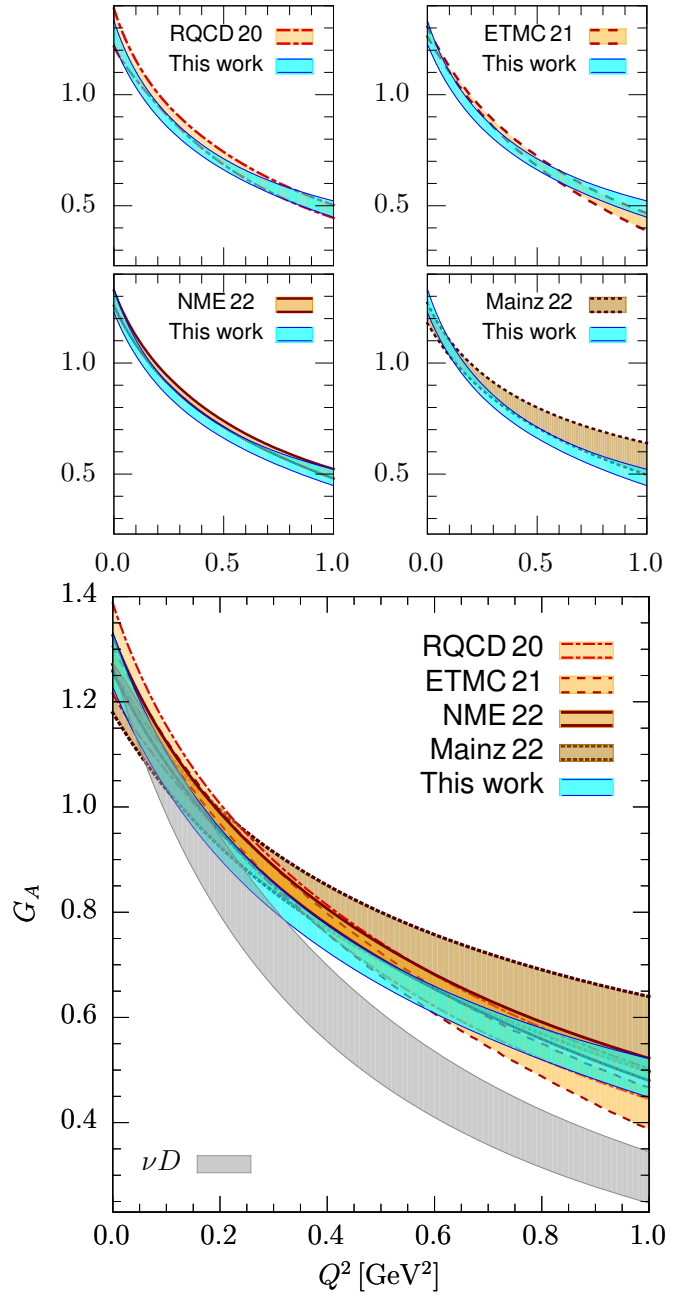


FIG. 20. A comparison of the isovector axial form factor $G_A(Q^2)$ at the physical point obtained using a z -expansion fit by the RQCD [20] (light faun band), ETMC [22] (light tan band), NME [7] (tan band), Mainz [23] (brown band) collaborations and this work (turquoise band). The G_A extracted using the ν -deuterium bubble chamber scattering experiments data [18] is shown by the grey band and labeled νD in the lower panel.

sigma and the envelope of the bands suggests a roughly 10% uncertainty throughout the range $0 < Q^2 < 1.0 \text{ GeV}^2$. The other significant observation is that the lattice results fall slower than the phenomenological extraction (the νN band) for $Q^2 \gtrsim 0.3 \text{ GeV}^2$.

When comparing between these current lattice data, it

is important to note that the analyses by the various collaborations handle various systematics differently. These systematic effects will become clearer and the analysis more robust as the precision of the data increases. In this regard, recent calculations including $N\pi$ states in a variational basis of interpolating operators [29] is a step forward and will, in time, provide further insight and improvements.

To reduce the roughly 10% spread in the lattice results compared in Fig. 20 requires much higher statistics data, which will be available over the next few years. It has become clear that $N\pi$ states need to be included in the analysis for the three form factors to satisfy the PCAC relation 17. The questions that remain for higher precision are how many multihadron states need to be kept in the spectral decomposition for a given precision and the size of their contributions.

VII. ACKNOWLEDGEMENT

We thank the MILC collaboration for providing the 2+1+1-flavor HISQ lattices used in this study. The calculations used the Chroma software suite [30]. This research used resources at (i) the National Energy Research Scientific Computing Center, a DOE Office of Science User Facility supported by the Office of Science of the U.S. Department of Energy under Contract No. DE-AC02-05CH11231; (ii) the Oak Ridge Leadership Computing Facility, which is a DOE Office of Science User Facility supported under Contract DE-AC05-00OR22725, and was awarded through the ALCC program project LGT107 and INCITE award HEP133; (iii) the USQCD collaboration, which is funded by the Office of Science of the U.S. Department of Energy; and (iv) Institutional Computing at Los Alamos National Laboratory. T. Bhattacharya and R. Gupta were partly supported by the U.S. Department of Energy, Office of Science, Office of High Energy Physics under Contract No. DE-AC52-06NA25396. T. Bhattacharya, R. Gupta, and B. Yoon were partly supported by the LANL LDRD program,

-
- [1] L. A. Ruso et al. (2022), 2203.09030.
 - [2] A. S. Kronfeld, D. G. Richards, W. Detmold, R. Gupta, H.-W. Lin, K.-F. Liu, A. S. Meyer, R. Sufian, and S. Syritsyn (USQCD), *Eur. Phys. J. A* **55**, 196 (2019), 1904.09931.
 - [3] A. S. Meyer, A. Walker-Loud, and C. Wilkinson (2022), 2201.01839.
 - [4] T. Cai et al. (MINERvA), *Nature* **614**, 48 (2023).
 - [5] Y. Aoki et al. (Flavour Lattice Averaging Group (FLAG)), *Eur. Phys. J. C* **82**, 869 (2022), 2111.09849.
 - [6] S. Aoki et al. (Flavour Lattice Averaging Group), *Eur. Phys. J. C* **80**, 113 (2020), 1902.08191.
 - [7] S. Park, R. Gupta, B. Yoon, S. Mondal, T. Bhattacharya, Y.-C. Jang, B. Joó, and F. Winter (Nucleon Matrix Elements (NME)), *Phys. Rev. D* **105**, 054505 (2022), 2103.05599.
 - [8] A. Bazavov et al., *Phys. Rev. D* **87**, 054505 (2013), 1212.4768.
 - [9] Y.-C. Jang, R. Gupta, B. Yoon, and T. Bhattacharya, *Phys. Rev. Lett.* **124**, 072002 (2020), 1905.06470.
 - [10] O. Bar, in *36th International Symposium on Lattice Field Theory (Lattice 2018) East Lansing, MI, United States, July 22-28, 2018* (2018), 1808.08738.
 - [11] O. Bar, *Phys. Rev. D* **99**, 054506 (2019), 1812.09191.
 - [12] B. Yoon et al., *Phys. Rev. D* **93**, 114506 (2016), 1602.07737.
 - [13] R. Gupta, Y.-C. Jang, B. Yoon, H.-W. Lin, V. Cirigliano, and T. Bhattacharya, *Phys. Rev. D* **98**, 034503 (2018), 1806.09006.
 - [14] R. Gupta, Y.-C. Jang, H.-W. Lin, B. Yoon, and T. Bhattacharya, *Phys. Rev. D* **96**, 114503 (2017), 1705.06834.
 - [15] V. Bernard, L. Elouadrhiri, and U.-G. Meissner, *J. Phys. G* **28**, R1 (2002), hep-ph/0107088.
 - [16] B. Bhattacharya, R. J. Hill, and G. Paz, *Phys. Rev. D* **84**, 073006 (2011), 1108.0423.
 - [17] Y.-C. Jang, R. Gupta, H.-W. Lin, B. Yoon, and T. Bhattacharya, *Phys. Rev. D* **101**, 014507 (2020), 1906.07217.
 - [18] A. S. Meyer, M. Betancourt, R. Gran, and R. J. Hill, *Phys. Rev. D* **93**, 113015 (2016), 1603.03048.
 - [19] G. S. Bali, B. Lang, B. U. Musch, and A. Schäfer, *Phys. Rev. D* **93**, 094515 (2016), 1602.05525.
 - [20] G. S. Bali, L. Barca, S. Collins, M. Gruber, M. Löffler, A. Schäfer, W. Söldner, P. Wein, S. Weishäupl, and T. Wurm (RQCD), *JHEP* **05**, 126 (2020), 1911.13150.
 - [21] G. S. Bali, S. Collins, S. Heybrock, M. Löffler, R. Rödl, W. Söldner, and S. Weishäupl (2023), 2305.04717.
 - [22] C. Alexandrou et al., *Phys. Rev. D* **103**, 034509 (2021), 2011.13342.
 - [23] D. Djukanovic, G. von Hippel, J. Koponen, H. B. Meyer, K. Ottnad, T. Schulz, and H. Wittig, *Phys. Rev. D* **106**, 074503 (2022), 2207.03440.
 - [24] R. Tsuji, N. Tsukamoto, Y. Aoki, K.-I. Ishikawa, Y. Kuramashi, S. Sasaki, E. Shintani, and T. Yamazaki (PACS), *Phys. Rev. D* **106**, 094505 (2022), 2207.11914.
 - [25] T. Harris, G. von Hippel, P. Junnarkar, H. B. Meyer, K. Ottnad, J. Wilhelm, H. Wittig, and L. Wrang, *Phys. Rev. D* **100**, 034513 (2019), 1905.01291.
 - [26] C. Alexandrou, S. Bacchio, M. Constantinou, J. Finkenrath, K. Hadjiyiannakou, K. Jansen, G. Koutsou, and A. Vaquero Aviles-Casco, *Phys. Rev. D* **102**, 054517 (2020), 1909.00485.
 - [27] C. Alexandrou, S. Bacchio, M. Constantinou, K. Hadjiyiannakou, K. Jansen, and G. Koutsou, *Phys. Rev. D* **104**, 074503 (2021), 2106.13468.
 - [28] C. Alexandrou, *SciPost Phys. Proc.* **6**, 006 (2022).
 - [29] L. Barca, G. Bali, and S. Collins, *Phys. Rev. D* **107**, L051505 (2023), 2211.12278.

- [30] R. G. Edwards and B. Joo (SciDAC Collaboration, LHPC Collaboration, UKQCD Collaboration), Nucl.Phys.Proc.Suppl. **140**, 832 (2005), hep-lat/0409003.

Appendix A: Determining the nucleon spectrum from $C^{2\text{pt}}(t)$

To extract the nucleon spectrum, we make two kinds of fits to the spectral decomposition of $C^{2\text{pt}}(t)$. The first is a frequentist (labeled F) multiexponential fit, i.e., without any priors. It is a three-state fit for $a \approx 0.06, 0.09$ fm ensembles, and two-state for $a \approx 0.12, 0.15$ fm ensembles. These frequentist results ($n_s = 2$ or 3) are compared against empirical Bayesian four-state fits ($n_s = 4$) in Table VII, and their difference is shown in Fig. 21 (bottom panel). We observe that

- The ground state masses from the F - and B -fits given in Table VII are consistent within one combined σ . There is, however, a small but systematic shift with $M_0^{(4)} < M_0^{(3)}$, indicating near convergence. The deviations are ≈ 10 MeV on all except $a12m220S$ and $a06m310$ ensembles, where they are $20 - 30$ MeV. Overall, the B -fit values are smaller.
- Most of the thirteen calculations satisfy the relativistic dispersion relation (speed of light c^2 consistent with unity) to within 1σ except for the B -fits for $a15m310$ and $a06m135$ ensembles.

The analysis of the first excited state mass from fits to the three-point correlations functions has been presented in Sec. II D. Here we study its extraction from the spectral decomposition of $C^{2\text{pt}}(t)$:

$$C^{2\text{pt}}(t) = a_0 e^{-E_0 t} \left\{ 1 + \sum_{k=1}^{\infty} b_k e^{-(E_k - E_0)t} \right\}, \quad (\text{A1})$$

where the coefficients a_0 and b_k are positive definite since the same interpolating operator is used at the source and the sink. Starting from the definition of the effective mass

$$m_{\text{eff}}(t) = \log \frac{C(t)}{C(t+1)} \quad (\text{A2})$$

one can derive, using the symmetric lattice derivative $df(t)/dt \rightarrow (f(t+1) - f(t-1))/2$, a series of effective masses $m_{\text{eff}}^{(n)}$

$$m_{\text{eff}}^{(0)} \equiv -\frac{d}{dt} \log C^{2\text{pt}}(t) \quad (\text{A3})$$

$$m_{\text{eff}}^{(n)} \equiv m_{\text{eff}}^{(n-1)} - \frac{d}{dt} \log(m_{\text{eff}}^{(n-1)} - E_{n-1}) \quad (\text{A4})$$

$$= E_n - \frac{d}{dt} \log \left\{ 1 + \sum_{k=n+1}^{\infty} \frac{b_k}{b_n} \frac{(E_k - E_0) \cdots (E_k - E_{n-1})}{(E_n - E_0) \cdots (E_n - E_{n-1})} e^{-(E_k - E_n)t} \right\}, \quad (n = 1, 2, \dots). \quad (\text{A5})$$

that should approach a plateau from above at a sufficiently large time t and give the energy levels E_n . To determine $m_{\text{eff}}^{(n)}(t)$, one could take the E_n from a multiexponential fit, with n limited by the statistical quality of the data. Note that no prior information of the overlap factors a_0 and b_k is required to calculate $m_{\text{eff}}^{(n)}(t)$.

These effective masses for the $a06m135$ ensemble are shown in Fig. 22 for the lowest two momenta and compared with when the E_i are taken from a four- (left panels) versus three-state (right panels) fits with values given by the black dashed lines with yellow error bands. The fit parameters and the first excited state masses, $M_1^{(4)}$ and $M_1^{(3)}$, are given in Table VIII. We note that

- The estimate of E_1 is slightly larger from the 3-state fits. Again, this is expected since the fits give “effective” E_i that partly incorporate the contributions of all the higher states neglected in the fits.
- The time t_1 when $m_{\text{eff}}^{(1)}(t)$ reaches the estimate E_1 is roughly constant, ≈ 0.7 fm.
- The signal in $m_{\text{eff}}^{(1)}(t)$ becomes noisy for $t \gtrsim t_1$, i.e.,

before confirmation of it having plateaued.

- Estimates of $M_1^{(4)}$ and $M_1^{(3)}$ for the two physical pion mass ensembles (see Table VIII and $M_1^{(4)} - M_1^{(3)}$ plotted in Fig. 21) are consistent with the $N(1710)$ excited state, or a combination of the $N(1440)$ and $N(1710)$ which overlap due to their widths, $\Gamma \approx 300$ and 100 MeV.
- Estimates of E_2 and $m_{\text{eff}}^{(2)}(t)$ from 3-state fits are not reliable.
- In the bottom right panel of Fig. 22, we input $E_1 = E_0 + 2M_\pi$ (solid black line) to study impact on $m_{\text{eff}}^{(n)}(t)$. Estimates of $m_{\text{eff}}^{(1)}(t)$ are not changed but $m_{\text{eff}}^{(2)}(t)$ shows a much more rapid fall. The signal is, however, poor and dies before any conclusion can be reached.

Overall, this analysis highlights the challenge of determining the excited state energies E_i from fits to $C^{2\text{pt}}(t)$ and making an association with physical states.

ID	n_s	$aM_0^{2\text{pt}}$	aM_0^{Disp}	c^2	$\hat{\chi}^2/\text{dof}$	p
<i>a15m310</i>	4	0.8302(21)	0.8304(21)	0.930(12)	1.37	0.195
<i>a15m310</i>	2	0.8315(20)	0.8319(19)	0.936(11)	0.96	0.474
<i>a12m310</i>	4	0.6660(27)	0.6662(26)	1.001(14)	0.62	0.777
<i>a12m310</i>	2	0.6715(13)	0.6716(13)	1.001(09)	0.73	0.685
<i>a12m220L</i>	4	0.6125(21)	0.6135(17)	0.995(15)	0.39	0.940
<i>a12m220L</i>	2	0.6187(10)	0.6187(10)	1.013(07)	0.67	0.741
<i>a12m220</i>	4	0.6080(31)	0.6086(30)	0.989(27)	0.33	0.967
<i>a12m220</i>	2	0.6151(14)	0.6152(14)	1.001(10)	0.91	0.515
<i>a12m220S</i>	4	0.6039(52)	0.6110(41)	0.970(29)	1.19	0.297
<i>a12m220S</i>	2	0.6194(26)	0.6204(24)	0.997(21)	0.69	0.718
<i>a09m310</i>	4	0.4951(14)	0.4959(13)	1.027(13)	1.72	0.078
<i>a09m310</i>	3	0.4952(15)	0.4961(13)	1.024(14)	0.96	0.473
<i>a09m220</i>	4	0.4495(20)	0.4513(15)	1.020(16)	0.36	0.955
<i>a09m220</i>	3	0.4514(16)	0.4528(13)	1.021(14)	0.53	0.857
<i>a09m130W</i>	4	0.4208(17)	0.4221(16)	0.978(31)	0.77	0.647
<i>a09m130W</i>	3	0.4213(18)	0.4225(17)	0.981(31)	1.12	0.342
<i>a06m310</i>	4	0.3248(30)	0.3257(28)	0.996(42)	0.97	0.422
<i>a06m310</i>	3	0.3305(21)	0.3319(19)	1.059(25)	0.80	0.524
<i>a06m310W</i>	4	0.3277(18)	0.3296(16)	1.025(22)	2.11	0.077
<i>a06m310W</i>	3	0.3289(16)	0.3303(14)	1.030(19)	2.14	0.073
<i>a06m220</i>	4	0.3036(19)	0.3035(19)	0.926(52)	0.26	0.902
<i>a06m220</i>	3	0.3065(17)	0.3060(16)	0.987(42)	1.22	0.299
<i>a06m220W</i>	4	0.3030(21)	0.3045(17)	1.033(40)	0.51	0.730
<i>a06m220W</i>	3	0.3047(14)	0.3053(13)	1.027(25)	0.33	0.858
<i>a06m135</i>	4	0.2714(24)	0.2716(22)	0.857(48)	0.48	0.886
<i>a06m135</i>	3	0.2735(16)	0.2737(16)	1.008(35)	0.33	0.967

TABLE VII. Comparison of the ground state nucleon mass obtained from fits to the dispersion relation, $E_p^2 = (M_0^{\text{Disp}})^2 + c^2 \mathbf{p}^2$ with $M_0^{2\text{pt}}$ from zero-momentum two-point correlator. Here n_s is the number of states kept in the fits with $n_s = 2$ or 3 implying a frequentist fit and $n_s = 4$ implying an empirical Bayesian fit. The speed of light c^2 , the χ^2/dof and p -value are for the fit to the dispersion relation.

Ensemble ID	t_1/a	4s [t_{\min}, t_{\max}]	3s [t_{\min}, t_{\max}]	$M_1^{(4)}$ GeV	$M_1^{(3)}$ GeV
a06m135	12	[6, 30]	[2, 25]	1.69(11)	1.85(05)
a06m220	13	[7, 30]	[3, 30]	1.87(08)	2.10(06)
a06m220W	11	[4, 20]	[2, 25]	1.82(15)	2.21(11)
a06m310	12	[7, 30]	[3, 30]	1.65(11)	2.09(14)
a06m310W	8	[4, 25]	[2, 25]	2.05(15)	2.37(15)
a09m130W	7	[4, 20]	[2, 20]	1.76(09)	1.82(09)
a09m220	9	[3, 14]	[2, 20]	1.72(09)	2.00(10)
a09m310	7	[2, 18]	[2, 18]	2.06(13)	2.09(16)
a12m220L	7	[2, 15]	[2, 14]	1.69(18)	2.40(03)
a12m220	6	[2, 15]	[1, 12]	1.63(12)	2.39(02)
a12m220S	6	[2, 15]	[2, 10]	1.50(08)	2.40(08)
a12m310	6	[2, 15]	[2, 10]	1.58(09)	2.51(05)
a15m310	4	[1, 10]	[1, 10]	2.04(06)	2.22(03)

TABLE VIII. Results for M_1 from the four-state empirical Bayesian fit (4s) and the three-state frequentist fit (3s). For ensembles with $a \approx 0.12, 0.15$ fm, a two-state frequentist fit is performed, nevertheless, we keep the label “s3” for brevity. The second column gives the approximate time t_1 at which the $m_{\text{eff}}^{(1)}$ reaches the first excited state energy E_1 given by the four-state fit. The time interval used in the four- (three-) state fits to $C^{2\text{pt}}(t)$ is given in the third (fourth) column.

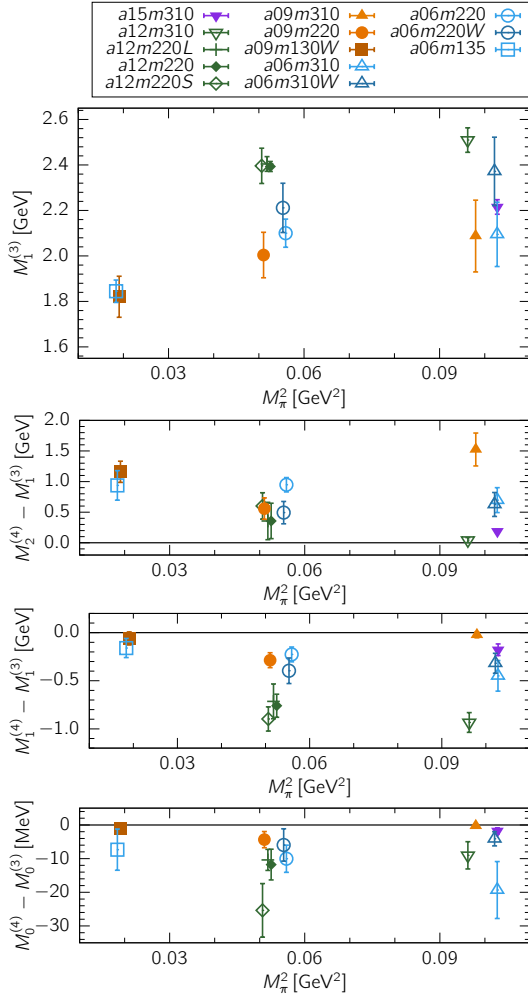


FIG. 21. (Top) The first excited state mass, $M_1^{(3)}$, from the frequentist 3-state (or 2-state) fit. The mass differences $M_2^{(4)} - M_1^{(3)}$ and $M_1^{(4)} - M_1^{(3)}$ are shown in the second and third panels. The difference in the ground state mass, $M_0^{(4)} - M_0^{(3)}$, is given in the bottom panel.

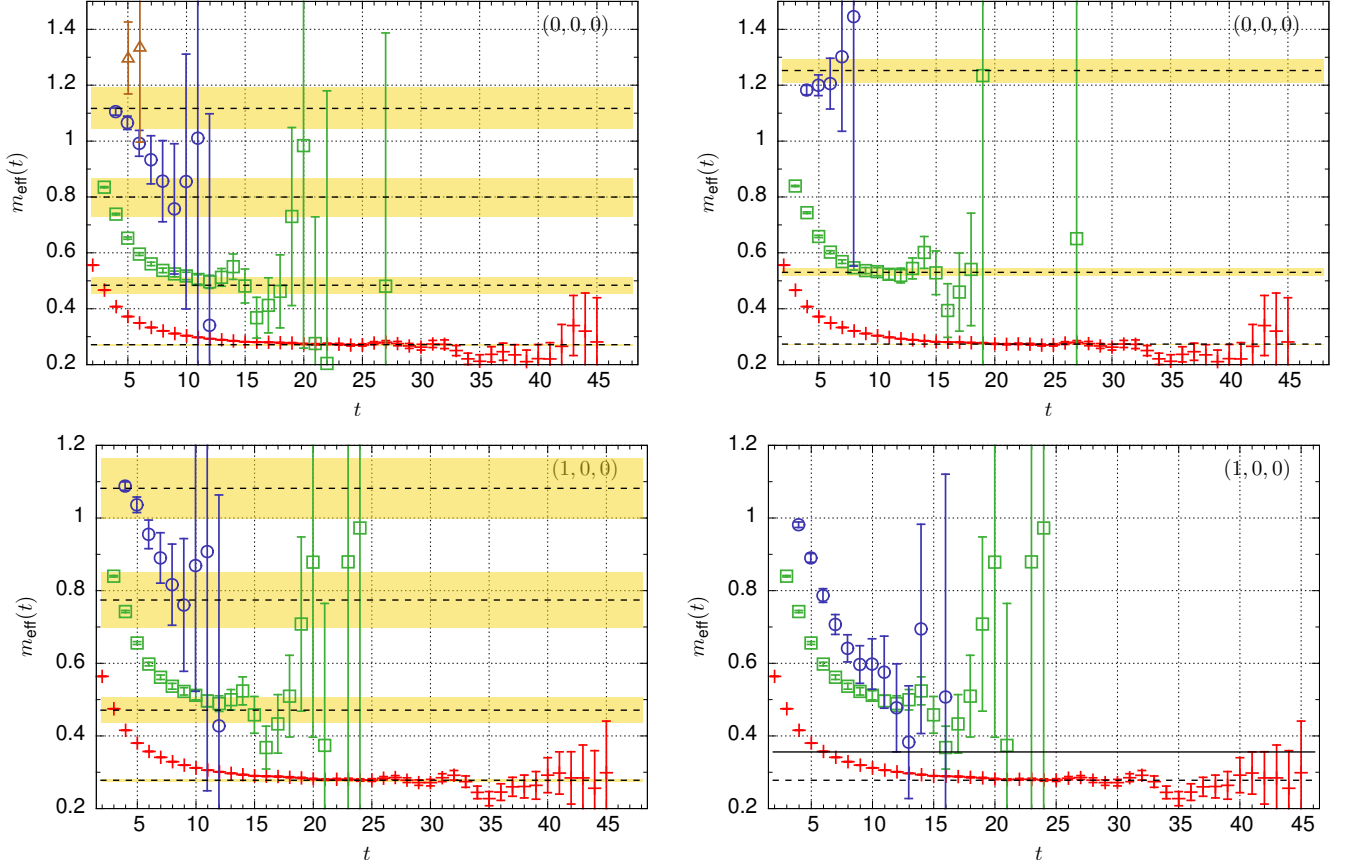


FIG. 22. Data for the effective masses $m_{\text{eff}}^{(n)}$, defined in Eq. (A4), from the a06m135 two-point correlators. Top panel shows results for $\mathbf{p} = \mathbf{0}$ with the E_{n-1} in Eq. (A4) taken from the four-state fit (left) and three-state fit (right). These input energy levels E_n are shown by the dashed lines with yellow error bands. The red plus, green square, and blue circle symbols correspond to $m_{\text{eff}}^{(n)}$ with $n = 0, 1, 2$, respectively. The bottom panel shows $m_{\text{eff}}^{(n)}$ for $\mathbf{p} = 2\pi\mathbf{n}/L$, $\mathbf{n} = (1, 0, 0)$. In the bottom right panel, E_0 is taken from the four-state fit and $E_1 = E_0 + 2M_\pi$ (solid black line) is assumed.

Appendix B: Extrapolation of the nucleon mass M_N to the Physical Point

Here we revisit the extrapolation of the nucleon mass $M_N(a, M_\pi^2, M_\pi L)$ given in Table VII to the physical point and extend the discussion in the Appendix B in Ref. [17]. We use the following CCFV ansatz:

$$M_N = c_0 + c_1 a + c_2 a^2 + c_3 M_\pi^2 + c_4 M_\pi^3 + c_5 M_\pi^2 e^{-M_\pi L}. \quad (\text{B1})$$

Results and the fit parameters c_i for various truncations of this ansatz are given in Table IX. The CCFV fits F1 and B1 are shown in Fig. 23. Our analysis indicates

- The CCFV fits, F1-F4, to the $M_0^{(3)}$ data give slightly smaller continuum M_N than fits to $M_0^{(4)}$ even though $M_0^{(3)} > M_0^{(4)}$ as shown in Fig. 21 (bottom panel) for each of the thirteen ensembles.
- Only F1 ($M_N = 0.939(12)$ GeV) and B1 ($M_N = 0.945(16)$ GeV) fits give estimates consistent with the physical value of $M_N = 939$ GeV. The other fits give ≈ 25 MeV higher values.
- The F3 and B3 fits, which include the higher order M_π^3 term give a c_4 that is roughly consistent with the χ PT prediction $c_4 = 3g_A^2/(32\pi F_\pi^2) = -5.716$. On including a^2 and/or finite volume correction terms in addition to the M_π^3 term, c_4 remains consistent with the χ PT prediction for F1, F2 and F4 fits but becomes smaller for B1, B2 and B4.
- The finite volume coefficient, c_5 , is not well determined in any of the fits. Without it, fits F1 and B1 have small p -value but give results consistent with the experimental value. Including it, the p -value of F2 and B2 fits improves to an acceptable level, but the coefficients of the lattice spacing dependence, c_1 and c_2 , become less well determined. Neglecting the c_2 term (F4 and B4 fits), the c_1 becomes well determined, while the other c_i are essentially unchanged. In these cases, the ~ 25 MeV shifts in the M_N from the F1 or B1 fits persist.

Overall, with the current data, we are not able to determine whether $M_0^{(3)}$ or $M_0^{(4)}$ give better estimates of the ground state nucleon mass. Also, we can at best make four-state fits to the two-point function and three-state fits to the three-point functions.

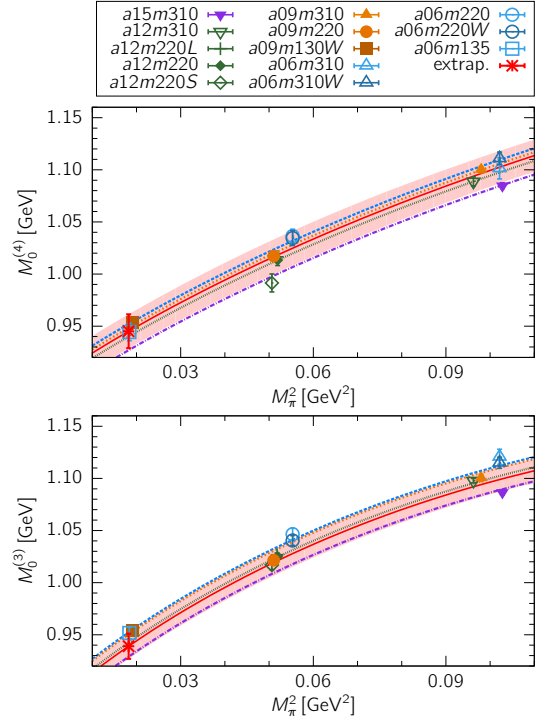


FIG. 23. The result of the chiral-continuum (CC) fit (no finite volume term) to the nucleon mass $M_0^{(4)}$ (B1 fit in Table IX) (top panel) and $M_0^{(3)}$ (F1 fit in Table IX) (bottom panel) is shown by the red line with the error band. The data for B1 and F1 fits given in Table VIII are plotted versus M_π^2 after shifting them in a to $a = 0$ using the CC fits. The CC fit is also shown versus M_π^2 with a set to $a = 0.06$ fm (blue dashed line), 0.09 fm (orange dotted line), 0.12 fm (green dotted line), and 0.15 fm (purple dash-dot line). In a perfect fit, these curves should pass through points with the same color, i.e., with the same lattice spacing a .

Fit	M_N GeV	χ^2/DOF	p	AIC	$c_0[1]$ GeV	$c_1[a]$ GeV fm ⁻¹	$c_2[a^2]$ GeV fm ⁻²	$c_3[M_\pi^2]$ GeV ⁻¹	$c_4[M_\pi^3]$ GeV ⁻²	$c_5[\text{FV}]$ GeV ⁻¹
F1	0.939(12)	2.187	0.025	27.5	0.878(013)	0.41(25)	-3.2(1.2)	4.24(38)	-6.5(1.0)	-
F2	0.954(14)	1.758	0.091	24.3	0.895(015)	0.11(28)	-1.6(1.4)	4.07(38)	-5.9(1.0)	-6.0(2.6)
F3	0.968(04)	2.686	0.004	32.2	0.904(008)	-0.23(04)	-	4.53(36)	-7.3(9)	-
F4	0.969(04)	1.686	0.096	23.5	0.908(008)	-0.19(04)	-	4.13(38)	-6.0(1.0)	-7.4(2.3)
B1	0.945(16)	1.109	0.353	18.9	0.896(017)	0.27(32)	-2.6(1.5)	3.18(46)	-3.6(1.2)	-
B2	0.968(20)	0.675	0.693	16.7	0.922(021)	-0.16(38)	-0.2(1.9)	2.86(48)	-2.5(1.3)	-10.4(5.1)
B3	0.972(05)	1.318	0.221	19.9	0.921(009)	-0.28(04)	-	3.35(44)	-4.2(1.2)	-
B4	0.970(05)	0.592	0.785	14.7	0.924(009)	-0.20(05)	-	2.86(48)	-2.5(1.3)	-10.7(4.0)

TABLE IX. Summary of CCFV fits to $M_N(a, M_\pi^2, M_\pi L)$ using Eq. (B1). Fits $F1$ - $F4$ are to the frequentist (3-state or 2-state) data labeled $M_0^{(3)}$ in the text, and $B1$ - $B4$ are to the 4-state empirical Bayesian fit data and labeled $M_0^{(4)}$. To make the interpretation of coefficients c_i defined in Eq. (B1) easier, we give both the functional dependance within square parentheses and the units. The results for $M_0^{(4)}$ are the same as in Ref. [17], except for a small change in $a06m135$ value due to increased statistics. Fits corresponding to the B2 and B4 were given in Table XV in Ref. [17] (labeled B1 and B2 there) and led to $M_N = 0.976(20)$ GeV and $0.972(6)$ GeV, respectively.

Appendix C: Tables giving Form Factors versus Q^2

The unrenormalized values of the form factors G_A , \tilde{G}_P , and G_P at the various Q^2 values simulated on the thirteen ensembles and extracted using the three analysis strategies \mathcal{S}_{sim} , \mathcal{S}_{A4} , and $\mathcal{S}_{2\text{pt}}$ defined in Section II are given in Tables X—XXII.

$Q^2[\text{GeV}]$	G_A			\tilde{G}_P			G_P		
	\mathcal{S}_{sim}	\mathcal{S}_{A4}	$\mathcal{S}_{2\text{pt}}$	\mathcal{S}_{sim}	\mathcal{S}_{A4}	$\mathcal{S}_{2\text{pt}}$	\mathcal{S}_{sim}	\mathcal{S}_{A4}	$\mathcal{S}_{2\text{pt}}$
0.252(00)	1.007(008)	1.010(009)	0.993(006)	12.53(22)	12.89(23)	11.01(14)	15.12(24)	15.56(23)	13.14(15)
0.483(01)	0.842(007)	0.842(007)	0.822(007)	6.388(126)	6.433(102)	5.827(093)	8.115(143)	8.162(105)	7.386(097)
0.703(02)	0.720(007)	0.720(010)	0.690(008)	3.967(071)	4.046(104)	3.647(072)	5.255(095)	5.357(105)	4.939(081)
0.911(06)	0.648(017)	0.657(020)	0.614(017)	2.890(132)	2.915(148)	2.553(094)	4.080(172)	4.071(160)	3.559(097)
1.102(07)	0.593(011)	0.587(013)	0.561(011)	2.144(082)	2.065(090)	1.978(061)	3.184(133)	3.046(105)	2.856(088)
1.297(09)	0.520(006)	0.524(011)	0.491(013)	1.560(045)	1.613(076)	1.590(078)	2.341(063)	2.418(090)	2.369(117)
1.637(22)	0.450(017)	0.476(025)	0.469(023)	1.018(062)	1.119(087)	1.119(103)	1.662(082)	1.793(118)	1.640(121)
1.803(22)	0.439(029)	0.449(034)	0.452(023)	0.999(106)	1.028(124)	1.050(104)	1.444(133)	1.489(148)	1.290(207)
1.790(29)	0.543(114)	0.458(039)	0.395(056)	1.215(356)	1.002(135)	0.959(204)	1.557(428)	1.121(319)	0.995(972)
1.917(31)	0.428(108)	0.437(024)	0.379(046)	0.911(353)	0.938(085)	1.225(153)	1.455(505)	1.354(166)	1.293(322)

TABLE X. The bare form factors G_A , \tilde{G}_P , and G_P versus Q^2 for the 3 strategies \mathcal{S}_{sim} , \mathcal{S}_{A4} , and $\mathcal{S}_{2\text{pt}}$ on ensemble $a15m310$.

$Q^2[\text{GeV}]$	G_A			\tilde{G}_P			G_P		
	\mathcal{S}_{sim}	\mathcal{S}_{A4}	$\mathcal{S}_{2\text{pt}}$	\mathcal{S}_{sim}	\mathcal{S}_{A4}	$\mathcal{S}_{2\text{pt}}$	\mathcal{S}_{sim}	\mathcal{S}_{A4}	$\mathcal{S}_{2\text{pt}}$
0.176(00)	1.086(011)	1.086(011)	1.050(014)	18.01(29)	17.84(38)	16.51(56)	22.32(36)	22.08(41)	21.15(86)
0.342(01)	0.948(010)	0.937(009)	0.905(013)	9.817(153)	9.501(169)	9.493(281)	12.67(20)	12.27(19)	12.02(33)
0.498(02)	0.844(011)	0.842(012)	0.787(016)	6.505(106)	6.411(155)	5.954(199)	8.635(154)	8.499(206)	8.309(252)
0.646(03)	0.764(013)	0.763(014)	0.686(022)	4.664(087)	4.600(138)	4.124(189)	6.478(133)	6.385(194)	5.863(191)
0.787(04)	0.694(011)	0.691(012)	0.639(016)	3.504(088)	3.454(113)	3.246(123)	4.957(127)	4.891(157)	4.301(162)
0.920(05)	0.649(011)	0.666(013)	0.576(019)	2.882(118)	3.006(076)	2.399(168)	4.015(150)	4.161(106)	3.424(180)
1.178(09)	0.533(010)	0.550(017)	0.506(025)	1.684(068)	1.818(110)	1.651(126)	2.606(074)	2.731(163)	2.433(222)
1.293(10)	0.472(031)	0.463(040)	0.465(025)	1.296(193)	1.295(214)	1.469(150)	2.056(173)	2.048(221)	1.659(259)
1.315(19)	0.462(016)	0.538(047)	0.482(336)	1.175(083)	1.609(253)	1.264(1.241)	2.104(152)	2.446(317)	1.680(546)
1.435(18)	0.471(013)	0.488(032)	0.462(044)	1.224(066)	1.293(138)	1.438(258)	1.908(087)	1.984(223)	0.840(515)

TABLE XI. The bare form factors G_A , \tilde{G}_P , and G_P versus Q^2 for the 3 strategies \mathcal{S}_{sim} , \mathcal{S}_{A4} , and $\mathcal{S}_{2\text{pt}}$ on ensemble $a12m310$.

$Q^2[\text{GeV}]$	G_A			\tilde{G}_P			G_P		
	\mathcal{S}_{sim}	\mathcal{S}_{A4}	$\mathcal{S}_{2\text{pt}}$	\mathcal{S}_{sim}	\mathcal{S}_{A4}	$\mathcal{S}_{2\text{pt}}$	\mathcal{S}_{sim}	\mathcal{S}_{A4}	$\mathcal{S}_{2\text{pt}}$
0.175(01)	1.129(033)	1.123(034)	1.084(020)	19.73(92)	19.75(1.08)	16.14(69)	26.03(1.19)	26.27(1.49)	21.67(96)
0.339(03)	0.918(037)	0.920(033)	0.912(020)	9.517(656)	9.580(552)	8.373(527)	14.44(1.11)	14.83(98)	12.60(91)
0.490(06)	0.814(031)	0.821(044)	0.766(027)	5.271(346)	5.634(304)	5.165(360)	8.344(603)	9.064(487)	8.620(681)
0.636(09)	0.749(120)	0.749(044)	0.705(037)	4.284(877)	4.166(328)	3.744(288)	6.528(1.027)	6.563(449)	6.237(399)
0.773(10)	0.629(039)	0.646(041)	0.640(024)	3.016(409)	3.123(268)	2.743(171)	7.386(2.229)	6.484(705)	5.342(341)
0.909(13)	0.587(069)	0.627(045)	0.593(028)	2.568(343)	2.763(309)	2.276(212)	4.458(804)	4.516(556)	3.919(353)
1.178(23)	0.461(144)	0.514(062)	0.502(041)	1.110(705)	1.689(269)	1.515(176)	2.710(222)	3.422(587)	3.156(390)
1.307(25)	0.467(115)	0.571(059)	0.511(039)	1.116(1.966)	1.810(250)	1.480(193)	2.183(5.142)	2.986(644)	2.890(476)
1.238(33)	0.509(049)	0.551(077)	0.555(068)	1.247(181)	1.605(316)	1.499(288)	2.975(858)	3.966(821)	3.586(682)
1.358(36)	0.415(037)	0.425(135)	0.440(050)	0.771(163)	0.712(764)	0.890(225)	2.597(424)	3.625(1.536)	2.818(614)

TABLE XII. The bare form factors G_A , \tilde{G}_P , and G_P versus Q^2 for the 3 strategies \mathcal{S}_{sim} , \mathcal{S}_{A4} , and $\mathcal{S}_{2\text{pt}}$ on ensemble $a12m220S$.

$Q^2[\text{GeV}]$	G_A			\tilde{G}_P			G_P		
	\mathcal{S}_{sim}	\mathcal{S}_{A4}	$\mathcal{S}_{2\text{pt}}$	\mathcal{S}_{sim}	\mathcal{S}_{A4}	$\mathcal{S}_{2\text{pt}}$	\mathcal{S}_{sim}	\mathcal{S}_{A4}	$\mathcal{S}_{2\text{pt}}$
0.105(00)	1.174(020)	1.169(021)	1.145(017)	28.84(1.16)	28.37(1.27)	24.11(1.40)	38.36(1.42)	37.84(1.55)	32.00(2.09)
0.206(02)	1.033(014)	1.041(017)	1.031(022)	15.55(42)	15.93(52)	14.53(97)	21.95(58)	22.23(66)	20.38(1.43)
0.301(02)	0.954(017)	0.956(017)	0.930(021)	10.75(34)	10.93(34)	9.99(48)	15.17(47)	15.30(49)	13.78(59)
0.391(03)	0.908(017)	0.911(017)	0.900(021)	7.975(219)	8.011(221)	7.498(345)	11.51(34)	11.43(34)	10.44(41)
0.482(04)	0.834(014)	0.836(016)	0.812(021)	6.182(192)	6.168(240)	5.752(262)	9.135(300)	9.236(356)	8.444(356)
0.568(05)	0.784(018)	0.787(021)	0.749(024)	4.988(200)	5.142(246)	4.601(249)	7.746(282)	7.955(344)	6.803(348)
0.732(08)	0.690(015)	0.730(029)	0.671(028)	3.404(152)	3.746(303)	3.246(219)	5.518(262)	6.051(497)	5.145(361)
0.808(10)	0.686(028)	0.705(033)	0.644(031)	3.213(252)	3.323(218)	2.850(237)	5.606(475)	5.833(388)	4.690(377)
0.806(12)	0.676(043)	0.711(035)	0.643(045)	3.147(203)	3.077(357)	2.885(321)	5.421(360)	5.058(541)	4.995(556)
0.884(12)	0.655(023)	0.671(025)	0.622(036)	2.579(184)	2.562(240)	2.693(266)	4.085(261)	4.115(295)	3.753(470)

TABLE XIII. The bare form factors G_A , \tilde{G}_P , and G_P versus Q^2 for the 3 strategies \mathcal{S}_{sim} , \mathcal{S}_{A4} , and $\mathcal{S}_{2\text{pt}}$ on ensemble $a12m220$.

$Q^2[\text{GeV}]$	G_A			\tilde{G}_P			G_P		
	\mathcal{S}_{sim}	\mathcal{S}_{A4}	$\mathcal{S}_{2\text{pt}}$	\mathcal{S}_{sim}	\mathcal{S}_{A4}	$\mathcal{S}_{2\text{pt}}$	\mathcal{S}_{sim}	\mathcal{S}_{A4}	$\mathcal{S}_{2\text{pt}}$
0.067(0)	1.235(20)	1.259(16)	1.199(09)	39.90(1.21)	40.42(1.12)	30.88(2.09)	52.61(1.52)	52.68(1.37)	40.29(3.15)
0.132(0)	1.129(10)	1.150(09)	1.118(08)	24.34(55)	24.51(45)	20.55(1.17)	32.11(63)	32.17(53)	27.08(1.63)
0.195(0)	1.061(09)	1.078(08)	1.052(09)	17.24(36)	17.22(26)	15.09(68)	23.01(42)	23.01(32)	20.17(95)
0.257(1)	0.982(11)	1.008(09)	0.983(13)	12.68(41)	13.01(19)	11.58(44)	17.74(41)	17.98(27)	16.02(68)
0.316(1)	0.944(08)	0.961(09)	0.936(12)	10.34(21)	10.40(18)	9.30(27)	14.34(27)	14.43(22)	12.98(37)
0.374(1)	0.907(10)	0.921(13)	0.890(14)	8.719(155)	8.623(250)	7.765(203)	12.19(24)	12.11(31)	10.99(29)
0.487(2)	0.822(29)	0.839(09)	0.808(14)	6.264(153)	6.239(091)	5.576(124)	9.003(302)	9.046(132)	8.146(154)
0.541(3)	0.782(15)	0.802(12)	0.771(16)	5.503(129)	5.347(173)	4.894(126)	8.083(176)	7.852(241)	7.260(159)
0.541(3)	0.776(15)	0.797(10)	0.770(17)	5.152(168)	5.075(130)	4.883(130)	7.922(237)	7.606(199)	7.429(190)
0.595(3)	0.739(13)	0.766(09)	0.741(16)	4.549(105)	4.477(110)	4.264(120)	6.992(210)	6.920(168)	6.565(145)

TABLE XIV. The bare form factors G_A , \tilde{G}_P , and G_P versus Q^2 for the 3 strategies \mathcal{S}_{sim} , \mathcal{S}_{A4} , and $\mathcal{S}_{2\text{pt}}$ on ensemble $a12m220L$.

$Q^2[\text{GeV}]$	G_A			\tilde{G}_P			G_P		
	\mathcal{S}_{sim}	\mathcal{S}_{A4}	$\mathcal{S}_{2\text{pt}}$	\mathcal{S}_{sim}	\mathcal{S}_{A4}	$\mathcal{S}_{2\text{pt}}$	\mathcal{S}_{sim}	\mathcal{S}_{A4}	$\mathcal{S}_{2\text{pt}}$
0.183(00)	1.043(06)	1.043(06)	1.053(04)	17.38(22)	17.27(20)	14.60(30)	21.90(21)	21.76(18)	18.35(35)
0.356(01)	0.894(06)	0.894(07)	0.907(06)	9.238(099)	9.231(105)	8.316(185)	12.36(14)	12.37(12)	11.24(25)
0.520(04)	0.793(09)	0.794(09)	0.795(12)	6.027(123)	6.047(103)	5.594(178)	8.372(148)	8.399(126)	7.931(253)
0.673(04)	0.714(09)	0.715(09)	0.717(09)	4.325(084)	4.313(082)	4.042(077)	6.225(108)	6.208(103)	5.776(086)
0.819(08)	0.647(07)	0.659(10)	0.652(09)	3.284(067)	3.370(079)	3.115(091)	4.889(103)	4.989(111)	4.620(103)
0.961(13)	0.602(07)	0.609(12)	0.591(13)	2.612(057)	2.710(084)	2.482(079)	3.938(082)	4.059(114)	3.834(106)
1.197(09)	0.531(14)	0.565(25)	0.521(09)	1.906(082)	2.028(121)	1.676(046)	3.116(126)	3.198(114)	2.781(063)
1.323(13)	0.498(10)	0.506(16)	0.489(08)	1.513(076)	1.601(093)	1.455(047)	2.535(120)	2.663(131)	2.455(123)
1.325(17)	0.449(12)	0.529(34)	0.482(24)	1.352(080)	1.687(162)	1.438(104)	2.312(138)	2.783(174)	2.319(131)
1.421(14)	0.481(23)	0.513(30)	0.470(11)	1.430(141)	1.519(146)	1.296(052)	2.435(240)	2.560(197)	2.216(111)

TABLE XV. The bare form factors G_A , \tilde{G}_P , and G_P versus Q^2 for the 3 strategies \mathcal{S}_{sim} , \mathcal{S}_{A4} , and $\mathcal{S}_{2\text{pt}}$ on ensemble $a09m310$.

$Q^2[\text{GeV}]$	G_A			\tilde{G}_P			G_P		
	\mathcal{S}_{sim}	\mathcal{S}_{A4}	$\mathcal{S}_{2\text{pt}}$	\mathcal{S}_{sim}	\mathcal{S}_{A4}	$\mathcal{S}_{2\text{pt}}$	\mathcal{S}_{sim}	\mathcal{S}_{A4}	$\mathcal{S}_{2\text{pt}}$
0.086(0)	1.185(17)	1.181(17)	1.169(10)	34.73(1.00)	34.12(92)	27.06(88)	47.06(1.16)	46.25(1.03)	36.91(1.17)
0.169(0)	1.063(11)	1.060(11)	1.074(09)	19.29(39)	19.16(38)	17.17(48)	27.19(45)	27.01(45)	23.67(66)
0.248(1)	0.978(10)	0.974(10)	0.986(09)	13.11(25)	13.04(25)	11.99(30)	18.90(31)	18.85(30)	17.25(48)
0.324(1)	0.925(11)	0.922(11)	0.920(11)	9.940(202)	9.784(217)	8.960(227)	14.41(28)	14.19(27)	13.22(33)
0.398(2)	0.862(08)	0.859(09)	0.858(10)	7.665(141)	7.563(146)	7.158(154)	11.59(19)	11.46(19)	10.67(24)
0.470(2)	0.807(09)	0.806(09)	0.802(11)	6.165(119)	6.086(124)	5.736(134)	9.556(168)	9.451(172)	8.847(189)
0.608(4)	0.726(10)	0.725(10)	0.719(12)	4.401(081)	4.379(090)	4.142(101)	7.007(131)	7.020(136)	6.462(159)
0.674(4)	0.687(11)	0.694(11)	0.683(13)	3.807(084)	3.772(088)	3.532(104)	6.187(137)	6.169(135)	5.456(160)
0.671(5)	0.706(09)	0.711(14)	0.690(16)	3.882(070)	3.935(095)	3.538(131)	6.299(162)	6.333(165)	5.616(208)
0.736(5)	0.664(11)	0.677(12)	0.654(13)	3.351(105)	3.362(111)	3.147(102)	5.480(177)	5.473(176)	4.962(178)

TABLE XVI. The bare form factors G_A , \tilde{G}_P , and G_P versus Q^2 for the 3 strategies \mathcal{S}_{sim} , \mathcal{S}_{A4} , and $\mathcal{S}_{2\text{pt}}$ on ensemble $a09m220$.

$Q^2[\text{GeV}]$	G_A			\tilde{G}_P			G_P		
	\mathcal{S}_{sim}	\mathcal{S}_{A4}	$\mathcal{S}_{2\text{pt}}$	\mathcal{S}_{sim}	\mathcal{S}_{A4}	$\mathcal{S}_{2\text{pt}}$	\mathcal{S}_{sim}	\mathcal{S}_{A4}	$\mathcal{S}_{2\text{pt}}$
0.049(0)	1.284(37)	1.281(35)	1.197(11)	66.90(4.61)	67.10(3.01)	38.95(1.00)	98.55(6.16)	98.65(4.23)	57.55(1.44)
0.097(0)	1.153(19)	1.152(20)	1.141(10)	36.15(1.21)	34.92(94)	25.08(55)	55.27(1.97)	53.17(1.32)	38.23(92)
0.143(0)	1.091(17)	1.092(17)	1.094(10)	24.32(73)	23.94(58)	18.69(42)	36.65(1.08)	36.14(80)	28.41(65)
0.189(1)	1.014(13)	1.022(17)	1.044(10)	17.42(36)	17.56(41)	14.58(32)	26.35(65)	26.32(59)	22.00(50)
0.234(1)	0.971(12)	0.976(13)	0.997(09)	13.80(31)	13.76(28)	11.88(26)	21.34(49)	21.09(38)	18.08(34)
0.277(1)	0.942(13)	0.945(13)	0.957(10)	11.57(29)	11.55(24)	10.00(23)	17.75(37)	17.70(33)	15.51(32)
0.361(2)	0.877(11)	0.867(13)	0.881(12)	8.244(191)	8.044(197)	7.399(168)	12.84(24)	12.85(28)	11.71(26)
0.403(3)	0.839(13)	0.839(13)	0.847(13)	7.165(179)	7.100(180)	6.517(170)	11.25(28)	11.22(26)	10.30(25)
0.404(4)	0.824(18)	0.822(17)	0.827(19)	6.833(225)	6.806(241)	6.315(216)	11.02(41)	10.97(41)	10.21(35)
0.443(4)	0.804(14)	0.800(13)	0.804(15)	6.399(169)	6.150(203)	5.797(148)	10.24(25)	9.999(276)	9.110(269)

TABLE XVII. The bare form factors G_A , \tilde{G}_P , and G_P versus Q^2 for the 3 strategies \mathcal{S}_{sim} , \mathcal{S}_{A4} , and $\mathcal{S}_{2\text{pt}}$ on ensemble $a09m130W$.

$Q^2[\text{GeV}]$	G_A			\tilde{G}_P			G_P		
	\mathcal{S}_{sim}	\mathcal{S}_{A4}	$\mathcal{S}_{2\text{pt}}$	\mathcal{S}_{sim}	\mathcal{S}_{A4}	$\mathcal{S}_{2\text{pt}}$	\mathcal{S}_{sim}	\mathcal{S}_{A4}	$\mathcal{S}_{2\text{pt}}$
0.190(1)	1.022(21)	1.010(23)	1.033(17)	16.99(64)	17.19(68)	14.40(49)	-	-	-
0.365(2)	0.868(15)	0.857(18)	0.870(15)	8.793(230)	8.997(256)	7.911(221)	-	-	-
0.528(3)	0.780(22)	0.774(22)	0.770(20)	6.151(188)	6.149(210)	5.048(228)	-	-	-
0.690(5)	0.669(36)	0.696(34)	0.670(25)	3.913(403)	4.303(242)	3.543(257)	-	-	-
0.840(6)	0.599(29)	0.614(26)	0.614(19)	3.080(168)	3.243(205)	2.932(192)	-	-	-

TABLE XVIII. The bare form factors G_A , \tilde{G}_P , and G_P versus Q^2 for the 3 strategies \mathcal{S}_{sim} , \mathcal{S}_{A4} , and $\mathcal{S}_{2\text{pt}}$ on ensemble $a06m310W$. Data for G_P were, by accident, not saved.

$Q^2[\text{GeV}]$	G_A			\tilde{G}_P			G_P		
	\mathcal{S}_{sim}	\mathcal{S}_{A4}	$\mathcal{S}_{2\text{pt}}$	\mathcal{S}_{sim}	\mathcal{S}_{A4}	$\mathcal{S}_{2\text{pt}}$	\mathcal{S}_{sim}	\mathcal{S}_{A4}	$\mathcal{S}_{2\text{pt}}$
0.189(01)	1.001(15)	1.007(23)	1.020(17)	15.67(72)	16.28(84)	15.11(64)	-	-	-
0.365(03)	0.853(10)	0.856(14)	0.880(17)	8.451(313)	8.635(228)	8.236(291)	-	-	-
0.532(07)	0.743(12)	0.745(17)	0.723(29)	5.441(168)	5.546(188)	4.964(297)	-	-	-
0.683(10)	0.677(12)	0.718(28)	0.663(32)	3.926(125)	4.409(216)	3.967(368)	-	-	-
0.846(12)	0.599(14)	0.618(21)	0.554(42)	2.929(088)	3.120(105)	2.762(240)	-	-	-

TABLE XIX. The bare form factors G_A , \tilde{G}_P , and G_P versus Q^2 for the 3 strategies \mathcal{S}_{sim} , \mathcal{S}_{A4} , and $\mathcal{S}_{2\text{pt}}$ on ensemble $a06m310$. Data for G_P were, by accident, not saved.

$Q^2[\text{GeV}]$	G_A			\tilde{G}_P			G_P		
	\mathcal{S}_{sim}	\mathcal{S}_{A4}	$\mathcal{S}_{2\text{pt}}$	\mathcal{S}_{sim}	\mathcal{S}_{A4}	$\mathcal{S}_{2\text{pt}}$	\mathcal{S}_{sim}	\mathcal{S}_{A4}	$\mathcal{S}_{2\text{pt}}$
0.109(0)	1.161(48)	1.152(37)	1.124(21)	29.89(1.99)	30.67(1.62)	22.81(89)	-	-	-
0.213(1)	1.022(29)	0.999(23)	1.008(20)	15.51(71)	15.35(56)	13.64(40)	-	-	-
0.313(2)	0.909(24)	0.898(25)	0.901(27)	9.762(387)	10.030(490)	8.987(396)	-	-	-
0.412(6)	0.860(34)	0.860(31)	0.801(52)	7.669(431)	7.993(393)	6.817(437)	-	-	-
0.504(6)	0.777(27)	0.774(27)	0.762(35)	5.701(264)	5.694(253)	5.539(305)	-	-	-

TABLE XX. The bare form factors G_A , \tilde{G}_P , and G_P versus Q^2 for the 3 strategies \mathcal{S}_{sim} , \mathcal{S}_{A4} , and $\mathcal{S}_{2\text{pt}}$ on ensemble $a06m220W$. Data for G_P were, by accident, not saved.

$Q^2[\text{GeV}]$	G_A			\tilde{G}_P			G_P		
	\mathcal{S}_{sim}	\mathcal{S}_{A4}	$\mathcal{S}_{2\text{pt}}$	\mathcal{S}_{sim}	\mathcal{S}_{A4}	$\mathcal{S}_{2\text{pt}}$	\mathcal{S}_{sim}	\mathcal{S}_{A4}	$\mathcal{S}_{2\text{pt}}$
0.110(0)	1.186(36)	1.149(34)	1.124(16)	30.75(1.54)	30.47(1.37)	21.36(66)	43.30(2.01)	42.85(1.66)	29.59(67)
0.216(1)	1.005(15)	0.973(20)	1.007(15)	16.04(47)	15.59(46)	13.08(36)	22.74(66)	22.14(54)	18.43(36)
0.318(2)	0.910(24)	0.862(20)	0.918(18)	10.53(42)	10.08(31)	9.228(312)	14.83(52)	14.93(41)	13.39(32)
0.414(5)	0.823(23)	0.807(22)	0.850(22)	7.449(289)	7.439(259)	6.917(272)	11.14(33)	10.98(35)	10.37(32)
0.509(6)	0.757(18)	0.754(19)	0.777(20)	5.807(188)	5.781(186)	5.295(199)	8.463(317)	8.621(274)	8.081(259)

TABLE XXI. The bare form factors G_A , \tilde{G}_P , and G_P versus Q^2 for the strategies \mathcal{S}_{sim} , \mathcal{S}_{A4} , and $\mathcal{S}_{2\text{pt}}$ on ensemble $a06m220$.

$Q^2[\text{GeV}]$	G_A			\tilde{G}_P			G_P		
	\mathcal{S}_{sim}	\mathcal{S}_{A4}	$\mathcal{S}_{2\text{pt}}$	\mathcal{S}_{sim}	\mathcal{S}_{A4}	$\mathcal{S}_{2\text{pt}}$	\mathcal{S}_{sim}	\mathcal{S}_{A4}	$\mathcal{S}_{2\text{pt}}$
0.051(0)	1.201(51)	1.211(56)	1.179(20)	59.23(4.34)	61.92(4.15)	35.54(1.42)	94.52(6.52)	99.18(6.04)	56.03(2.10)
0.102(1)	1.075(33)	1.075(34)	1.109(16)	32.30(1.88)	32.17(1.48)	22.04(64)	54.37(2.91)	54.56(2.25)	37.84(1.41)
0.151(2)	0.966(31)	0.966(34)	1.041(17)	20.25(1.02)	20.52(97)	16.21(55)	36.14(1.68)	36.60(1.55)	28.47(1.20)
0.198(2)	0.940(24)	0.948(25)	1.008(18)	15.71(74)	15.95(57)	13.47(48)	26.73(1.01)	26.96(85)	22.41(73)
0.246(3)	0.876(20)	0.877(22)	0.940(20)	11.82(47)	11.75(41)	10.33(31)	21.32(60)	21.32(66)	18.53(59)
0.294(4)	0.836(17)	0.838(21)	0.876(32)	9.153(297)	9.397(327)	8.750(352)	16.88(49)	17.34(54)	15.85(55)
0.386(6)	0.778(19)	0.782(18)	0.788(37)	6.977(212)	6.977(182)	6.705(320)	12.84(37)	12.83(37)	11.73(44)
0.431(5)	0.755(19)	0.755(18)	0.740(34)	5.883(182)	5.862(188)	5.665(321)	11.17(34)	11.25(35)	10.39(46)
0.432(5)	0.739(22)	0.750(21)	0.753(37)	6.129(219)	6.163(202)	5.909(331)	11.38(41)	11.33(39)	10.79(56)
0.475(6)	0.718(21)	0.736(19)	0.707(28)	5.386(184)	5.369(168)	4.757(193)	9.941(344)	9.931(313)	9.117(407)

TABLE XXII. The bare form factors G_A , \tilde{G}_P , and G_P versus Q^2 for the 3 strategies \mathcal{S}_{sim} , \mathcal{S}_{A4} , and $\mathcal{S}_{2\text{pt}}$ on ensemble $a06m135$.

Appendix D: Results for g_A , $\langle r_A^2 \rangle$, g_P^* and $g_{\pi NN}$

The results for g_A , $\langle r_A^2 \rangle$, g_P^* , $g_{\pi NN}F_\pi$ and $\frac{g_{\pi NN}F_\pi}{M_N}$ from the thirteen ensembles are given in Tables XXIII, XXIV and XXV.

ID	g_A	$\langle r_A^2 \rangle$	χ^2/dof	p
a15m310	1.211(30)	0.229(11)	1.07	0.38
a12m310	1.209(40)	0.221(17)	0.29	0.94
a12m220L	1.246(43)	0.300(25)	2.39	0.01
a12m220	1.234(46)	0.292(28)	0.87	0.56
a12m220S	1.331(80)	0.331(59)	0.25	0.96
a09m310	1.188(49)	0.250(11)	0.81	0.56
a09m220	1.233(54)	0.297(21)	1.33	0.21
a09m130W	1.272(65)	0.446(72)	1.30	0.22
a06m310	1.158(44)	0.239(18)	0.56	0.74
a06m310W	1.165(48)	0.221(24)	0.59	0.71
a06m220	1.300(59)	0.368(45)	0.69	0.63
a06m220W	1.261(70)	0.311(50)	0.42	0.83
a06m135	1.349(85)	0.74(13)	0.63	0.71

TABLE XXIII. Results for g_A and $\langle r_A^2 \rangle$ given by z^2 fits to the axial form factor, $G_A(Q^2)$, obtained with the \mathcal{S}_{sim} strategy. The χ^2/dof and p -value of the fits are also given.

ID	g_P^*	$g_{\pi NN}F_\pi$	$\frac{g_{\pi NN}F_\pi}{M_N}$	χ^2/dof	p
a15m310	2.22(08)	1.30(06)	1.20(05)	0.46	0.84
a12m310	2.46(09)	1.36(06)	1.25(06)	0.45	0.85
a12m220L	4.06(16)	1.26(06)	1.24(05)	0.92	0.52
a12m220	3.81(20)	1.18(08)	1.16(07)	0.47	0.91
a12m220S	4.62(32)	1.47(12)	1.48(12)	0.79	0.58
a09m310	2.42(10)	1.38(06)	1.25(06)	0.43	0.86
a09m220	4.11(20)	1.28(07)	1.26(07)	0.66	0.76
a09m130W	8.78(58)	1.28(10)	1.34(10)	0.73	0.70
a06m310	2.20(13)	1.29(09)	1.17(07)	0.23	0.95
a06m310W	2.29(11)	1.34(08)	1.20(07)	1.49	0.19
a06m220	4.28(23)	1.45(09)	1.40(09)	0.42	0.84
a06m220W	3.95(26)	1.33(10)	1.29(09)	0.91	0.48
a06m135	8.39(73)	1.18(13)	1.25(13)	0.83	0.55

TABLE XXV. The values of g_P^* , $g_{\pi NN}F_\pi$ and $g_{\pi NN}F_\pi/M_N$ given by z^2 fits to \mathcal{S}_{sim} strategy data for \tilde{F}_P defined in Eq. (39). The χ^2/dof and p -value of the fits are also given, and F_π and M_N are in units of GeV.

ID	g_P^*	$g_{\pi NN}F_\pi$	$\frac{g_{\pi NN}F_\pi}{M_N}$	χ^2/dof	p
a15m310	2.16(07)	1.24(05)	1.15(04)	0.92	0.43
a12m310	2.44(09)	1.33(06)	1.22(05)	0.61	0.61
a12m220L	4.02(16)	1.23(05)	1.21(05)	1.34	0.23
a12m220	3.73(18)	1.14(06)	1.13(06)	0.68	0.69
a12m220S	4.71(36)	1.47(13)	1.48(13)	0.46	0.71
a09m310	2.37(10)	1.32(06)	1.20(05)	0.86	0.46
a09m220	3.98(18)	1.21(06)	1.19(06)	1.15	0.33
a09m130W	8.38(46)	1.19(07)	1.25(07)	1.05	0.39
a06m310	2.20(13)	1.28(09)	1.16(07)	0.01	0.99
a06m310W	2.31(16)	1.34(12)	1.20(11)	3.48	0.03
a06m220	4.38(29)	1.48(12)	1.43(12)	0.27	0.77
a06m220W	4.16(38)	1.41(16)	1.37(15)	1.36	0.26
a06m135	8.35(70)	1.16(11)	1.23(11)	1.44	0.23

TABLE XXIV. Results for g_P^* , $g_{\pi NN}F_\pi$ and $g_{\pi NN}F_\pi/M_N$ given by the “PD” fits (defined in Eq. (40)) to \tilde{G}_P obtained using \mathcal{S}_{sim} strategy. The χ^2/dof and p -value of the fits are also given, and F_π and M_N are in units of GeV.

Appendix E: Summary of CCFV Fits

The results of the 13-point CCFV fits to the \mathcal{S}_{sim} data and the fit parameters, including the χ^2/DOF and the p -value, for g_A and $\langle r_A^2 \rangle$ in Table XXVI; g_P^* in Tables XXVII and XXVIII; and $g_{\pi NN}$ in Table XXIX.

χ^2/DOF	p	AIC	AICc	$c_0[1]$	$c_1[a]$ fm^{-1}	$c_2[M_\pi^2]$ GeV^{-2}	$c_3[\text{FV}]$ GeV^{-2}	
13-point CCFV fits to g_A data obtained with \mathcal{S}_{sim} and z^2 fit								
1.296(050)	0.254	0.986	10.3	15.3	1.332(058)	0.002(477)	-1.967(719)	41.370(37.926)
1.277(047)	0.348	0.968	9.5	12.1	1.303(052)	0.284(402)	-1.402(498)	-
1.219(042)	1.037	0.410	15.4	16.6	1.219(042)	0.039(392)	-	-
1.302(032)	0.361	0.971	8.0	9.2	1.326(040)	-	-1.325(486)	-
1.248(027)	0.940	0.500	14.3	15.5	1.248(027)	-	-	-23.153(22.360)
1.223(013)	0.951	0.494	13.4	13.8	1.223(013)	-	-	-
13-point CCFV fit to $\langle r_A^2 \rangle$ data obtained with \mathcal{S}_{sim} and z^2 fit								
0.418(033)	1.310	0.225	19.8	24.8	0.457(040)	-0.489(260)	-2.169(449)	34.126(20.944)
0.384(025)	1.445	0.154	20.4	23.1	0.413(029)	-0.168(170)	-1.596(280)	-
0.287(019)	4.267	0.000	50.9	52.1	0.287(019)	-0.332(167)	-	-
0.369(021)	1.403	0.164	19.4	20.6	0.399(025)	-	-1.643(276)	-
0.298(013)	3.241	0.000	39.6	40.8	0.298(013)	-	-	-38.490(9.863)
0.251(006)	4.240	0.000	52.9	53.2	0.251(006)	-	-	-

TABLE XXVI. Summary of the parameters in the 13-point CCFV fit to g_A and $\langle r_A^2 \rangle$. The data used are given in Table XXIII. These were obtained by fitting the Q^2 behavior of G_A from the \mathcal{S}_{sim} strategy and using the z^2 truncation. Details are given in Sec. III A.

g_P^*	χ^2/DOF	p	AIC	AICc	$c_0[1]$	$c_1[a]$ fm^{-1}	$c_2[M_\pi^2]$ GeV^{-2}	$c_3[\text{FV}]$ GeV^{-2}
g_P^* using \mathcal{S}_{sim} data and \tilde{F}_P fit using z^2 , 13-point CCFV fit								
9.300(459)	0.897	0.527	16.1	21.1	0.261(015)	-0.117(124)	-0.018(180)	6.359(9.373)
9.213(441)	0.853	0.577	14.5	17.2	0.257(013)	-0.079(110)	0.067(129)	-
9.301(408)	0.800	0.640	12.8	14.0	0.261(011)	-0.066(107)	-	-
8.969(281)	0.822	0.618	13.0	14.2	0.251(010)	-	0.047(126)	-
8.968(240)	0.815	0.625	13.0	14.2	0.251(007)	-	-	2.739(5.929)
9.062(124)	0.765	0.687	11.2	11.5	0.254(003)	-	-	-
g_P^* using \mathcal{S}_{sim} data and \tilde{G}_P fit using Eq. 40, 13-point CCFV fit								
9.248(484)	1.182	0.301	18.6	23.6	0.258(015)	-0.178(135)	0.075(181)	4.550(9.448)
9.167(454)	1.087	0.368	16.9	19.5	0.255(013)	-0.148(119)	0.138(127)	-
9.274(443)	1.096	0.360	16.1	17.3	0.260(012)	-0.105(112)	-	-
8.708(264)	1.129	0.333	16.4	17.6	0.243(009)	-	0.086(119)	-
8.793(228)	1.159	0.310	16.7	17.9	0.247(006)	-	-	2.360(5.527)
8.876(123)	1.078	0.374	14.9	15.3	0.249(003)	-	-	-

TABLE XXVII. Summary of parameters values in the 13-point CCFV fit (see Eq. (29)) for obtaining g_P^* . The data used are given in Tables XXIV and XXV. In the top half, the quantity $(Q^{*2} + M_\pi^2)g_P^* = 2m_\mu M_N \tilde{F}_P(Q^{*2})$, with \tilde{F}_P is defined in Eq. (39) and fit using z^2 , is extrapolated, while in the bottom half $(Q^{*2} + M_\pi^2)g_P^* = (Q^{*2} + M_\pi^2)(m_\mu/2M_N)\tilde{G}_P(Q^{*2})$ is used. The extrapolated results are then converted to g_P^* by dividing by the physical value of $(Q^{*2} + M_\pi^2)$. Details are given in Sec. IV.

g_P^*	χ^2/DOF	p	AIC	AICc	$c_0[1]$	$c_1[a]$ fm $^{-1}$	$c_2[M_\pi^2]$ GeV $^{-2}$	$c_3[\text{FV}]$ GeV $^{-2}$	$c_4[\text{pole}]$ GeV 2
g_P^* using \mathcal{S}_{sim} data and z^2 fit to $\tilde{F}_P(Q^{*2})$, 13-point CCFV fit									
8.763(479)	0.978	0.451	17.8	26.4	0.917(944)	-1.327(1.523)	-6.027(6.740)	83.890(129.644)	0.223(035)
8.770(479)	0.916	0.510	16.2	21.2	0.692(878)	-0.655(1.114)	-3.825(5.817)	-	0.228(034)
9.019(292)	0.867	0.563	14.7	17.3	0.127(182)	-0.679(1.113)	-	-	0.249(011)
8.714(469)	0.859	0.572	14.6	17.3	0.631(872)	-	-3.935(5.814)	-	0.229(034)
8.950(294)	0.900	0.532	15.0	17.7	0.086(226)	-	-	-18.315(86.479)	0.249(014)
8.969(281)	0.822	0.618	13.0	14.2	0.047(126)	-	-	-	0.250(011)
g_P^* using \mathcal{S}_{sim} data and “PD” fit Eq. (40), 13-point CCFV fit									
8.590(418)	1.273	0.252	20.2	28.8	1.075(905)	-2.081(1.715)	-6.246(6.684)	83.651(136.326)	0.214(031)
8.585(418)	1.174	0.307	18.6	23.6	0.813(798)	-1.322(1.186)	-3.821(5.390)	-	0.220(030)
8.806(277)	1.107	0.352	17.1	19.7	0.265(195)	-1.376(1.184)	-	-	0.240(011)
8.468(404)	1.180	0.298	17.8	20.5	0.698(791)	-	-4.209(5.378)	-	0.220(030)
8.645(279)	1.191	0.291	17.9	20.6	0.219(222)	-	-	-58.710(82.451)	0.236(013)
8.708(264)	1.129	0.333	16.4	17.6	0.086(119)	-	-	-	0.242(010)

TABLE XXVIII. Summary of parameters values in the 13-point CCFV fit (Eq. (29) with an additional term $c_4/(Q^{*2} + M_\pi^2)$) for obtaining g_P^* . The data used are given in Tables XXIV and XXV. In the top half, the quantity $g_P^* = (m_\mu/2M_N)\tilde{F}_P(Q^{*2})/(Q^{*2} + M_\pi^2)$, is extrapolated, while in the bottom half $g_P^* = (m_\mu/2M_N)\tilde{G}_P(Q^{*2})$ is used. Details are given in Sec. IV.

$g_{\pi NN}$	χ^2/DOF	p	AIC	AICc	$c_0[1]$	$c_1[a]$ fm $^{-1}$	$c_2[M_\pi^2]$ GeV $^{-2}$	$c_3[\text{FV}]$ GeV $^{-2}$
$g_{\pi NN}$ with \mathcal{S}_{sim} , z^2 fit, 13-point CCFV fit								
14.491(857)	0.878	0.544	15.9	20.9	1.330(090)	-0.942(752)	0.339(1.093)	55.002(56.824)
14.273(827)	0.884	0.547	14.8	17.5	1.296(083)	-0.637(683)	1.080(779)	-
14.713(764)	0.979	0.463	14.8	16.0	1.357(070)	-0.448(669)	-	-
13.666(511)	0.883	0.556	13.7	14.9	1.243(060)	-	0.935(763)	-
13.777(435)	0.886	0.553	13.7	14.9	1.270(040)	-	-	44.246(36.550)
14.225(228)	0.934	0.511	13.2	13.6	1.312(021)	-	-	-
$g_{\pi NN}$ with \mathcal{S}_{sim} , Pole-Dominance fit, 13-point CCFV fit								
14.135(852)	1.202	0.288	18.8	23.8	1.283(087)	-1.230(786)	1.098(1.026)	28.874(53.442)
13.975(799)	1.111	0.349	17.1	19.8	1.261(077)	-1.036(699)	1.497(711)	-
14.240(788)	1.412	0.159	19.5	20.7	1.313(073)	-0.519(655)	-	-
12.986(438)	1.209	0.274	17.3	18.5	1.177(051)	-	1.127(666)	-
13.271(381)	1.349	0.190	18.8	20.0	1.224(035)	-	-	35.810(31.073)
13.637(210)	1.347	0.184	18.2	18.5	1.257(019)	-	-	-

TABLE XXIX. Summary of the 13-point CCFV fit parameters for the extraction of $g_{\pi NN}$ as described in Sec. IV B 2. The data used are given in Tables XXIV and XXV. In the top table, the product $g_{\pi NN}\tilde{F}_\pi = M_N\tilde{F}_P(-M_\pi^2)$ is extrapolated, and the result, in the continuum, is divided by $F_\pi = 92.9 \text{ MeV}$. In the bottom table, $\tilde{F}_P(-M_\pi^2)$ is extrapolated and the result in the continuum multiplied by M_N/F_π .

Appendix F: Data for the extraction of $g_{A,S,T}$ from forward matrix elements

This appendix gives the results of fits used to extract the charges $g_{A,S,T}$ from forward matrix elements and their renormalized values at the physical point obtained from various CCFV fits discussed in the main text.

ID	$M_1 - M_0$	$M_2 - M_0$				
		Axial	Scalar	Tensor	Vector	prior
a15m310	2.2	3.50(01)	3.52(01)	3.52(03)	3.50(02)	3.52(12)
a12m310	2.0	4.32(11)	4.51(07)	3.78(14)	4.46(08)	4.55(26)
a12m220L	1.7	5.19(30)	6.26(11)	6.01(17)	6.01(08)	6.05(44)
a12m220	2.0	5.93(12)	6.02(08)	5.55(23)	5.88(12)	6.00(44)
a12m220S	2.5	6.09(04)	6.12(03)	5.97(12)	6.10(05)	6.13(36)
a09m310	2.0	2.91(16)	3.24(11)	3.29(08)	3.43(10)	3.15(21)
a09m220	1.8	3.90(66)	4.43(20)	4.49(14)	2.07(07)	4.35(40)
a09m130W	2.1	5.83(39)	7.27(29)	6.48(23)	2.37(05)	5.84(66)
a06m310	2.0	3.01(02)	3.03(02)	3.11(03)	3.05(01)	3.04(11)
a06m310W	2.0	3.95(04)	3.94(03)	3.89(06)	3.95(02)	3.94(21)
a06m220	2.0	4.20(13)	4.40(06)	4.50(11)	4.47(06)	4.49(29)
a06m220W	2.0	4.91(06)	4.96(04)	5.04(10)	4.95(03)	4.98(29)
a06m135	2.2	6.43(07)	6.84(16)	6.93(27)	6.71(08)	6.60(51)

TABLE XXX. Mass gaps of excited state for the 3-RD- $N\pi$ fit in units of the lattice pion mass for each ensemble. The M_1 is fixed to the non-interacting energy of the $N(\mathbf{n}) + \pi(-\mathbf{n})$ state with $\mathbf{n} = (1, 0, 0)$. The M_2 is constrained to be near the first excited state mass given by the two-point correlator by using the narrow prior shown in the last column. These mass gaps can be compared with the 3-RD fit results given in the Table XXXII.

ID	g_A	p	g_S	p	g_T	p	g_V	p
a15m310	1.266(017)	0.780	0.834(018)	0.040	1.133(006)	0.819	1.073(004)	0.528
	1.250(007)	0.591	0.868(028)	0.002	1.121(006)	0.641	1.069(004)	0.000
	1.243(005)	0.607	0.838(019)	0.031	1.132(004)	0.811	1.070(003)	0.394
a12m310	1.256(006)	0.247	0.929(031)	0.180	1.068(009)	0.089	1.055(005)	0.097
	1.283(018)	0.436	1.091(083)	0.007	1.034(020)	0.060	1.061(008)	0.106
	1.241(005)	0.047	0.910(015)	0.215	1.083(005)	0.000	1.053(002)	0.069
a12m220L	1.275(005)	0.175	0.829(025)	0.038	1.090(007)	0.679	1.068(003)	0.053
	1.289(013)	0.410	0.873(042)	0.000	1.069(011)	0.194	1.067(004)	0.165
	1.266(007)	0.005	0.865(016)	0.089	1.092(003)	0.690	1.064(002)	0.035
a12m220	1.253(010)	0.252	0.987(056)	0.561	1.080(011)	0.363	1.063(004)	0.892
	1.265(021)	0.173	1.113(095)	0.401	1.048(018)	0.243	1.071(009)	0.622
	1.239(007)	0.157	0.929(029)	0.445	1.084(006)	0.266	1.061(003)	0.846
a12m220S	1.257(017)	0.715	0.908(213)	0.113	1.103(027)	0.982	1.065(006)	0.775
	1.266(044)	0.631	1.003(260)	0.015	1.065(039)	0.754	1.081(018)	1.000
	1.245(012)	0.627	0.967(097)	0.100	1.110(011)	0.861	1.061(004)	0.713
a09m310	1.275(017)	0.593	1.000(019)	0.305	1.029(004)	0.620	1.047(002)	0.034
	1.238(008)	0.426	1.016(027)	0.170	1.027(007)	0.375	1.036(004)	0.080
	1.212(004)	0.000	1.006(011)	0.291	1.025(004)	0.463	1.067(008)	0.000
a09m220	1.282(016)	0.173	0.987(025)	0.570	1.018(004)	0.809	1.051(002)	0.449
	1.279(013)	0.440	1.056(046)	0.222	1.001(011)	0.634	1.049(004)	0.325
	1.216(006)	0.000	0.989(015)	0.531	1.007(005)	0.379	1.040(007)	0.000
a09m130W	1.320(034)	0.132	1.049(023)	0.542	1.010(006)	0.869	1.054(002)	0.045
	1.271(015)	0.021	1.049(061)	0.069	1.000(011)	0.648	1.052(006)	0.090
	1.231(006)	0.006	1.135(024)	0.068	0.990(007)	0.250	1.011(008)	0.000
a06m310	1.271(057)	0.439	1.172(082)	0.873	0.992(007)	0.217	1.041(005)	0.823
	1.243(027)	0.840	1.239(108)	0.352	0.982(020)	0.738	1.033(010)	0.773
	1.181(008)	0.098	1.121(003)	0.829	0.980(006)	0.058	1.054(011)	0.586
a06m310W	1.264(089)	0.397	1.115(065)	0.288	0.979(016)	0.438	1.036(005)	0.886
	1.216(021)	0.669	1.122(073)	0.501	0.975(016)	0.094	1.035(011)	0.413
	1.208(012)	0.358	1.144(049)	0.280	0.985(009)	0.407	1.036(005)	0.883
a06m220	1.336(065)	0.009	1.183(157)	0.625	0.975(011)	0.668	1.048(005)	0.373
	1.235(018)	0.012	1.109(066)	0.275	0.975(012)	0.372	1.050(007)	0.328
	1.190(011)	0.000	1.026(028)	0.484	0.975(007)	0.664	1.059(007)	0.359
a06m220W	1.383(079)	0.751	0.818(065)	0.539	0.977(012)	0.078	1.039(006)	0.908
	1.257(024)	0.643	0.769(089)	0.770	0.962(022)	0.084	1.039(009)	0.724
	1.212(012)	0.303	0.866(055)	0.454	0.971(008)	0.104	1.037(004)	0.882
a06m135	1.281(061)	0.518	1.025(050)	0.460	0.966(010)	0.277	1.039(005)	0.354
	1.242(021)	0.641	1.108(110)	0.382	0.950(014)	0.208	1.039(006)	0.303
	1.198(010)	0.272	1.154(073)	0.312	0.942(009)	0.072	1.075(007)	0.003

TABLE XXXI. Summary of bare charges g_A , g_S , g_T , and g_V obtained from forward matrix elements along with the p -value of the three fits used to remove ESC: 3-RD (first row), 3^* (or 2-state for g_S) (second row), and 3-RD- $N\pi$ (third row) described in the text. The mass gap $M_2 - M_0$ output by the 3-RD- $N\pi$ fits is summarized in Table XXX.

Ensemble ID	Charge	$r_2 b_{02}$	$r_1 r_2 b_{12}$	$a\Delta M_2$	$\frac{M_1 - M_0}{M_\pi}$	$\frac{M_2 - M_0}{M_\pi}$	$\frac{M(N\pi) - M_0}{M_\pi}$
a15m310	A	-0.063(008)	-0.00(00)	-0.37(11)	3.5(1)	2.0(4)	2.2
a12m310	A	-0.047(008)	-4.0(2.9)	-0.15(10)	4.6(2)	3.7(5)	2.0
a12m220L	A	-0.051(011)	-3.4(1.7)	-0.16(08)	6.1(1)	4.9(6)	1.7
a12m220	A	-0.055(011)	-2.9(3.4)	-0.07(19)	6.0(1)	5.5(1.4)	2.0
a12m220S	A	-0.041(021)	-2.7(4.8)	-0.18(23)	6.1(3)	4.8(1.7)	2.5
a09m310	A	-0.076(013)	0.12(03)	-0.26(06)	3.2(5)	1.3(1)	2.0
a09m220	A	-0.091(012)	0.18(03)	-0.23(04)	4.3(4)	2.0(1)	1.8
a09m130W	A	-0.111(024)	0.20(04)	-0.19(03)	5.8(6)	2.8(3)	2.1
a06m310	A	-0.127(038)	0.12(14)	-0.17(06)	3.0(4)	1.2(3)	2.0
a06m310W	A	-0.070(073)	0.19(29)	-0.27(06)	3.9(5)	1.1(5)	2.0
a06m220	A	-0.191(041)	0.17(15)	-0.19(03)	4.5(2)	1.7(2)	2.0
a06m220W	A	-0.183(058)	0.42(30)	-0.24(03)	5.0(4)	1.5(2)	2.0
a06m135	A	-0.149(052)	0.32(09)	-0.13(03)	6.6(3)	3.3(5)	2.2
a15m310	S	-0.190(026)	1.13(66)	0.04(08)	3.5(1)	3.7(3)	2.2
a12m310	S	-0.273(045)	-5.6(5.7)	-0.14(16)	4.6(2)	3.8(8)	2.0
a12m220L	S	-0.224(050)	10(13)	0.07(03)	6.1(1)	6.5(2)	1.7
a12m220	S	-0.242(034)	-27(18)	0.04(07)	6.0(1)	6.3(5)	2.0
a12m220S	S	-0.256(086)	18(56)	-0.12(34)	6.1(3)	5.3(2.5)	2.5
a09m310	S	-0.325(007)	-0.04(11)	0.03(09)	3.2(5)	3.4(3)	2.0
a09m220	S	-0.324(009)	0.43(18)	-0.00(00)	4.3(4)	4.3(4)	1.8
a09m130W	S	-0.316(037)	-0.35(55)	0.36(10)	5.8(6)	11.8(1.5)	2.1
a06m310	S	-0.402(026)	-0.9(1.3)	-0.06(08)	3.0(4)	2.4(7)	2.0
a06m310W	S	-0.401(086)	7(17)	-0.02(06)	3.9(5)	3.8(7)	2.0
a06m220	S	-0.482(079)	0.2(1.3)	-0.12(06)	4.5(2)	2.7(9)	2.0
a06m220W	S	-0.424(351)	57(64)	0.09(13)	5.0(4)	6.3(1.8)	2.0
a06m135	S	-0.130(267)	-14.0(8.7)	0.33(10)	6.6(3)	15.0(2.5)	2.2
a15m310	T	0.136(007)	0.10(13)	0.03(07)	3.5(1)	3.6(3)	2.2
a12m310	T	0.172(007)	-1.17(69)	-0.30(05)	4.6(2)	3.0(2)	2.0
a12m220L	T	0.190(020)	-2.06(92)	-0.12(10)	6.1(1)	5.2(7)	1.7
a12m220	T	0.187(008)	-2.3(1.2)	-0.18(08)	6.0(1)	4.7(6)	2.0
a12m220S	T	0.189(033)	-4.4(2.7)	-0.25(12)	6.1(3)	4.3(9)	2.5
a09m310	T	0.200(002)	0.33(07)	0.04(07)	3.2(5)	3.4(1)	2.0
a09m220	T	0.206(003)	0.62(08)	0.07(04)	4.3(4)	5.0(2)	1.8
a09m130W	T	0.214(006)	0.61(07)	0.11(03)	5.8(6)	7.6(3)	2.1
a06m310	T	0.215(029)	1.25(71)	0.11(05)	3.0(4)	4.2(6)	2.0
a06m310W	T	0.227(026)	0.15(43)	-0.05(07)	3.9(5)	3.4(7)	2.0
a06m220	T	0.191(014)	0.17(54)	0.01(04)	4.5(2)	4.7(6)	2.0
a06m220W	T	0.230(028)	-0.15(78)	-0.01(06)	5.0(4)	4.8(9)	2.0
a06m135	T	0.226(016)	1.91(67)	0.12(04)	6.6(3)	9.7(1.1)	2.2
a15m310	V	-0.012(001)	0.16(08)	-0.23(07)	3.5(1)	2.6(3)	2.2
a12m310	V	-0.008(001)	-0.2(2.1)	-0.17(22)	4.6(2)	3.7(1.1)	2.0
a12m220L	V	-0.009(001)	0.04(07)	-0.45(13)	6.1(1)	2.7(9)	1.7
a12m220	V	-0.009(001)	0.06(18)	-0.26(12)	6.0(1)	4.1(9)	2.0
a12m220S	V	-0.009(002)	0.04(18)	-0.36(25)	6.1(3)	3.5(1.9)	2.5
a09m310	V	-0.006(000)	0.36(08)	0.02(01)	3.2(5)	3.3(5)	2.0
a09m220	V	-0.006(000)	0.53(08)	0.01(00)	4.3(4)	4.5(4)	1.8
a09m130W	V	-0.006(000)	0.48(03)	0.01(00)	5.8(6)	6.0(7)	2.1
a06m310	V	-0.005(001)	0.66(28)	0.01(04)	3.0(4)	3.2(7)	2.0
a06m310W	V	-0.006(004)	-0.4(1.3)	0.13(14)	3.9(5)	5.3(1.5)	2.0
a06m220	V	-0.009(002)	1.29(42)	0.07(02)	4.5(2)	5.5(5)	2.0
a06m220W	V	-0.004(001)	0.03(17)	-0.17(16)	5.0(4)	2.6(2.3)	2.0
a06m135	V	-0.003(001)	0.78(16)	0.01(02)	6.6(3)	6.8(6)	2.2

TABLE XXXII. Outputs $r_2 b_{02}$, $r_1 r_2 b_{12}$, and the excited state mass gap $a\Delta M_2$ of the 3-RD fit for the axial (A), scalar (S), tensor (T) and vector (V) charges. The mass gaps in columns 6–8 are in units of M_π for that ensemble. The mass gap $M(N\pi) - M_0 \equiv M_N(\mathbf{n}) + M_\pi(-\mathbf{n}) - M_0$ with $\mathbf{n} = (1, 0, 0)$ is close to $M_2 - M_0$ for the axial channel and much smaller for the other charges. Note that $M_1 - M_0$ and $M(N\pi) - M_0$ are the same for the four charges.

g_A	χ^2/DOF	$p\text{-value}$	AIC	AICc	$c_0[1]$	$c_1[a]$ fm^{-1}	$c_2[M_\pi^2]$ GeV^{-2}	$c[\text{FV}]$ GeV^{-2}
$Z_A g_A^{(\text{bare})}$, 13-pt								
1.281(052)	0.296	0.987	7.3	8.5	1.281(052)	-0.59(45)	-	-
1.228(029)	0.430	0.943	8.7	9.9	1.232(036)	-	-0.22(48)	-
1.281(052)	0.325	0.975	9.3	11.9	1.280(054)	-0.60(49)	0.03(52)	-
1.285(054)	0.348	0.959	11.1	16.1	1.287(057)	-0.69(55)	-0.08(60)	10.0(28.7)
$Z_A g_A^{(\text{bare})}$, 11-pt-narrow								
1.264(057)	0.214	0.993	5.9	7.4	1.264(057)	-0.45(49)	-	-
1.222(029)	0.295	0.976	6.7	8.2	1.225(037)	-	-0.18(49)	-
1.264(057)	0.241	0.983	7.9	11.4	1.263(058)	-0.47(55)	0.04(55)	-
1.268(059)	0.265	0.967	9.9	16.5	1.269(062)	-0.54(62)	-0.04(62)	7.7(28.8)
$Z_A g_A^{(\text{bare})}$, 10-pt-narrow								
1.308(072)	0.112	0.999	4.9	6.6	1.308(072)	-0.93(68)	-	-
1.226(031)	0.313	0.961	6.5	8.2	1.232(040)	-	-0.32(60)	-
1.316(074)	0.105	0.998	6.7	10.7	1.320(078)	-0.90(68)	-0.25(61)	-
1.317(075)	0.115	0.995	8.7	16.7	1.321(078)	-0.88(69)	-0.20(64)	-6.7(31.8)
$Z_A/Z_V \times g_A^{(\text{bare})}/g_V^{(\text{bare})}$, 13-pt								
1.317(037)	0.334	0.979	7.7	8.9	1.317(037)	-0.62(33)	-	-
1.252(014)	0.651	0.786	11.2	12.4	1.253(018)	-	-0.09(26)	-
1.317(038)	0.367	0.961	9.7	12.3	1.317(039)	-0.62(33)	0.00(26)	-
1.316(038)	0.403	0.934	11.6	16.6	1.315(040)	-0.61(34)	0.03(31)	-3.0(13.8)
$Z_A/Z_V \times g_A^{(\text{bare})}/g_V^{(\text{bare})}$, 11-pt-narrow								
1.310(039)	0.268	0.983	6.4	7.9	1.310(039)	-0.56(34)	-	-
1.250(014)	0.555	0.835	9.0	10.5	1.252(018)	-	-0.07(26)	-
1.309(039)	0.302	0.966	8.4	11.8	1.309(040)	-0.56(35)	0.01(27)	-
1.308(040)	0.335	0.939	10.3	17.0	1.307(041)	-0.54(36)	0.05(31)	-3.7(13.8)
$Z_A/Z_V \times g_A^{(\text{bare})}/g_V^{(\text{bare})}$, 10-pt-narrow								
1.320(044)	0.266	0.977	6.1	7.8	1.320(044)	-0.66(39)	-	-
1.250(014)	0.617	0.764	8.9	10.7	1.251(019)	-	-0.05(28)	-
1.321(045)	0.302	0.953	8.1	12.1	1.322(047)	-0.66(39)	-0.03(28)	-
1.323(045)	0.312	0.931	9.9	17.9	1.322(047)	-0.65(39)	0.03(31)	-7.3(14.8)
$(Z_A g_A^{(\text{bare})} + Z_A/Z_V \times g_A^{(\text{bare})}/g_V^{(\text{bare})})/2$, 13-pt								
1.292(041)	0.354	0.973	7.9	9.1	1.292(041)	-0.56(36)	-	-
1.238(019)	0.551	0.869	10.1	11.3	1.241(024)	-	-0.18(33)	-
1.292(041)	0.389	0.952	9.9	12.6	1.292(042)	-0.56(38)	0.00(35)	-
1.294(042)	0.429	0.920	11.9	16.9	1.294(044)	-0.59(41)	-0.03(39)	3.0(17.6)
$(Z_A g_A^{(\text{bare})} + Z_A/Z_V \times g_A^{(\text{bare})}/g_V^{(\text{bare})})/2$, 11-pt-narrow								
1.280(044)	0.268	0.983	6.4	7.9	1.280(044)	-0.46(38)	-	-
1.235(019)	0.411	0.930	7.7	9.2	1.238(024)	-	-0.15(33)	-
1.280(044)	0.301	0.966	8.4	11.8	1.280(044)	-0.46(41)	-0.00(36)	-
1.281(045)	0.343	0.934	10.4	17.1	1.282(047)	-0.48(44)	-0.02(40)	1.5(17.7)
$(Z_A g_A^{(\text{bare})} + Z_A/Z_V \times g_A^{(\text{bare})}/g_V^{(\text{bare})})/2$, 10-pt-narrow								
1.311(054)	0.183	0.993	5.5	7.2	1.311(054)	-0.77(49)	-	-
1.237(020)	0.456	0.888	7.6	9.4	1.240(026)	-	-0.20(38)	-
1.316(056)	0.187	0.988	7.3	11.3	1.319(058)	-0.75(49)	-0.15(39)	-
1.317(056)	0.195	0.978	9.2	17.2	1.319(058)	-0.73(50)	-0.10(41)	-7.1(19.3)

TABLE XXXIII. Summary of CCFV fits to g_A using Eq. 29 for three different cuts on the 13 points and three different renormalization procedures defined in the text.

g_T	χ^2/DOF	p -value	AIC	AICc	$c_0[1]$	$c_1[a]$ fm^{-1}	$c_2[M_\pi^2]$ GeV^{-2}	$c[\text{FV}]$ GeV^{-2}
$Z_T g_T^{(\text{bare})}$, 13-pt								
0.990(029)	0.281	0.989	7.1	8.3	0.990(029)	0.35(32)	-	-
1.001(019)	0.270	0.991	7.0	8.2	0.994(024)	-	0.38(33)	-
0.980(031)	0.222	0.994	8.2	10.9	0.974(033)	0.29(33)	0.32(34)	-
0.982(031)	0.145	0.998	9.3	14.3	0.982(034)	0.11(38)	0.02(46)	30.4(31.8)
$Z_T g_T^{(\text{bare})}$, 11-pt-narrow								
0.983(034)	0.329	0.966	7.0	8.5	0.983(034)	0.40(35)	-	-
0.999(020)	0.303	0.974	6.7	8.2	0.991(026)	-	0.45(36)	-
0.978(034)	0.266	0.977	8.1	11.6	0.971(036)	0.29(37)	0.35(38)	-
0.981(034)	0.176	0.990	9.2	15.9	0.980(037)	0.10(42)	0.05(49)	30.1(31.9)
$Z_T g_T^{(\text{bare})}$, 10-pt-narrow								
1.012(040)	0.156	0.996	5.2	7.0	1.012(040)	0.00(46)	-	-
1.004(020)	0.117	0.999	4.9	6.6	1.000(026)	-	0.22(39)	-
1.005(042)	0.133	0.996	6.9	10.9	1.001(045)	-0.02(47)	0.22(40)	-
1.000(044)	0.124	0.993	8.7	16.7	0.998(046)	-0.04(47)	0.09(50)	16.3(37.5)
$Z_T/Z_V \times g_T^{(\text{bare})}/g_V^{(\text{bare})}$, 13-pt								
1.008(025)	0.172	0.999	5.9	7.1	1.008(025)	0.38(28)	-	-
1.024(015)	0.208	0.997	6.3	7.5	1.018(019)	-	0.33(27)	-
0.999(026)	0.089	1.000	6.9	9.6	0.994(028)	0.33(28)	0.27(27)	-
1.000(026)	0.072	1.000	8.7	13.7	0.997(029)	0.27(31)	0.14(38)	13.1(26.7)
$Z_T/Z_V \times g_T^{(\text{bare})}/g_V^{(\text{bare})}$, 11-pt-narrow								
1.002(029)	0.192	0.995	5.7	7.2	1.002(029)	0.43(30)	-	-
1.024(016)	0.227	0.991	6.0	7.5	1.017(020)	-	0.37(29)	-
0.997(029)	0.105	0.999	6.8	10.3	0.992(031)	0.35(32)	0.28(30)	-
0.998(029)	0.088	0.999	8.6	15.3	0.995(031)	0.28(35)	0.15(40)	12.8(26.8)
$Z_T/Z_V \times g_T^{(\text{bare})}/g_V^{(\text{bare})}$, 10-pt-narrow								
1.009(033)	0.198	0.991	5.6	7.3	1.009(033)	0.34(38)	-	-
1.026(016)	0.188	0.993	5.5	7.2	1.020(021)	-	0.29(31)	-
1.000(035)	0.118	0.997	6.8	10.8	0.995(037)	0.32(39)	0.27(31)	-
0.995(037)	0.099	0.997	8.6	16.6	0.992(038)	0.30(39)	0.14(41)	15.3(31.7)
$(Z_T g_T^{(\text{bare})} + Z_T/Z_V \times g_T^{(\text{bare})}/g_V^{(\text{bare})})/2$, 13-pt								
0.998(020)	0.383	0.963	8.2	9.4	0.998(020)	0.37(22)	-	-
1.012(013)	0.387	0.962	8.3	9.5	1.005(016)	-	0.36(22)	-
0.989(021)	0.249	0.991	8.5	11.2	0.984(023)	0.30(23)	0.30(23)	-
0.991(021)	0.167	0.997	9.5	14.5	0.990(024)	0.19(25)	0.08(32)	21.8(22.0)
$(Z_T g_T^{(\text{bare})} + Z_T/Z_V \times g_T^{(\text{bare})}/g_V^{(\text{bare})})/2$, 11-pt-narrow								
0.993(023)	0.440	0.914	8.0	9.5	0.993(023)	0.41(24)	-	-
1.011(013)	0.432	0.919	7.9	9.4	1.004(017)	-	0.41(24)	-
0.987(023)	0.296	0.967	8.4	11.8	0.982(025)	0.31(25)	0.32(25)	-
0.990(024)	0.202	0.985	9.4	16.1	0.988(026)	0.19(28)	0.10(34)	21.5(22.1)
$(Z_T g_T^{(\text{bare})} + Z_T/Z_V \times g_T^{(\text{bare})}/g_V^{(\text{bare})})/2$, 10-pt-narrow								
1.012(028)	0.303	0.965	6.4	8.1	1.012(028)	0.16(32)	-	-
1.014(013)	0.214	0.989	5.7	7.4	1.009(018)	-	0.26(26)	-
1.003(029)	0.217	0.982	7.5	11.5	0.999(031)	0.14(32)	0.25(26)	-
0.998(030)	0.205	0.975	9.2	17.2	0.996(031)	0.13(32)	0.13(34)	14.7(27.1)

TABLE XXXIV. Summary of CCFV fits to g_T using Eq. 29 for three different cuts on the 13 points and three different renormalization procedures defined in the text.

g_S	χ^2/DOF	$p\text{-value}$	AIC	AICc	$c_0[1]$	$c_1[a]$ fm^{-1}	$c_2[M_\pi^2]$ GeV^{-2}	$c[\text{FV}]$ GeV^{-2}
$Z_S g_S^{(\text{bare})}$, 13-pt								
0.991(046)	2.073	0.019	26.8	28.0	0.991(046)	-1.37(46)	-	-
0.876(021)	2.809	0.001	34.9	36.1	0.882(027)	-	-0.32(37)	-
0.991(046)	2.278	0.012	28.8	31.4	0.990(047)	-1.40(49)	0.07(40)	-
1.001(047)	2.435	0.009	29.9	34.9	1.008(050)	-1.61(54)	-0.37(62)	38.7(41.6)
$Z_S g_S^{(\text{bare})}$, 11-pt-narrow								
1.044(051)	1.055	0.393	13.5	15.0	1.044(051)	-1.83(50)	-	-
0.888(022)	2.317	0.013	24.9	26.4	0.897(028)	-	-0.52(38)	-
1.045(051)	1.180	0.307	15.4	18.9	1.043(051)	-1.88(56)	0.10(42)	-
1.066(053)	1.056	0.389	15.4	22.1	1.076(056)	-2.27(62)	-0.56(63)	60.4(42.2)
$Z_S g_S^{(\text{bare})}$, 10-pt-narrow								
1.077(070)	1.130	0.339	13.0	14.8	1.077(070)	-2.20(75)	-	-
0.882(022)	2.179	0.026	21.4	23.1	0.886(028)	-	-0.21(42)	-
1.076(070)	1.288	0.251	15.0	19.0	1.075(071)	-2.23(77)	0.06(43)	-
0.993(086)	1.043	0.395	14.3	22.3	1.016(080)	-1.67(84)	-1.23(89)	132.3(79.7)
$Z_S/Z_V \times g_S^{(\text{bare})}/g_V^{(\text{bare})}$, 13-pt								
0.999(053)	2.456	0.005	31.0	32.2	0.999(053)	-1.43(49)	-	-
0.832(027)	3.202	0.000	39.2	40.4	0.826(034)	-	0.31(47)	-
0.988(054)	2.396	0.008	30.0	32.6	0.973(055)	-1.73(52)	0.87(50)	-
0.994(054)	2.513	0.007	30.6	35.6	0.990(057)	-1.78(52)	0.21(76)	44.6(38.6)
$Z_S/Z_V \times g_S^{(\text{bare})}/g_V^{(\text{bare})}$, 11-pt-narrow								
1.072(064)	1.696	0.084	19.3	20.8	1.072(064)	-2.03(56)	-	-
0.846(027)	3.132	0.001	32.2	33.7	0.846(035)	-	0.04(48)	-
1.083(064)	1.443	0.173	17.5	21.0	1.064(064)	-2.59(63)	1.05(54)	-
1.093(064)	1.312	0.240	17.2	23.8	1.090(066)	-2.68(64)	0.16(79)	59.8(38.9)
$Z_S/Z_V \times g_S^{(\text{bare})}/g_V^{(\text{bare})}$, 10-pt-narrow								
1.103(074)	1.825	0.067	18.6	20.3	1.103(074)	-2.35(69)	-	-
0.837(028)	3.211	0.001	29.7	31.4	0.829(037)	-	0.40(54)	-
1.097(074)	1.630	0.122	17.4	21.4	1.079(075)	-2.71(72)	1.00(56)	-
0.981(089)	0.987	0.432	13.9	21.9	1.001(082)	-1.69(84)	-1.10(1.05)	174.6(74.5)
$(Z_S g_S^{(\text{bare})} + Z_S/Z_V \times g_S^{(\text{bare})}/g_V^{(\text{bare})})/2$, 13-pt								
1.004(043)	2.563	0.003	32.2	33.4	1.004(043)	-1.46(40)	-	-
0.867(022)	3.727	0.000	45.0	46.2	0.871(028)	-	-0.24(37)	-
1.003(043)	2.737	0.002	33.4	36.0	0.996(044)	-1.62(44)	0.37(41)	-
1.014(044)	2.883	0.002	33.9	38.9	1.017(047)	-1.81(47)	-0.17(60)	40.7(34.1)
$(Z_S g_S^{(\text{bare})} + Z_S/Z_V \times g_S^{(\text{bare})}/g_V^{(\text{bare})})/2$, 11-pt-narrow								
1.057(048)	1.547	0.125	17.9	19.4	1.057(048)	-1.90(44)	-	-
0.880(022)	3.408	0.000	34.7	36.2	0.888(028)	-	-0.47(38)	-
1.064(049)	1.600	0.119	18.8	22.2	1.055(049)	-2.18(51)	0.47(44)	-
1.085(050)	1.420	0.192	17.9	24.6	1.090(053)	-2.49(55)	-0.28(62)	58.2(34.4)
$(Z_S g_S^{(\text{bare})} + Z_S/Z_V \times g_S^{(\text{bare})}/g_V^{(\text{bare})})/2$, 10-pt-narrow								
1.095(063)	1.636	0.109	17.1	18.8	1.095(063)	-2.32(64)	-	-
0.870(023)	3.294	0.001	30.4	32.1	0.871(029)	-	-0.04(43)	-
1.093(063)	1.755	0.092	18.3	22.3	1.085(064)	-2.47(66)	0.40(45)	-
0.983(080)	1.212	0.296	15.3	23.3	1.007(073)	-1.63(76)	-1.32(89)	163.2(72.9)

TABLE XXXV. Summary of CCFV fits to g_S using Eq. 29 for three different cuts on the 13 points and three different renormalization procedures defined in the text.